A Novel Magnetic Resonance Imaging (MRI) Approach for Measuring Weak Electric Currents Inside the Human Brain

Göksu, Cihan

Publication date:
2017

Document Version
Publisher's PDF, also known as Version of record

Technical University of Denmark

Cihan Göksu

A Novel Magnetic Resonance Imaging (MRI) Approach for Measuring Weak Electric Currents Inside the Human Brain

PhD thesis, August 2017

DTU Electrical Engineering
Department of Electrical Engineering

DANISH RESEARCH
CENTRE FOR
MAGNETIC RESONANCE

PhD Thesis

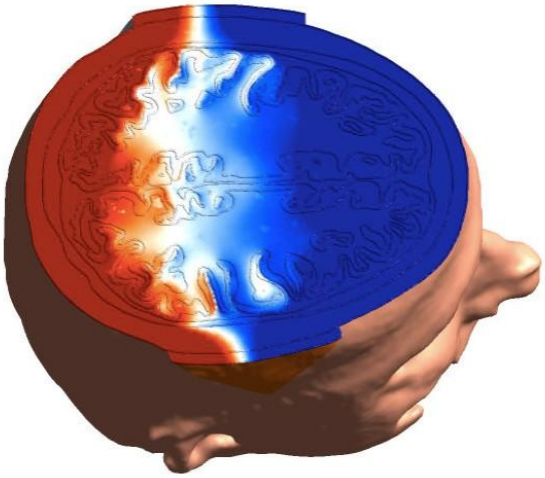

A Novel Magnetic Resonance Imaging (MRI) Approach for Measuring Weak Electric Currents Inside the Human Brain

Cihan Göksu

Supervised by: Assoc. Prof. Axel Thielscher, PhD, and
Assoc. Prof. Lars G. Hanson, PhD

Technical University of Denmark
Kgs. Lyngby, Denmark 2017

Copenhagen University Hospital Hvidovre
Centre for Functional and Diagnostic Imaging and Research
Danish Research Centre for Magnetic Resonance
Section 714
Kettegaard Allé 30
2650 Hvidovre
DENMARK
Tel: (+45) 3862 1184
Web: www.drcmr.dk
E-mail: info@drcmr.dk

Technical University of Denmark
Department of Electrical Engineering
Center for Magnetic Resonance
Ørsted Plads 349
2800 Kgs. Lyngby
DENMARK
Tel: (+45) 45 25 35 00
Web: www.elektro.dtu.dk
E-mail: info@elektro.dtu.dk

Abstract

Knowing the electrical conductivity and current density distribution inside the human brain will be useful in various biomedical applications, i.e. for improving the efficiency of non-invasive brain stimulation (NIBS) techniques, the accuracy of electroencephalography (EEG) and magnetoencephalography (MEG) source localization, or localization of pathological tissues. For example, the accuracy of electric field simulations for NIBS techniques is currently reduced by assigning inaccurate ohmic conductivity values taken from literature to different brain tissues. Therefore, the knowledge of individual ohmic conductivity values may open up the possibility of creating more realistic and accurate head models, which may ameliorate the simulations and practical use of NIBS techniques.

Magnetic resonance current density imaging (MRCDI) and magnetic resonance electrical impedance tomography (MREIT) are two emerging methods for calculating the current flow and for reconstructing the ohmic conductivity distribution inside the human brain. Both methods use measurements of the magnetic field $\Delta B_{z,c}$ that are induced by weak currents applied via surface electrodes. The sensitivity of the measurements directly affects the accuracy of the current flow estimations and the quality of the reconstructed conductivity images. It increases with increasing strength of the injected currents that are limited to 1-2 mA for in-vivo human brain applications. Therefore, sensitivity improvements of the underlying MRI methods are crucial for implementing MRCDI and MREIT in neuroscience and clinical applications.

In this thesis, systematic sensitivity and efficiency analyses of two different MRI pulse sequences, multi-echo spin echo (MESE) and steady-state free precession free induction decay (SSFP-FID), are performed in order to optimize these sequences for in-vivo application in the human brain. The simulations are validated by comprehensive phantom experiments. Secondly, the optimized sequences are tested for in-vivo human brain applications, and adapted to increase their robustness to physiological noise. The current-induced magnetic field $\Delta B_{z,c}$ inside the brain is measured in different individuals, revealing inter-individual $\Delta B_{z,c}$ differences due to anatomical variability. Finally, volume conductor models of the individuals are created and used to simulate the current-induced $\Delta B_{z,c}$ images and the current flow distributions. Comparison of the $\Delta B_{z,c}$ and current flow simulations and measurements demonstrates a good correspondence. In summary, the results presented in this thesis pave the way for employing the optimized MRI sequences in future studies to improve the efficiency of NIBS techniques.

Resumé

At kende fordelingen af elektrisk konduktivitet og strømtæthed i menneskets hjerne vil være nyttigt til forskellige biomedicinske anvendelser såsom øgning af effektiviteten af non-invasive hjernestimulationsteknikker (NIBS-teknikker), øgning af præcisionen af elektroencefalografi (EEG) og magnetoencefalografi (MEG) kildelokalisering samt lokalisering af patologisk væv. For eksempel er præcisionen af simulerede elektriske felter ved NIBS-teknikker for nuværende mindsket af, at man tildeler de forskellige væv i hjernen usikre ohmske konduktivitetsværdier kendt fra litteraturen.

Derfor kan viden om individuelle konduktivitetsværdier åbne muligheder for at skabe mere realistiske og præcise hovedmodeller, som kan forbedre simulering og praktisk anvendelse af NIBS-teknikker.

Magnetisk resonans strømtæthedsbilleddannelse (magnetic resonance current density imaging, MRCDI) og magnetisk resonans elektrisk impedans tomografi (MREIT) er to metoder under udvikling til beregning af strømtæthed og rekonstruktion af den ohmske konduktivitetsfordeling i menneskehjernen. Begge metoder anvender målinger af det magnetiske felt $\Delta B_{z,c}$, som induceres af svage strømme dannet ved hjælp af overfladeelektroder. Følsomheden af målingerne påvirker direkte præcisionen af strømtæthedsestimater og kvaliteten af de rekonstruerede konduktivitetsbilleder. Den øges med styrken af de tilførte strømme, som er begrænset til 1-2 mA for anvendelse in-vivo i hjernen på mennesker. Derfor er forbedringer af følsomheden i de underliggende MRI-metoder altafgørende for implementeringen af MRCDI og MREIT i neurovidenskabelig og klinisk sammenhæng.

Til denne afhandling udførtes systematiske sensitivitets- og effektivitetsanalyser af to forskellige MRI-puls-sekvenser, ”multi echo spin echo” (MESE) og ”steady-state free precession free induction decay” (SSFP-FID) for optimering af disse sekvenser til in-vivo anvendelse i den menneskelige hjerne. Simuleringerne valideredes med omfattende fantomforsøg. Dernæst testedes de optimerede sekvenser for anvendelse in-vivo i menneskehjerner, og de tilpassedes for at øge deres robusthed over for fysiologisk støj. Det strøminducerede magnetiske felt $\Delta B_{z,c}$ inde i hjernen måltes i forskellige individer og afslørede interindividuelle $\Delta B_{z,c}$-forskelle som følge af anatomisk variabilitet. Afslutningsvis skabtes volumenledningsmodeller ud fra hver forsøgsperson, og disse anvendtes til at simulere strøminducerede $\Delta B_{z,c}$ og strømtæthedsfordelinger. Ved sammenligning fandtes god overensstemmelse mellem $\Delta B_{z,c}$ simuleringer og målinger. Opsummeret baner resultaterne i denne afhandling vejen for anvendelse af de optimerede MRI-sekvenser i fremtidige studier af strømtæthedsfordelinger skabt ved non-invasiv in-vivo strømstimulering af menneskehjerner.

To My Family,

Preface

This thesis is submitted in partial fulfillment of the requirement for obtaining a PhD degree at the PhD school of Electrical Engineering at the Technical University of Denmark (DTU). The project was supervised by Associate Professor Axel Thielscher (main supervisor) and Associate Professor Lars G. Hanson (co-supervisor).

The thesis presents the study performed during my employment at the Department of Electrical Engineering at DTU from September 1st 2014 to August 31st 2017. The study was carried out in collaboration with two different research centers:

- Danish Research Centre for Magnetic Resonance (DRCMR), Centre for Functional and Diagnostic Imaging and Research, Copenhagen University Hospital Hvidovre, Denmark
- High-Field Magnetic Resonance Center, Max-Planck-Institute for Biological Cybernetics, Tübingen, Germany

In addition, I have had the pleasure of attending several international courses, research meeting and conferences, in particular the following:

- IDEA Sequence Programming (MR8SDE), SIEMENS Healthcare Training and Development, Cary NC, USA
- MRI Simulation for Sequence Development, Protocol Optimization and Education, ESMRMB course, Technical University of Denmark
- ESMRMB 33rd Annual Scientific Meeting 2016, Vienna, Austria
- ISMRM 25th Annual Meeting & Exhibition 2017, Honolulu, HI, USA

Furthermore, I have benefitted from teaching at DTU in the MSc. Course *31547 Medical Magnetic Resonance Imaging*.

Cihan Göksu

Copenhagen, August 2017

Acknowledgements

I would like to express my gratitude to my mentor and supervisor Axel Thielscher and my co-supervisor Lars G. Hanson for their guidance, criticism, favorable advice and suggestions, encouragement, and support throughout the entire research.

I also would like to express my gratitude to my external co-supervisors Prof. Klaus Scheffler and Dr. Philipp Ehses from the Max Planck Institute for Biological Cybernetics in Tübingen for their guidance, help, and support during my external research stay.

I am so grateful for the extraordinary friendly and motivating environment at DTU and DRCMR. I thank deeply everybody providing this wonderful environment, and especially my friends and colleagues Mürsel, Faruk, Jan Ole, Bakri, Bannay, Cristina, Rie, Guilherme, Leo, Natalia, Peter, Irina, Morten, Janine, Mitsuaki, David, Tiago, Jeanette, and many others I can't fit in here. I enjoyed every sip of an open-minded, friendly research environment on every work day (i.e. especially super challenging table football games, coffee breaks, and Friday bars ☺).

I am also grateful for the extraordinary friendly and motivating environment at the Max Planck Institute, Tübingen. Those six months contributed to the success of this thesis in various ways. Therefore, I would like to deeply thank everybody involved for providing this beautiful environment, especially my friends and colleagues Johannes, Alex, Marlon, and many others. I will never forget

the Schönbuch hikes, Friday bars, or briefly every second of my beautiful experiences in South Germany. I also would like to thank Sissy for her support, friendship, and understanding, and Nicole for her support and friendship. I appreciate their endless endeavor to teach me German. Overall, they were keeping me motivated in my studies and transformed it to an unforgettable experience.
I would also like to thank to everybody in my previous research group at METU for their support, help, and valuable discussions.
Finally, I would like to express my endless gratitude to my family. I owe every little part of my success to their love, understanding, and support. Those feelings were the strongest help keeping me on track throughout the entire study.

Table of Content

List of Figures

Abbreviations

α	Tip angle
$\Delta B_{z,c}$	Current-induced magnetic field
bSSFP	balanced Steady-State Free Precession
CDI	Current Density Imaging
EEG	Electroencephalography
EIT	Electrical Impedance Tomography
FID	Free Induction Decay
FOV	Field Of View
FWHM	Full Width Half Maximum
MEG	Magnetoencephalography
MESE	Multi-Echo Spin Echo
MR	Magnetic Resonance
MRI	Magnetic Resonance Imaging
N_{avg}	Number of averages
NIBS	Non-Invasive Brain Stimulation
RF	Radio Frequency
SE	Spin Echo
SNR	Signal-to-Noise Ratio
SSFP	Steady-State Free Precession
T_1	Spin-lattice relaxation time constant
T_2	Spin-spin relaxation time constant

T_2^*	Dephasing time constant
T_E	Echo time
T_{ES}	Echo spacing
T_R	Repetition time
TCS	Transcranial Current Stimulation
TDCS	Transcranial Direct Current Stimulation
TMS	Transcranial Magnetic Stimulation

1 INTRODUCTION

1.1 Motivation

Transcranial current stimulation (TCS) is a non-invasive brain stimulation technique that can be used to generate localized changes of the excitability of brain areas (1). Therefore, the method may have several useful neuroscience and clinical applications. For example, initial evidence suggests that the method may be used in the treatment of Parkinson's disease, chronic pain, depression, stroke, and that it has a positive effect on memory of healthy humans (2). However, efficient use of the method requires better target localization, which can only be provided by accurate simulation of the injected current flow. Recently, individualized simulations based on realistic head models have been realized. However, the model's accuracy can still be markedly improved by providing the exact individual electrical conductivity values of skin, skull, and brain tissues (3,4). This may enable better target localization and dosage control for TCS, but also other non-invasive brain stimulation (NIBS) methods (3,5).

The electrical conductivity of tissues is spatially distinct and depends on the pathological condition of the tissues. Therefore, knowing the electrical conductivity may be useful for diagnostic purposes (6,7). In addition, the knowledge of the electrical conductivity may improve source localization methods for electroencephalography (EEG) and magnetoencephalography (MEG) (8).

Electrical impedance tomography (EIT) was proposed to determine ohmic tissue conductivities (9). In conventional EIT, an external current is injected into the human body, and ohmic conductivity images are reconstructed from the voltage measurements performed via surface electrodes. However, EIT is hampered by its low spatial resolution and sensitivity to conductivity perturbations in regions away from surface electrodes. In order to ameliorate this problem, magnetic resonance electrical impedance tomography (MREIT) was proposed (10). MREIT combines magnetic resonance imaging (MRI), which is an imaging method providing high-resolution images, with the injection of weak currents to reconstruct ohmic conductivity images of the human body at a better spatial accuracy and higher sensitivity than EIT. The focus of this thesis is on current flow measurements in the human brain, which is particularly challenging due to the low conductivity of the skull compartment, reducing the current strengths inside the brain.

In MREIT of the human brain, an external electrical current is applied in synchrony with an MRI pulse sequence. The current flow inside the brain induces a magnetic field distribution, and the component of the induced magnetic field ($\Delta B_{z,c}$), which is parallel to the main magnetic field of the scanner (B_0), creates small shifts in the Larmor precession frequency. A frequency shift results in a change in the phase of the measured MRI signal, which is used to measure the $\Delta B_{z,c}$. The measured $\Delta B_{z,c}$ allows calculation of the current flow distribution and reconstruction of ohmic conductivity images of the brain.

1.2 Methods development

1.2.1 Magnetic field measurements using MRI

Scott *et al* (11) performed the very first $\Delta B_{z,c}$ and current flow measurements in a cylindrical phantom using MRI at 2 T. In that study, a standard single-echo

spin echo (SE) sequence was used. They conducted a sensitivity analysis (12), and demonstrated that the sensitivity of current-induced magnetic field measurements depends on the signal-to-noise ratio (SNR) of the MR image, and the phase sensitivity of the used MR sequence. Later on, Sadleir *et al* (13) conducted a further sensitivity study, this time at 3 and 11 T, and achieved similar findings with an alternative approach for the SNR analysis. They also performed proof-of-principle MREIT experiments at 11 T (10,13). Since then, the aim has been to make MREIT a clinically usable technique to measure the electrical conductivity and current flow distributions inside the human body.

1.2.2 MRCDI and MREIT

The measured current-induced magnetic field $\Delta B_{z,c}$ can be used to calculate the current flow distribution inside the body, with the method being denoted as magnetic resonance current density imaging (MRCDI) (11,12,14–21). Considering the Maxwell equation $\vec{\nabla} \times \vec{B}/\mu_0 = \vec{J}$ when displacement currents are insignificant ($\vec{B}$ is the magnetic field, μ_0 the permeability of free space, and $\vec{J}$ the current density distribution), the current density calculation requires knowledge of all magnetic field components. However, only the current-induced magnetic field component, which is parallel to the main magnetic field B_0, can be measured by MRI. Therefore, measuring all magnetic field components requires rotation of the imaged object. Several previously conducted studies employed this type of current density reconstruction for phantoms (11,14,17,19,22). However, subject rotation is not applicable for in-vivo human studies with the possible exception of small rotations in validation studies. In order to address this problem, methods to calculate the current density using only $\Delta B_{z,c}$ were developed and implemented (23–26).

In addition to the calculation of the current density, a further aspect is the reconstruction of the ohmic conductivity distribution inside the body, which may be useful in many biomedical applications, and is termed magnetic resonance electrical impedance tomography, MREIT. Several algorithms have been developed using either the measured $\Delta B_{z,c}$ or the reconstructed current density (20,27–31). The problem of subject rotation exists for MREIT as well. Therefore, also MREIT algorithms have been developed which use only a single component of the current-induced magnetic field (30,32). More detailed information is beyond the scope of this study. The reader is kindly referred to the review articles of (20,29, and 33), which serve as a useful introduction into these topics.

1.2.3 Pulse sequences for MREIT

In-vivo human applications of MREIT requires sequences with high phase sensitivity (see Chapters 2 and 3 for further details). In the following, I therefore give an overview of the major MRI sequences that have been developed for MRCDI and MREIT so far.

In 2005, Oh *et al* performed ex-vivo gradient-recalled echo (GRE) MREIT experiments with 12-48 mA in a cylindrical phantom which was filled with chunks of biological tissues surrounded by agar (34). They demonstrated the feasibility of conductivity imaging of soft tissue at high resolution when using sufficiently strong currents. Concurrently, induced-current MREIT (IC-MREIT) was proposed as a new imaging modality by Ider and Ozparlak that was based on the idea to employ induction coils to eliminate the prospective side effects of current stimulation via electrodes, e.g. tingling, phosphenes, and burning sensation (35).

In 2006, Hamamura *et al* tested the conductivity variation over time in an agar phantom using a current strength of 900 µA (36). The employed sequence was

a modified version of a single echo SE MREIT sequence, which was composed of repetitive refocusing pulses allowing for use of an alternating current-induced magnetic field before data acquisition (37). They observed ion diffusion by means of conductivity imaging. Later on, Bieri *et al* conducted a study on magnetic resonance elastography (MRE) (38), which is methodologically related to MRCDI. They employed a balanced alternating steady-state free precession (bSSFP) sequence and demonstrated that bSSFP has 10-15 fold higher phase sensitivity compared to standard MRE methods. In 2006, Sadleir *et al* extended their previous study (10) to compare SE and GRE sequences at 3 T and 11 T in ex-vivo biological tissue phantoms (39). The SNR of $\Delta B_{z,c}$ depends on the SNR of the MR image and the pulse-width of the injected current for a standard SE experiment, but these cannot both be increased simultaneously for a symmetric data acquisition, as the MR signal decays over time due to relaxation. Considering these limitations, Lee *et al* determined the optimal current injection time for a single echo SE MREIT experiment in 2007 (40). The current strength I_c = 20 mA was used in a saline phantom with bovine tissue. Again in 2007, an injected current nonlinear encoding (ICNE) SE sequence was proposed by Park *et al* (41). The ICNE sequence allows current injection also during the data acquisition period, which increases the SNR of the recorded $\Delta B_{z,c}$. The method causes artifacts in the measured $\Delta B_{z,c}$ in case of strong current injection, which can be fixed by post-processing. However, it is worth noting that in-vivo human brain MREIT can apply only very weak currents, so that current injection during data acquisition does not distort the measured $\Delta B_{z,c}$. In the same year, Kim *et al* conducted a post-mortem canine brain MREIT study (42) at 3 T with the ICNE sequence at 40 mA current strength. Concurrently, Kwon *et al* optimized the current pulse-width for the ICNE SE sequence and performed MREIT experiments in agar phantoms with 20 mA (43).

Motivated by the need to perform human MRI in reasonable scan times, Hamamura and Müftüler conducted a single shot SE echo planar imaging (EPI) MREIT study in 2008 (44). They also compared its performance with standard SE, and concluded that the SE EPI MREIT sequence may provide better quality images, as it allows more repetitions per unit time compared to standard SE.

In 2009, Kim *et al* performed the first human leg MREIT experiment by using an ICNE SE sequence with 10 mA (45). In the same year, Minhas *et al* conducted a simulation study for bSSFP MREIT, and proposed that the high phase sensitivity of bSSFP may be used to enhance the sensitivity (46). The study was extended later on by measuring in a cylindrical phantom, and reconstructing the bSSFP MREIT simulated images for a current injection of 5 mA (47).

In 2010, Han *et al* performed a canine brain multi-echo (ME) SE MREIT experiment with 20 mA (48), and compared the results with standard single-echo SE MREIT. Concurrently, Nam and Kwon proposed a modified MESE sequence for MREIT (49), which employed multi-gradient-echo acquisition. Experiments using a cylindrical phantom and a canine brain were performed with 10 mA. Both studies observed an SNR increase in the measured $\Delta B_{z,c}$ in the modified sequence results compared to standard SE cases. Nam and Kwon further reported an improved image quality due to the use of multi-gradient-echo acquisitions.

In the following year, the noise levels of MESE MREIT were studied by Minhas *et al* (50). Agar phantom and ex-vivo dog brain experiments were performed with 3 mA and a total scan time of 100 mins. They observed that the noise levels could be reduced down to around 0.1 nT in the phantom experiments and 1 nT in the dog experiments. In addition, the results were compared with standard single-echo SE and the superiority of MESE was demonstrated.

In the same year, Kranjc *et al* performed a two-shot rapid acquisition with relaxation enhancement (RARE) CDI study to monitor the electric field distribution during electroporation by means of MREIT (51,52). They performed experiments with 1000-2000 V very short voltage pulses in a cylindrical phantom. In 2012, Kim *et al* performed a multi-echo GRE MREIT study. They studied the noise levels of the different echoes and the optimal combination of the echoes, and developed a denoising algorithm (53). Experiments in a cylindrical phantom with 3 mA current were performed. Concurrently, a standard SE MREIT study was conducted by Arpınar *et al* (54). The experiments were performed in a non-homogenous cylindrical phantom, and results obtained at 200 μA and 5 mA were compared. Also in the same year, Seo *et al* theoretically studied the usefulness of gradient-recalled echo EPI (GRE-EPI) MREIT to reduce the scan time (55). Afterwards, Chauhan *et al* conducted a multi-echo GRE MREIT study and demonstrated that reducing the total scan time of an MREIT experiment is feasible without degrading the image quality by using partial fourier acquisition. In the study, experiments in a non-homogenous cylindrical phantom with 5 mA were performed (56).

In 2014, Jeong *et al* conducted a study on the effectiveness of using needle versus external electrodes in MREIT (57). In order to imitate needle electrodes, an acrylic cylinder wrapped in a carbon electrode was placed in the middle of a cylindrical phantom. MESE MREIT experiments with 5 mA were performed with both needle and surface electrodes, and a better efficiency of using needle electrodes was demonstrated. Concurrently, Kwon *et al* proposed using MREIT as a technique to monitor RF ablation (58). A temperature dependence of the conductivity was demonstrated in bovine muscle tissue, and the experiments were performed with a multi-echo GRE sequence. The same year, Oh *et al* performed a noise analysis of a spoiled multi-echo GRE MREIT sequence (59).

An optimal repetition time T_R was determined, which depended on the current pulse-width and the dephasing time T_2^*. In addition, validation experiments in a non-homogenous cylindrical phantom were performed with 10 mA current. Concurrently, Jeong *et al* demonstrated a new method to increase the SNR and quality of the reconstructed conductivity images by utilizing multiple RF receiver coils (60). A multi-echo GRE sequence was used and the experiments were performed in a non-homogenous cylindrical phantom with 10 mA current. In the same year, Kim *et al* studied conductivity imaging at two different frequencies via MREIT and MREPT by using a conventional SE sequence (61).
In 2016, Lee *et al* conducted the first steady-state free precession (SSFP) MREIT study (62). They investigated the performance of four different SSFP MREIT sequences by comparing them with a conventional SE MREIT sequence. They concluded that the best variant is the one that preserves only the FID component of the transverse magnetization (thus called SSFP-FID) and that uses current injection before the data acquisition. In their study, homogenous and non-homogenous cylindrical phantom experiments were performed with 10 and 5 mA current injection. Concurrently, Jeong *et al* demonstrated the possibility of improving the measurement sensitivity by means of a modified SSFP-FID variant where the current is injected until the end of readout (63). Non-homogenous cylindrical phantom experiments with 5 mA were performed and the results were compared with a standard spoiled GRE MREIT sequence. In 2016, the first in-vivo measurements of current-induced magnetic fields in the human brain were performed by Jog *et al* (64). They performed phantom, human limb, and brain experiments, and employed standard GRE field mapping acquisitions and combined them with direct currents injected at [0-1.5] mA in pseudorandom order. Near the electrodes, a current-induced magnetic field $\Delta B_{z,c}$ could be demonstrated. However, the sensitivity of the method was

insufficient to visualize the $\Delta B_{z,c}$ perturbations with high spatial resolution throughout the brain.

In 2017, we analyzed the sensitivity of $\Delta B_{z,c}$ measurements for SSFP-FID and MESE MREIT sequences (65). We proposed current injection within the entire T_R period in the SSFP-FID sequence to improve the sensitivity further, and evaluated the efficiency of both sequences, i.e. their sensitivity in relation to the total scan times. Spherical homogenous and cylindrical phantom experiments were performed with [0-1] mA current injections. The optimized sequence parameters for in-vivo brain imaging were determined for both sequences. In the same year, Lee *et al* proposed a new sequence, reverse dual-echo steady-state (rDESS) to estimate relaxation parameters and conductivity simultaneously (66). Magnitude and phase sensitivity of FID and echo pathways were simulated, and a higher phase sensitivity of SSFP-FID was demonstrated. Homogenous and non-homogenous cylindrical phantom experiments were performed with 10 mA current. The performance of the method is compared with the previously proposed SSFP-FID (62) and a conventional SE sequence. Concurrently, Kasinadhuni *et al* reported the second study on imaging the current flow in-vivo in the human head (67), performed in four healthy volunteers. A spoiled GRE sequence was used, and the applied current strength was 1.5 mA. These initial results were promising, but highlighted the need for further improvements of the measurement procedures and the sensitivity of the employed MRI sequences to allow for good quality and unambiguous $\Delta B_{z,c}$ images in a reasonable acquisition time.

In the same year, Chauhan *et al* conducted an MREIT study with a multi-shot EPI sequence to test the performance of a fast sequence compared to conventional methods (68). The performance of the method for different numbers of shots was also compared. The feasibility of the method was demonstrated in

experiments employing a non-homogenous cylindrical phantom with 10 mA current injection.

1.3 Objectives of the study

Up to now, single-echo spin echo (SE), multi-echo spin echo (MESE), gradient recalled echo (GRE), echo planar imaging (EPI), and steady-state free precession free induction decay (SSFP-FID) MREIT studies have been reported (11,44,49,50,62). In general, sequences with refocusing pulses are more robust to main field inhomogeneities and have a higher SNR, but imaging time is prolonged. On the other hand, gradient-echo sequences are more vulnerable to field inhomogeneities, and have less SNR due to the T_2^* signal decay, but are generally faster.

The $\Delta B_{z,c}$ sensitivity directly affects the accuracy and quality of the reconstructed current and conductivity distributions (50). It depends on the current strength, and only weak currents (1-2 mA) can be applied to the human brain in the low-frequency range (69). Therefore, reliable $\Delta B_{z,c}$ measurements are challenging in-vivo. Under this constraint, most of the previously developed MREIT sequences were not sensitive enough to enable in-vivo brain applications of MREIT. The goals of this thesis work were therefore to identify the most promising MRI sequence types for MREIT, to systematically analyze and optimize their sensitivity using theoretical analyses and phantom tests, and to adapt and validate the optimized sequences for robust imaging in in-vivo applications.

1.4 Outline

In **Chapter 1**, MREIT, MRCDI, and their potential biomedical applications were introduced. The chapter continued with a brief summary of the state-of-

the-art of the development of suited MR sequences, and motivated further sensitivity improvement. The objectives of the thesis were described, and the thesis outline is finally here given.

In **Chapter 2**, the fundamental theory of measuring current-induced magnetic fields by MRI is introduced, and the MRCDI method is explained. The conventional SE MRCDI method is selected for ease of explanation. In addition, the sensitivity of the method is explained briefly.

Chapter 3 is a summary of a sensitivity analysis of MESE and SSFP-FID MREIT methods for in-vivo human brain imaging. In this study, both MESE and SSFP-FID methods are optimized for in-vivo measurements of the human brain. The sensitivities of the methods are simulated and the simulation results validated in phantoms with realistic relaxation parameters. The sensitivity ranges demonstrated in this study for both sequence types render high-resolution in-vivo human brain MREIT feasible. This study was published as a journal paper in Magnetic Resonance in Medicine.

Chapter 4 summarizes the realization of in-vivo human brain MRCDI based on the previously optimized MESE and SSFP-FID sequences. Adaptations are demonstrated, which increase their robustness to physiological noise while keeping their high sensitivities to the current-induced phase shifts. Successful in-vivo measurements of the current-induced magnetic field $\Delta B_{z,c}$ were performed in several subjects, cable contributions were explored and corrected, and inter-individual $\Delta B_{z,c}$ differences observed. The current flow distributions were reconstructed from the measurements, and compared with the simulations. The sensitivity of the method is evaluated, and the results are compared with the only two published human brain in-vivo MRCDI studies (64,67). This work is presented as a submitted manuscript.

Finally, in **Chapter 5**, general discussions, conclusions and future perspectives are given.

2

BACKGROUND – MAGNETIC RESONANCE CURRENT DENSITY IMAGING (MRCDI)

2.1 Introduction

In this chapter, the fundamentals of measuring $\Delta B_{z,c}$, i.e. the magnetic field component parallel to the main magnetic field $B_{0,}$ and being induced by an externally injected current flow, is briefly explained. The factors, which may affect the sensitivity of the method, are briefly outlined. MRCDI and MREIT methods are also briefly discussed. However, details of the reconstruction algorithms are not given, as this topic is beyond the scope of this study. This section is written for readers with backgrounds in MRI physics and acquisition techniques.

2.2 Current injection during Magnetic Resonance Imaging (MRI)

We employ a device developed for transcranial weak current stimulation (TCS) to inject the electric current via surface electrodes into the brain. TCS is a neuromodulation technique, which can induce localized excitability changes in the stimulated brain areas (1). TCS employs weak electrical currents in the range

of [1-2] mA, and various current patterns have been tested, such as direct currents, alternating currents, or even randomly varying “noise” currents. Here, we use alternating currents in the low frequency range (i.e. [0-100] Hz), which are synchronized to the MR sequence. The photograph of the employed MRI-conditional TCS device (DC-STIMULATOR PLUS, neuroConn, Ilmenau, Germany) is shown in Figure 2.1.

Magnetic Resonance Imaging is a non-invasive imaging technique, which can provide high-resolution brain images. A typical 3T MRI scanner (PRISMA, Siemens Healthcare, Erlangen, Germany) is shown in Figure 2.2.

Figure 2.1: The employed MRI-conditional TCS device (DC-STIMULATOR PLUS, neuroConn, Ilmenau, Germany).

Figure 2.2: The employed 3T MRI scanner (PRISMA, Siemens Healthcare, Erlangen, Germany).

2.3 Current-induced magnetic field measurements by means of MRI

In this thesis, MRI measurements are combined with weak currents injected via surface electrodes. For a concise explanation of the basic theory, a conventional single SE CDI sequence is considered (11,12) (Figure 2.3). The sequence is composed of a 90˚ excitation pulse preceding a 180˚ refocusing pulse, which in combination with long echo and relaxation times makes the measured magnetization T_2-weighted (T_2w), with a high signal-to-noise ratio (SNR), and robust to field inhomogeneities. An external electrical current is injected into the subject in synchrony with the MRI sequence. The current induces an additional magnetic field, and its component $\Delta B_{z,c}$, which is parallel to the main magnetic field B_0, causes a small shift in the precession frequency of the magnetization. This causes a phase modulation in the acquired MRI signal and renders the measurement of $\Delta B_{z,c}$ feasible.

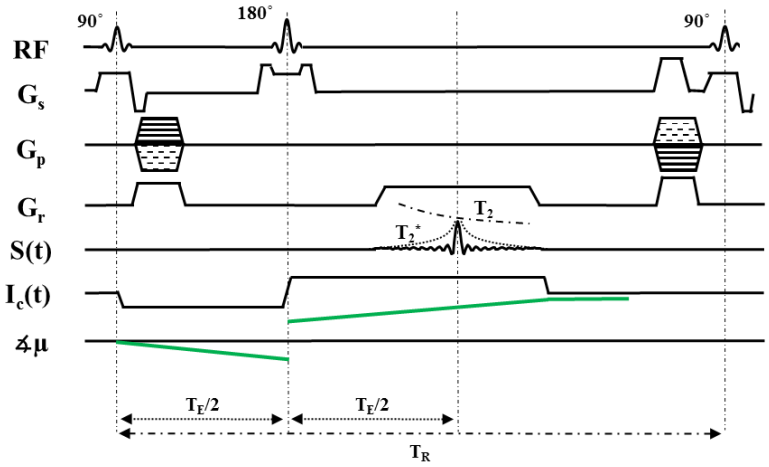

Figure 2.3: Sequence diagram of a conventional single-echo SE CDI (please note that the polarity of the injected current is inverted after the refocusing pulse, in order to provide continuous current-induced phase accumulation).

In a noise free environment, and neglecting the geometric and slice distortions due to the current injection during data acquisition and RF pulses, the measured MRI signal $S(k_x, k_y, t)$ in k-space is

$$S(k_x, k_y, t) = \int_{slice} \mu(x, y, t) e^{-j\gamma \Delta B_{z,c} t} e^{-j2\pi(k_x x + k_y y)} dx dy \qquad [1],$$

where $\mu(x, y, t)$ is the continuous transverse magnetization, and γ the gyromagnetic ratio of hydrogen, $\gamma = 2\pi \cdot 42.58$ MHz/T. Neglecting distortions is a valid assumption in our case, as only very weak electrical currents, i.e. limited to [1-2] mA (69), are allowed for in-vivo applications targeting the human brain. In that case, the current-induced precession frequency shifts are much smaller than the readout bandwidth.

Considering Equation [1] for a standard rectilinear k-space trajectory $2\pi k_x = \gamma G_x (t - T_E)$, where G_x is the readout gradient strength and T_E the echo time,

the measured current-induced magnetic field $\Delta B_{z,c}$ can be approximated as (12,41):

$$\Delta B_{z,c}(x,y) = \frac{\angle M^{+}(x,y) - \angle M^{-}(x,y)}{2\gamma T_E} \quad [2]$$

In Equation [2], $\angle M^{+}(x,y)$ and $\angle M^{-}(x,y)$ are the phases of complex MR images acquired with positive (+) and negative (-) current injection. Please note that the measurements are usually repeated twice with positive and negative current injection in order to eliminate systematic phase artifacts in the MR phase images and to increase SNR.

2.4 Sensitivity and efficiency of current-induced magnetic field measurements

A noise analysis of SE CDI has been performed by Scott *et al* (12), and the standard deviation of the measured phase image has been reported as $\sigma_\varphi = 1/(SNR\sqrt{2})$, where SNR is the signal-to-noise ratio of the MR magnitude image when only thermal noise is considered. Please note that the signal-to-noise ratio, SNR, of an MR image scales linearly with voxel size, the square root of number of excitations, and the square root of the readout sampling time. By combining σ_φ and Equation [2], the standard deviation of $\Delta B_{z,c}$ can be derived, and is given by:

$$\sigma_{\Delta B_{z,c}} = \frac{1}{2\gamma\, SNR\, T_E} \quad [3]$$

In general, MR sequences provide different SNR and differ in their sensitivity to current-induced phase, thereby providing different $\sigma_{\Delta B_{z,c}}$. In addition, the in-vivo application of human MRDCI requires performing the experiments in reasonable scan times. Therefore, it is useful to define the efficiency of the CDI experiment η_{seq} which relates its sensitivity to the required scan time T_{tot} (70):

$$\eta_{seq} = \frac{|\Delta B_{z,c}|}{\sigma_{\Delta B_{z,c}}\sqrt{T_{tot}}} \quad [4]$$

In Equation [4], the efficiency is defined as the sensitivity per square root of total scan time, so that the efficiency does not depend on the number of averages. A thorough analysis for the MESE and SSFP-FID sequences considered in this study can be found in Appendix A and B.

2.5 MR Current Density Imaging (MRCDI) and MR Electrical Impedance Tomography (MREIT)

As already mentioned in Chapter 1, MRCDI and MREIT are two imaging modalities proposed to obtain high-resolution measurements of the current density and ohmic conductivity distribution in the human body. The methods are delineated in Figure 2.4. As shown, they both combine externally injected currents and MRI. The experiments are repeated twice with positive (+) and negative (-) current injection. The phase-modulated complex MRI data are processed, and the current-induced magnetic field $\Delta B_{z,c}$ is calculated. Conventionally, current flow and conductivity reconstruction require all components of the current-induced magnetic field according to the Biot-Savart Law.

However, as subjects cannot be easily rotated to achieve repeated measurements at different orientations, MRCDI and MREIT algorithms using only $\Delta B_{z,c}$ to reconstruct the current density and ohmic conductivity have been proposed (see Section 1.2). MREIT algorithms are divided into two subgroups, $\vec{J}$-based and $\Delta B_{z,c}$-based algorithms. The $\vec{J}$-based algorithms use the reconstructed current density distribution, while the $\Delta B_{z,c}$-based algorithms are based directly on the measured $\Delta B_{z,c}$. The methodology and thorough analysis of the algorithms is beyond the scope of the study, and the interested reader is referred to, e.g. the reviews (20,29,33).

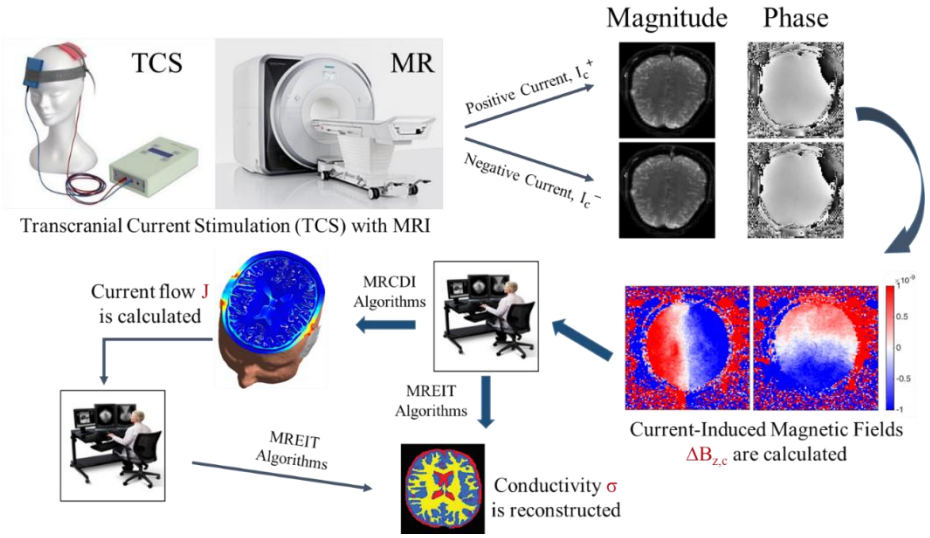

Figure 2.4: Schematic diagram of human brain MRCDI and MREIT.

3

SENSITIVITY ANALYSIS OF MAGNETIC FIELD MEASUREMENTS FOR MR ELECTRICAL IMPEDANCE TOMOGRAPHY (MREIT)

MR current density imaging and electrical impedance tomography (MRCDI and MREIT; see sections 2.2 and 2.3) are two emerging modalities, which can be used to determine the current flow and ohmic conductivity distribution inside the human body (11,12,33,71,72). They are based on the measurement of magnetic fields induced by a current that is injected into the body via surface electrodes. This thesis focusses on field measurements in-vivo in the human brain. The strength of the injected currents is limited to 1-2 mA in this case, so that the current-induced magnetic field is very weak and very sensitive measurement methods are needed. Furthermore, in-vivo human brain MREIT requires the use of reasonable scan times. While previous studies showed that high resolution and quality conductivity images can be acquired in phantoms, animals, and the human leg employing currents of 5 mA or higher, in-vivo measurements from the human brain still require more sensitive MR methods (33,42,48,64,67,73,74). Therefore, in this thesis, two MR sequence types were selected – multi-echo spin echo (MESE) and steady-state free precession free

induction decay (SSFP-FID) – for which reasonable sensitivities were demonstrated in prior studies. A thorough analysis of the two methods was performed using theoretical analyses and phantom measurements, with the aim of maximizing their sensitivities to current-induced phase changes in the MR images. In the studies listed in Appendix A and B, the analyses assessed the efficiency [1] of the two sequences for measuring the induced magnetic field changes, given by

$$\eta_{seq} = \frac{SNR_{\Delta B_{z,c}}}{\sqrt{T_{tot}}}, \quad [1]$$

where $SNR_{\Delta B_{z,c}}$ is the signal-to-noise ratio (SNR) of the current-induced magnetic field $\Delta B_{z,c}$, and T_{tot} is the total scan time. $SNR_{\Delta B_{z,c}}$ depends on the SNR of MR magnitude images and the phase sensitivity (12,13,62). The efficiency relates the achieved SNR to the required measurement time and is thus useful to optimize and quantitatively compare the performance of MR sequences.

Here, MESE was selected for its high SNR of the MR magnitude images and its robustness to magnetic field inhomogeneities, and SSFP-FID for its high phase sensitivity. The $SNR_{\Delta B_{z,c}}$ and the efficiency of both sequences were simulated and the sequences were optimized for the relaxation times of human brain tissue. The simulation results were verified in experiments employing a homogenous phantom with relaxation parameters T_1 and T_2 similar to brain tissue. For both sequences, optimal parameters were determined, which significantly improved their efficiency compared to the settings applied in prior studies. The sequences were also tested in a phantom with non-homogenous geometry. The demonstrated sensitivity levels were sufficient to render in-vivo human brain MREIT feasible.

This work was published as a journal paper, which can be found in Appendix B. Part of the work was also published as a conference abstract, which is listed in Appendix A.

4
IN-VIVO HUMAN BRAIN MRCDI

The aim in the second sub-study of the thesis was to demonstrate reliable measurements of current-induced magnetic fields in-vivo in the human brain. Once established, they will provide important information to validate and improve forward modeling schemes that are employed in transcranial brain stimulation (TBS) and electro- (EEG) and magnetoencephalography (MEG) to estimate the current flow distribution.

Recently developed MRCDI and MREIT techniques rendered the reconstruction of high quality current density and conductivity images from in-vivo measurements in the canine brain and human limb feasible (75,76). However, the applied electrical current strengths were much higher than the limits for in-vivo human brain applications (1-2 mA) (69). Correspondingly, only two studies report in-vivo measurements of current-induced magnetic fields in the human brain up to now. One research group employed standard field mapping sequences to measure the constant fields of direct currents (64). While the use of standard sequences has the advantage that 3D coverage can be readily achieved, this approach is not robust to slow temporal drifts of the MR signal which occur due to both technical and physiological reasons, inherently limiting the achievable sensitivity. Another research group has reported the first high resolution $\Delta B_{z,c}$ images of in-vivo measurements in the human brain (77). However, their

results do not show good reproducibility across participants, and in addition exhibit significant differences to simulated field distributions based on individualized FEM models. This raises doubts about the reliability of the presented results.

In the study performed here, I employed the previously optimized MESE and SSFP-FID sequences (see Section 3), and tested their performance for in-vivo measurements in a series of five experiments. First, their robustness to physiological noise was optimized using multi-gradient-echo readouts, allowing to maintain long echo times (MESE) and repetition times (SSFP-FID) needed to obtain a high sensitivity to the current-induced fields. The linearity of the measured $\Delta B_{z,c}$ with respect to the current strength was validated for both methods. The remaining part of the study is focused on the more efficient SSFP-FID sequence. A strong influence of magnetic stray fields on the $\Delta B_{z,c}$ images is demonstrated, caused by non-ideal paths of the feeding cables that are connected to the electrodes. In addition, a method to correct for these undesired influences is proposed and validated. Subsequently, the impact of the repetition time on measurement efficiency and image quality is evaluated. Finally, measurements with two different current injection profiles (right-left and anterior-posterior) are performed in five subjects. The results demonstrate reliable recordings of $\Delta B_{z,c}$ fields as weak as 1 nT, caused by currents of 1 mA strength. The $\Delta B_{z,c}$ measurements are compared with FEM simulations based on individualized head models. The $\Delta B_{z,c}$ measurements and FEM simulations are used to calculate current flow distributions, and the estimated current flow measurements and simulations are compared by means of a linear regression analysis. They show good correspondence, with an average coefficient of determination R^2 of 71%. Interestingly, the simulations underestimated the current strength on average by 24%. The outcome of this study is very promising and opens up the

possibility of exploring the usefulness of the new method across a wide range of applications. In particular, this comprises the systematic validation and optimization of numerical field simulations for TBS, EEG and MEG.
A submitted manuscript covering this work can be found in Appendix D. In addition, part of this work was published as a conference abstract, as listed in Appendix C.

5 GENERAL DISCUSSION AND CONCLUSIONS

The studies included in this thesis aimed at rendering in-vivo MRCDI measurements in the human brain feasible. Previous in-vivo studies demonstrated successful recordings of current-induced magnetic fields and current flow distributions in animals and the human limb at high quality and resolution, but only for high current strength exceeding 5 mA (see section 1.2). Two recent studies performed in-vivo MRCDI measurements in the human brain (64,77), as already discussed in Section 4. While these initial results were promising, they highlighted the need for further improvements of the measurement procedures and the sensitivity of the employed MRI sequences to allow for good quality and unambiguous $\Delta B_{z,c}$ images in a reasonable acquisition time. In contrast, the methods developed in this thesis allowed for the acquisition of reliable $\Delta B_{z,c}$ images in less than 10 minutes measurement time, and for a current strength as low as 1 mA. In the following, I summarize some key aspects that contributed to the successful realization of in-vivo MRCDI of the human brain, and discuss putative future directions.

5.1 MESE vs. SSFP-FID

There were two different MRCDI methods used in this thesis, MESE and SSFP-FID. MESE is a robust technique providing a high SNR of the MR magnitude images, which is an important factor for the sensitivity of MRCDI measurements and the acquired image quality. In this method, the phase accumulation of the complex transversal magnetization scales linearly with the strength and duration of the current-induced magnetic field. Surprisingly, the results of the optimization study demonstrate that the measurement efficiency of MESE is maximized for long repetition times of T_R = 1.5-2 s in order to allow for sufficient recovery of longitudinal magnetization. This introduces long dead times after the acquisition of each phase-encoding line, inherently limiting the achievable efficiency. The dead times could be used in the future to realize multi-slice acquisitions without a significant loss of efficiency. However, the performance of a multi-slice approach in the presence of physiological noise still has to be demonstrated.

In the absence of physiological noise, optimized SSFP-FID measurements were shown to be around three times more efficient than optimized MESE. The technique has a non-linear dependence of the accumulated phase on the current strength and duration, and benefits from the absence of dead times, which outweighs the SNR loss due to the additional T_2^* decay. From a practical point of view, a single measurement can be obtained in a much shorter scan time, so that the final $\Delta B_{z,c}$ image can be obtained by averaging several successive acquisitions. This allows for the identification and removal of corrupted single measurements to possibly improve the quality of the final magnetic field image.

The results indicate, that in the presence of physiological noise, SSFP-FID acquired at T_R = 80 ms is more efficient than for a theoretically optimal T_R = 120

ms. In that case, SSFP-FID is also moderately more efficient than MESE. However, the difference in efficiency is far lower in-vivo than in the phantom experiments, demonstrating a strong impact of physiological noise on the results.

5.2 Considerations on the sequence design

In the optimization study, the repetition time T_R, echo spacing T_{ES} and the number of spin-echoes N_{SE} of MESE were determined to provide the highest efficiency for in-vivo MRCDI of the human brain (Appendix B). The sequence employs crusher gradients in order to eliminate unwanted echo pathways and to keep only the primary spin-echo pathway to provide a linear phase increase. It was demonstrated that careful selection of the crusher areas and directions is important to robustly achieve the desired effect. The crusher pairs cause a diffusion weighting, but this is negligible as the distance between crusher pairs is very short (b-value $b<10$ s/mm^2 for the crusher pair with the largest areas). Despite the careful design of the crusher gradients and the good results, an additional empirical optimization of their areas may help to increase the SNR slightly further by increasing the time available for the readout. Finally, the slice profiles characteristic of the radio-frequency pulses should be measured and, if necessary, optimized when multi-slice acquisitions are desired, since even limited slice cross-talk may be detrimental.

For SSFP-FID, the repetition time T_R, the echo time T_E, and tip angle α were optimized to obtain the highest efficiency. The SSFP-FID sequence also employs spoiler gradients, which were conservatively chosen based on theoretical calculations to cause intra-voxel phase spread of at least 4π. Empirical optimization of the spoilers could reduce their duration, allowing for longer readouts and potentially improve SNR moderately. Furthermore, an optimization of the excitation pulses may provide better slice profiles. Finally, the SNR is highly

dependent on the field homogeneity. Therefore, advanced shimming techniques may help to provide high efficiency across the complete brain.

5.3 Cable-induced magnetic stray fields

The current flow in the cables that connect the surface electrodes to the current source causes a magnetic stray field, which affect the measured current-induced magnetic field. Ideally, the cable paths are fully parallel to the main magnetic field of the scanner, so that the cable-induced magnetic fields do not have a z-component. However, this is difficult to achieve in practice, due to the coil geometry, the head size and shape, and the electrode geometries. In our case, also the need to use equipment that was CE marked as medical device, contributed to the non-ideal cable pathways. The stray field and the magnetic field caused by the current flow inside the brain can easily be in a similar range. In the presented in-vivo study (Appendix D), a method was implemented and validated, which corrects for the stray field, based on tracking of the cable paths in structural images. While this method worked well, an optimal choice of cable paths is still desirable to increase the robustness of the overall measurement approach. Specifically, it should preferably be prevented that head motion changes the cable-induced stray fields, e.g. between the MRCDI measurements and the structural MRI used for reconstructing the cable paths.

5.4 Other Aspects

The in-vivo study in Appendix D demonstrated a clear effect of physiological noise on the MRCDI results. The control measurements without current injection exhibit spatially varying biases, which change between measurement repetitions. Pilot experiments revealed that the state of eyes (open or closed) has no effect on the measurements. However, jaw movements severely affected the quality of the MRCDI measurements, suggesting that also other motion due to

swallowing, breathing, or increased head movements due to discomfort during the current application play a role. In the in-vivo study, these effects were minimized by restricting the current strength to 1 mA and by carefully preparing the participants prior to the measurements.

In the studies in Appendix B and D, there were no eddy current effects observed in the MRCDI measurements. However, further increasing the number of gradient echoes, the slew rate, or employing echo planar imaging (EPI) readouts may cause eddy current related artefacts. Also flow-related artifacts were mostly absent. However, slice positions superior to the ventricles were chosen, and flow compensation methods may be required in the future when lower slices are selected. Finally, the amplitude and temporal accuracy of the current source affects the accuracy of the MRCDI measurements. However, the employed TCS stimulator was sufficiently good and its effects negligible compared to the aforementioned aspects.

5.5 Future perspectives

The MR sequences used in this thesis provided sufficient sensitivity to reliably observe current-induced magnetic fields in the range of 1 nT. However, the sensitivity can potentially be further improved by employing alternative methods such as balanced Steady-State Free Precession (bSSFP). Balanced SSFP sequences can have a phase sensitivity that is more than 10 times higher compared to standard methods (38). However, bSSFP is not robust to field inhomogeneities, and off-resonance effects can cause severe image artifacts and will decrease the phase sensitivity drastically.

The detrimental effects of subject motion could be minimized by employing faster sequences (78). However, it is unclear whether this can be achieved without decreasing the sensitivity to the current-induced phase changes. In addition,

novel motion correction methods could be used to counteract the impact of motion on the MRCDI results (79).

Finally, inhomogeneous current density distributions in the electrode pads may induce a significant stray field in brain regions near the electrodes. Therefore, in addition to correct for the cable-induced stray fields, more advanced methods may take stray field from the electrode pads into account.

REFERENCES

1. Nitsche MA, Paulus W. Excitability changes induced in the human motor cortex by weak transcranial direct current stimulation. J. Physiol. 2000;527:633–639.

2. Woods AJ, Antal A, Bikson M, et al. A technical guide to tDCS , and related non-invasive brain stimulation tools. Clin. Neurophysiol. 2016;127:1031–1048. doi: 10.1016/j.clinph.2015.11.012.

3. Opitz A, Paulus W, Will S, Antunes A, Thielscher A. Determinants of the electric field during transcranial direct current stimulation. Neuroimage 2015;109:140–150.

4. Thielscher A, Antunes A, Saturnino GB. Field modeling for transcranial magnetic stimulation: A useful tool to understand the physiological effects of TMS? Proc. Annu. Int. Conf. IEEE Eng. Med. Biol. Soc. EMBS 2015;2015–Novem:222–225. doi: 10.1109/EMBC.2015.7318340.

5. Thielscher A, Opitz A, Windhoff M. Impact of the gyral geometry on the electric field induced by transcranial magnetic stimulation. Neuroimage 2011;54:234–243.

6. Fear EC, Hagness SC, Meaney PM, Okoniewski M, Stuchly MA. Enhancing Breast Tumor Detection with Near-Field Imaging. IEEE Microw. Mag. 2002;3:48–56.

7. Morucci JP, Riguad B. Bioelectrical impedance techniques in medicine part III; Impedance imaging, medical applications. Crit. Rev. Biomed. Eng. 1996;24:655–677.

8. Mosher JC, Leahy RM, Lewis PS. EEG and MEG: Forward Solutions for Inverse Methods. IEEE Trans. Biomed. Eng. 1999;46:245–259.

9. Eyüboğlu BM. Electrical impedance imaging: Injected current electrical impedance imaging. WILEY - Encycl. Biomed. Eng. WILEY-Encyclopedia

Biomed. Eng. (Metin Akay, ed.) 2006;2:1195–1205.

10. Sadleir RJ, Grant SC, Silver X, Zhang SU, Woo EJ, Lee SY, Kim TS, Oh SH, Lee BI, Seo JK. Magnetic Resonance Electrical Impedance Tomography (MREIT) at 11 Tesla Field Strength : Preliminary Experimental Study. 2005;7:340–343.

11. Scott GC, Joy MLG, Armstrong RL, Henkelman RM. Measurement of nonuniform current density by magnetic resonance. IEEE Trans. Med. Imaging 1991;10:362–374.

12. Scott GC, Joy MLG, Armstrong RL, Henkelman RM. Sensitivity of magnetic-resonance current-density imaging. J. Magn. Reson. 1992;97:235–254.

13. Sadleir R, Grant S, Zhang SU, et al. Noise analysis in magnetic resonance electrical impedance tomography at 3 and 11 T field strengths. Physiol. Meas. 2005;26:875–84.

14. Joy M, Scott G, Henkelman M. In vivo Detection of Applied Electric Currents by Magnetic Resonance Imaging. Magn. Reson. Imaging 1989;7:89–94.

15. Joy ML, Lebedev VP, Gati JS. Imaging of current density and current pathways in rabbit brain during transcranial electrostimulation. IEEE Trans. Biomed. Eng. 1999;46:1139–49.

16. Birgül Ö, Eyüboğlu BM, Ider YZ. Magnetic Resonance-Conductivity Imaging Using 0.15 Tesla MRI Scanner. In: 2001 Proceedings of the 23rd Annual EMBS International Conference. ; 2001. pp. 3384–3387.

17. Pesikan P, Joy MLG, Scott GC, Henkelman RM. Two-dimensional current density imaging. IEEE Trans. Instrum. Meas. 1990;39:1048–1053. doi: 10.1109/19.65824.

18. Joy MLG. MR Current Density and Conductivity Imaging : The state of the art . 2004:5315–5319.

19. Göksu C, Sadighi M, Eroğlu HH, Eyüboğlu M. Realization of Magnetic Resonance Current Density Imaging at 3 Tesla. In: Annual International Conference of the IEEE Engineering in Medicine and Biology Society - EMBC. ; 2014. pp. 1115–1118.

20. Seo JK, Kwon O, Woo EJ. Magnetic resonance electrical impedance tomography (MREIT): conductivity and current density imaging. J. Phys. Conf. Ser. 2005;12:140–155. doi: 10.1088/1742-6596/12/1/014.

21. Oh SH, Lee B Il, Woo EJ, Lee SY, Cho MH, Kwon O, Seo JK. Conductivity and current density image reconstruction using harmonic Bz algorithm in

magnetic resonance electrical impedance tomography. Phys. Med. Biol. 2003;48:3101–3116. doi: 10.1088/0031-9155/48/19/001.

22. Joy MLG. MR current density and conductivity imaging: the state of the art. In: Conf Proc IEEE Eng Med Biol Soc. Vol. 7. ; 2004. pp. 5315–9. doi: 10.1109/IEMBS.2004.1404484.

23. Ider YZ, Birgül Ö, Oran ÖF, Arıkan O, Hamamura MJ, Müftüler T. Fourier transform magnetic resonance current density imaging (FT-MRCDI) from one component of magnetic flux density. Phys. Med. Biol. 2010;55:3177–3199. doi: 10.1088/0031-9155/55/11/013.

24. Ersöz A, Eyüboğlu BM. Magnetic resonance current density imaging using one component of magnetic flux density. Inverse Probl. Sci. Eng. 2017;21:184–196. doi: 10.1080/17415977.2012.683790.

25. Hoon Oh S, Kon Chun I, Yeol Lee S, Hyoung Cho M, Woong Mun C. A single current density component imaging by MRCDI without subject rotations. Magn. Reson. Imaging 2003;21:1023–1028. doi: 10.1016/S0730-725X(03)00213-3.

26. Park C, Lee B Il, Kwon OI. Analysis of recoverable current from one component of magnetic flux density in MREIT and MRCDI. Phys. Med. Biol. 2007;52:3001–13. doi: 10.1088/0031-9155/52/11/005.

27. Seo JK, Woo EJ. Magnetic Resonance Electrical Impedance Tomography. Soc. Ind. Appl. Math. 2011;53:40–68.

28. Woo EJ, Seo JK. Magnetic resonance electrical impedance tomography (MREIT) for high-resolution conductivity imaging. Physiol. Meas. 2008;29:R1-26. doi: 10.1088/0967-3334/29/10/R01.

29. Eyüboğlu BM. Magnetic Resonance Electrical Impedance Tomography. WILEY - Encycl. Biomed. Eng. WILEY-Encyclopedia Biomed. Eng. (Metin Akay, ed.) 2006;4:2154–62.

30. Birgül Ö, Eyüboğlu BM, Ider YZ. Experimental results for 2D magnetic resonance electrical impedance tomography (MR-EIT) using magnetic flux density in one direction. Phys. Med. Biol. 2003;48:3485–3504.

31. Seo JK, Woo EJ. Electrical tissue property imaging at low frequency using MREIT. IEEE Trans. Biomed. Eng. 2014;61:1390–1399.

32. Seo JK, Yoon J, Woo EJ, Kwon O. Reconstruction of Conductivity and Current Density Images Using Only One Component of Magnetic Field Measurements. IEEE Trans. Biomed. Eng. 2003;50:1121–1124.

33. Seo JK, Woo EJ. Magnetic Resonance Electrical Impedance Tomography (MREIT). Soc. Ind. Appl. Math. 2011;53:40–68.

34. Oh SH, Lee B Il, Woo EJ, Lee SY, Kim T-S, Kwon O, Seo JK. Electrical conductivity images of biological tissue phantoms in MREIT. Physiol. Meas. 2005;26:S279-88. doi: 10.1088/0967-3334/26/2/026.

35. Ozparlak L, Ider YZ. Induced current magnetic resonance-electrical impedance tomography. Physiol. Meas. 2005;26:S289-305. doi: 10.1088/0967-3334/26/2/027.

36. Hamamura MJ, Muftuler LT, Birgul O, Nalcioglu O. Measurement of ion diffusion using magnetic resonance electrical impedance tomography. Phys. Med. Biol. 2006;51:2753–62. doi: 10.1088/0031-9155/51/11/005.

37. Mikac U, Demsar F, Beravs K, Sersa I. Magnetic resonance imaging of alternating electric currents. Magn. Reson. Imaging 2001;19:845–856.

38. Bieri O, Maderwald S, Ladd ME, Scheffler K. Balanced alternating steady-state elastography. Magn. Reson. Med. 2006;55:233–41.

39. Sadleir R, Grant S, Zhang SU, Oh SH, Lee B Il, Woo EJ. High field MREIT: setup and tissue phantom imaging at 11 T. Physiol. Meas. 2006;27:S261-70.

40. Lee BI, Park C, Pyo HC, Kwon O, Woo EJ. Optimization of current injection pulse width in MREIT. Physiol. Meas. 2007;28:N1-7. doi: 10.1088/0967-3334/28/1/N01.

41. Park C, Lee B Il, Kwon O, Woo EJ. Measurement of induced magnetic flux density using injection current nonlinear encoding (ICNE) in MREIT. Physiol. Meas. 2007;28:117–27.

42. Kim HJ, Lee B Il, Cho Y, Kim YT, Kang BT, Park HM, Lee SY, Seo JK, Woo EJ. Conductivity imaging of canine brain using a 3 T MREIT system: postmortem experiments. Physiol. Meas. 2007;28:1341–53. doi: 10.1088/0967-3334/28/11/002.

43. Kwon OI, Lee B Il, Nam HS, Park C. Noise analysis and MR pulse sequence optimization in MREIT using an injected current nonlinear encoding (ICNE) method. Physiol. Meas. 2007;28:1391–404.

44. Hamamura MJ, Muftuler LT. Fast imaging for magnetic resonance electrical impedance tomography. Magn. Reson. Imaging 2008;26:739–45.

45. Kim HJ, Kim YT, Minhas AS, Jeong WC, Woo EJ. In Vivo High-Resolution Conductivity Imaging of the Human Leg Using MREIT : The First Human Experiment. 2009;28:1681–1687.

46. Minhas AS, Member S, Woo EJ, Lee SY. Magnetic Flux Density Measurement with Balanced Steady State Free Precession Pulse Sequence for MREIT: A Simulation Study. 2009:2276–2278.

47. Minhas AS, Woo EJ, Sadleir R. Simulation of MREIT using balanced steady state free precession (b-SSFP) pulse sequence. J. Phys. Conf. Ser. 2010;224. doi: 10.1088/1742-6596/224/1/012019.

48. Han YQ, Meng ZJ, Jeong WC, Kim YT, Minhas AS, Kim HJ, Nam HS, Kwon O, Woo EJ. MREIT conductivity imaging of canine head using multi-echo pulse sequence. J. Phys. Conf. Ser. 2010;224:12078. doi: 10.1088/1742-6596/224/1/012078.

49. Nam HS, Kwon OI. Optimization of multiply acquired magnetic flux density B(z) using ICNE-Multiecho train in MREIT. Phys. Med. Biol. 2010;55:2743–59.

50. Minhas AS, Jeong WC, Kim YT, Han Y, Kim HJ, Woo EJ. Experimental Performance Evaluation of Multi-Echo ICNE Pulse Sequence in Magnetic Resonance Electrical Impedance Tomography. Magn. Reson. Med. 2011;66:957–65.

51. Kranjc M, Bajd F, Serša I, Miklav D. Magnetic Resonance Electrical Impedance Tomography for Monitoring Electric Field Distribution During Tissue Electroporation. IEEE Trans. Biomed. Eng. 2011;30:1771–1778.

52. Kranjc M, Bajd F, Sersa I, Woo EJ, Miklavcic D. Ex vivo and in silico feasibility study of monitoring electric field distribution in tissue during electroporation based treatments. PLoS One 2012;7:e45737. doi: 10.1371/journal.pone.0045737.

53. Kim MN, Ha TY, Woo EJ, Kwon OI. Improved conductivity reconstruction from multi-echo MREIT utilizing weighted voxel-specific signal-to-noise ratios. Phys. Med. Biol. 2012;57:3643–59. doi: 10.1088/0031-9155/57/11/3643.

54. Arpinar VE, Hamamura MJ, Degirmenci E, Muftuler LT. MREIT experiments with 200 μA injected currents: a feasibility study using two reconstruction algorithms, SMM and harmonic Bz. Phys. Med. Biol. 2012;57:4245–61. doi: 10.1088/0031-9155/57/13/4245.

55. Seo JK, Kim D-H, Lee J, Kwon OI, Sajib SZK, Woo EJ. Electrical tissue property imaging using MRI at dc and Larmor frequency. Inverse Probl. 2012;28:84002. doi: 10.1088/0266-5611/28/8/084002.

56. Chauhan M, Jeong WC, Kim HJ, Kwon OI, Woo EJ. Optimization of magnetic flux density for fast MREIT conductivity imaging using multi-echo interleaved partial fourier acquisitions. Biomed. Eng. Online 2013;12:82. doi:

10.1186/1475-925X-12-82.

57. Jeong WC, Sajib SZK, Kim HJ, Kwon OI. Focused Current Density Imaging Using Internal Electrode in Magnetic Resonance Electrical Impedance Tomography (MREIT). IEEE Trans. Biomed. Eng. 2014;61:1938–1946.

58. Kwon OI, Chauhan M, Kim HJ, Jeong WC, Wi H, Oh TI, Woo EJ. Fast conductivity imaging in magnetic resonance electrical impedance tomography (MREIT) for RF ablation monitoring. Int. J. Hyperth. 2014;30:447–455. doi: 10.3109/02656736.2014.966337.

59. Oh TI, Jeong WC, Kim JE, Sajib SZK, Kim HJ, Kwon OI, Woo EJ. Noise analysis in fast magnetic resonance electrical impedance tomography (MREIT) based on spoiled multi gradient echo (SPMGE) pulse sequence. Phys. Med. Biol. 2014;59:4723–38. doi: 10.1088/0031-9155/59/16/4723.

60. Jeong WC, Chauhan M, Sajib SZK, Kim HJ, Serša I, Kwon OI, Woo EJ. Optimization of magnetic flux density measurement using multiple RF receiver coils and multi-echo in MREIT. Phys. Med. Biol. 2014;59:4827–44. doi: 10.1088/0031-9155/59/17/4827.

61. Kim HJ, Jeong WC, Sajib SZK, Kim MO, Kwon OI, Je Woo E, Kim DH. Simultaneous imaging of dual-frequency electrical conductivity using a combination of MREIT and MREPT. Magn. Reson. Med. 2014;71:200–208. doi: 10.1002/mrm.24642.

62. Lee H, Jeong WC, Kim HJ, Woo EJ, Park J. Alternating steady state free precession for estimation of current-induced magnetic flux density: A feasibility study. Magn. Reson. Med. 2016;75:2009–2019.

63. Jeong WC, Lee MB, Sajib SZK, Kim HJ, Kwon OI, Woo EJ. Enhanced magnetic flux density mapping using coherent steady state equilibrium signal in MREIT. AIP Adv. 2016;6:35121. doi: 10.1063/1.4942669.

64. Jog M V, Smith RX, Jann K, Dunn W, Lafon B, Truong D, Wu A, Parra L, Bikson M, Wang DJJ. In-vivo Imaging of Magnetic Fields Induced by Transcranial Direct Current Stimulation (tDCS) in Human Brain using MRI. Sci. Rep. 2016;6:34385. doi: 10.1038/srep34385.

65. Göksu C, Scheffler K, Ehses P, Hanson LG, Thielscher A. Sensitivity Analysis of Magnetic Field Measurements for Magnetic Resonance Electrical Impedance Tomography (MREIT). Magn. Reson. Med. 2017;0. doi: 10.1002/mrm.26727.

66. Lee H, Sohn C, Park J. Current-Induced Alternating Reversed Dual-Echo-Steady-State for Joint Estimation of Tissue Relaxation and Electrical Properties.

Magn. Reson. Med. 2017;78:107–120. doi: 10.1002/mrm.26350.

67. Kasinadhuni AK, Indahlastari A, Chauhan M, Schär M, Mareci TH, Sadleir RJ. Imaging of current flow in the human head during transcranial electrical therapy. Brain Stimul. 2017:1–9. doi: 10.1016/j.brs.2017.04.125.

68. Chauhan M, Shankar RV, Kumar NA, Kodibagkar VD, Sadleir R. Multishot Echo-Planar MREIT for Fast Imaging of Conductivity , Current Density , and Electric Field Distributions. Magn. Reson. Med. 2017;0:1–12. doi: 10.1002/mrm.26638.

69. Utz KS, Dimova V, Oppenländer K, Kerkhoff G. Electrified minds: Transcranial direct current stimulation (tDCS) and Galvanic Vestibular Stimulation (GVS) as methods of non-invasive brain stimulation in neuropsychology-A review of current data and future implications. Neuropsychologia 2010;48:2789–2810.

70. Pohmann R, von Kienlin M, Haase A. Theoretical evaluation and comparison of fast chemical shift imaging methods. J. Magn. Reson. 1997;129:145–160.

71. Eyüboğlu BM. Magnetic Resonance Current Density Imaging. WILEY-Encyclopedia Biomed. Eng. WILEY-Encyclopedia Biomed. Eng. (Metin Akay, ed.) 2006;4:2147–53.

72. Eyüboğlu BM, Reddy R, Leigh JS. Imaging electrical current density using nuclear magnetic resonance. ELEKTRİK 1998;6:201–214.

73. Kim YT, Meng Z, Minhas AS, Kim HJ, Woo EJ, Lim CY, Park HM. In vivo MREIT conductivity imaging of canine brain to evaluate ischemia and abscess. 2011 8th Int. Symp. Noninvasive Funct. Source Imaging Brain Hear. 2011 8th Int. Conf. Bioelectromagn. 2011:44–47. doi: 10.1109/NFSI.2011.5936817.

74. Kim HJ, Kim YT, Jeong WC, Minhas AS, Lim CY, Park HM, Woo EJ. Conductivity imaging of canine body using 3T magnetic resonance electrical impedance tomography (MREIT) system. Sci. Iran. 2011;18:1505–1510. doi: 10.1016/j.scient.2011.08.023.

75. Kim YT, Minhas AS, Meng Z, Kim HJ, Woo EJ. Conductivity imaging of human lower extremity using MREIT with multi-echo pulse sequence and 3 mA imaging current. 2011 8th Int. Symp. Noninvasive Funct. Source Imaging Brain Hear. 2011 8th Int. Conf. Bioelectromagn. 2011:48–52. doi: 10.1109/NFSI.2011.5936818.

76. Kim HJ, Oh TI, Kim YT, et al. In vivo electrical conductivity imaging of a canine brain using a 3 T MREIT system. Physiol. Meas. 2008;29:1145–55. doi: 10.1088/0967-3334/29/10/001.

77. Kasinadhuni AK, Indahlastari A, Chauhan M, Scär M, Mareci TH, Sadleir RJ. Imaging of current flow in the human head during transcranial electrical therapy. Brain Stimul. 2017;10:764–772. doi: 10.1016/j.brs.2017.04.125.

78. Hargreaves BA. Rapid Gradient-Echo Imaging. J. Magn. Reson. Imaging 2012;36:1300–1313. doi: 10.1002/jmri.23742.

79. Maclaren J, Armstrong BSR, Barrows RT, et al. Measurement and Correction of Microscopic Head Motion during Magnetic Resonance Imaging of the Brain. PLoS One 2012;7:e48088. doi: 10.1371/journal.pone.0048088.

A APPENDIX

EFFICIENCY ANALYSIS OF MAGNETIC FIELD MEASUREMENT FOR MR ELECTRICAL IMPEDANCE TOMOGRAPHY (MREIT)

The following abstract was accepted for the annual scientific meeting of European Society for Magnetic Resonance in Medicine and Biology (ESMRMB) 2016.

Efficiency Analysis of Magnetic Field Measurement for MR Electrical Impedance Tomography (MREIT)

Cihan Göksu[1-2], Lars G. Hanson[1-2], Philipp Ehses[3-4], Klaus Scheffler[3-4], and Axel Thielscher[1-2-3]

[1] Danish Research Centre for Magnetic Resonance, Centre for Functional and Diagnostic Imaging and Research, Copenhagen University Hospital Hvidovre, Denmark, [2] Biomedical Engineering Group, DTU Elektro, Technical University of Denmark, Kgs Lyngby, Denmark, [3] High-Field Magnetic Resonance Center, Max-Planck-Institute for Biological Cybernetics, Tübingen, Germany, [4] Department of Biomedical Magnetic Resonance, University of Tübingen, Tübingen, Germany

Introduction: MREIT is an emerging method to measure the ohmic tissue conductivities, with several potential biomedical applications. Its sensitivity depends on the magnitude of the applied current, which is limited to 1-2 mA in the human brain [1, 2]. This renders in-vivo applications challenging. Here, we aim to analyze and optimize the efficiency of two MREIT pulse sequences for in-vivo brain imaging.

Theory and Methods: The electrical current injected into the subject creates an additional magnetic field ($\Delta B_{z,c}$) that can be detected from the phase of the magnetization [3]. Multi-Echo Spin Echo (MESE; Fig. 1a) and Steady-State Free Precession Free Induction Decay (SSFP-FID; Fig. 1b) are two sensitive MREIT pulse sequences. The efficiencies of MESE and SSFP-FID $\Delta B_{z,c}$ measurements ($\eta_{\Delta B_{z,c}}$) are defined as the signal-to-noise ratios (SNRs) per square root measurement time as in equations (1, 2), where N_{echo}, γ, SNR_n, T_{ES}, τ_π, $\tau_{\pi/2}$, μ, and T_{tot} are total number of echoes, gyromagnetic ratio, SNR of the n^{th} echo, echo spacing, RF pulse widths, transverse magnetization, and total measurement time, respectively [4, 5].

Results: The MESE efficiency is simulated, considering T1, T2, and T2* relaxation in the SNR_n. The simulations are experimentally validated for 0.5 mA injection current I_c in a doped saline filled spherical homogenous phantom, 10 cm in diameter (T1 = 1 s, T2 = 100 ms). Comparisons are shown in Fig. 2. The simulation results for three SSFP-FID variants (Fig. 1b; first two as in [4]; additional SSFP-FID3 with current injection in the entire TR period) are shown in Fig. 3a. The efficiency of SSFP-FID3, the most sensitive of the three variants, is simulated and experimentally validated for 1 mA in the same phantom. The compared efficiency results are shown in Figure 3b-g. All simulations are performed using rotation matrices, and cross-checked with the analytical equations.

Discussion and Conclusion: The measured and simulated efficiency maps for the MESE and SSFP-FID experiments are in good agreement. The most efficient regions for the MESE and SSFP-FID3 are N_{echo} = [2, 3], T_{ES} = [60 - 100] ms, and TE = [60 - 90] ms, TR = [120 - 180] ms for $\alpha = 20^\circ$, respectively. For single echo acquisitions, B_0 inhomogeneities and the low bandwidth per pixel at these long T_{ES} and TR create geometric image distortions. This can be fixed by multi-echo summation with a slight decrease in efficiency. Both sequences are promising for testing in in-vivo applications.

Acknowledgements: The project is supported by Lundbeck foundation with grant number R118-A11308.

References: [1] C. Göksu et al., EMBC 2014, 1115-8; [2] K. S. Utz et al., Neuropsychologia, 48:2789–810 (2010); [3] G. C. Scott and M. L. G. Joy, IEEE Trans. Med. Imaging, 10:362–74 (1991); [4] H. Lee et al., Magn. Reson. Med. (2015); [5] H. S. Nam and O. I. Kwon, Phys. Med. Biol., 55:2743–59 (2010).

$$\eta^{MESE}_{\Delta B_{z,c}} = \frac{\Delta B_{z,c}\sqrt{\sum_{n=1}^{N_{echo}} 2\left\{\gamma SNR_n\left[(T_{ES}-\tau_\pi)n-\frac{\tau_{\pi/2}}{2}\right]\right\}^2}}{\sqrt{T_{tot}}} \quad (1)$$

$$\eta^{SSFPFID}_{\Delta B_{z,c}} = \frac{\Delta B_{z,c} SNR \left.\frac{\partial \angle \mu}{\partial \Delta B_{z,c}}\right|_{\Delta B_{z,c}=0}}{\sqrt{T_{tot}}} \quad (2)$$

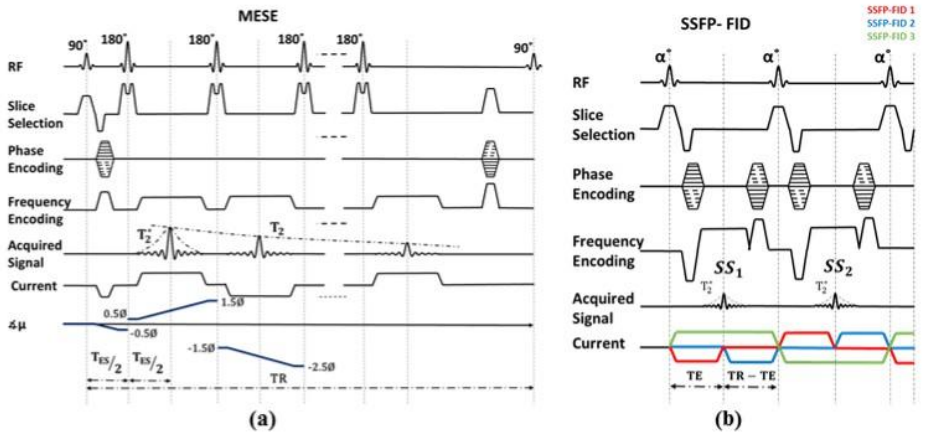

Figure 1. The pulse sequence diagrams: (a) MESE, (b) SSFP-FID variants

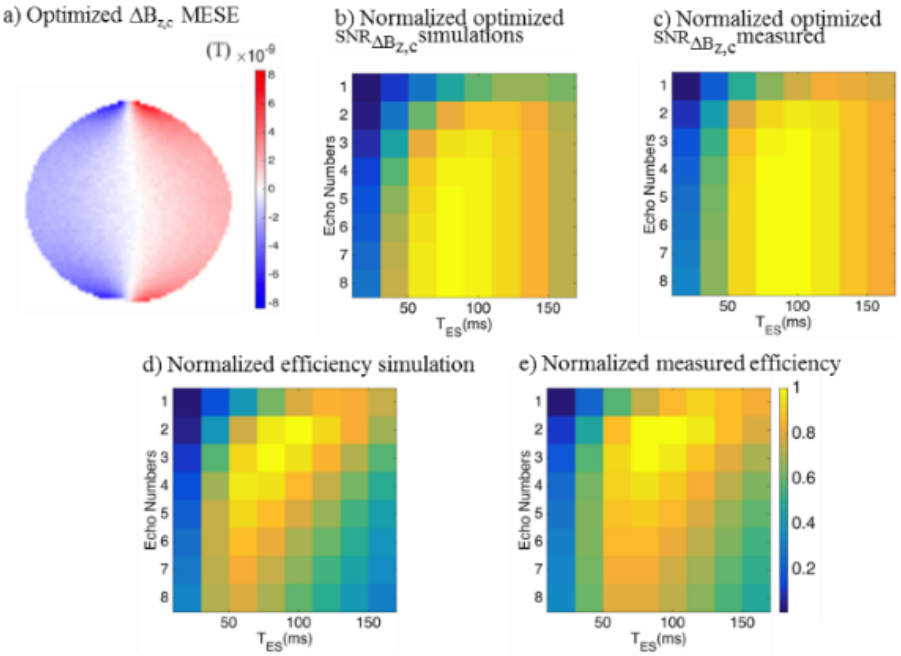

Figure 2. MESE experimental and simulation results: (a) Optimized $\Delta B_{z,c}$ MESE image for N_{echo} = 1-8, T_{ES} = 20 ms, TR = 670 ms, BW = 125 Hz/px, N_{avg} = 1, I_c = 0.5 mA, (b) normalized optimized $SNR_{\Delta B_{Z,c}}$ simulations, (c) normalized optimized $SNR_{\Delta B_{Z,c}}$ measured, (d) normalized efficiency simulation, and (e) normalized measured efficiency.

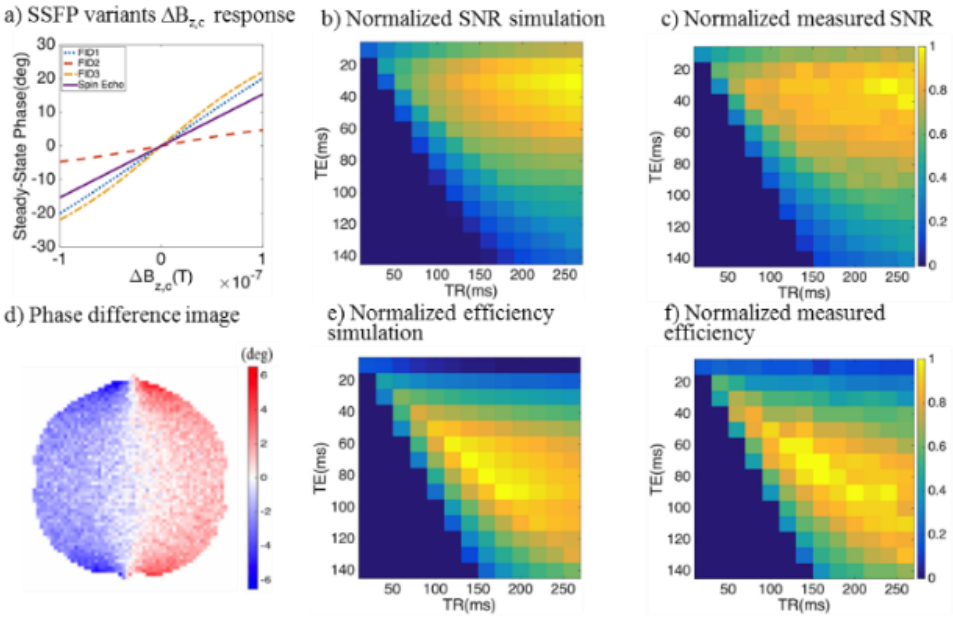

Figure 3. SSFP-FID3 experimental and simulation results: (a) SSFP variants $\Delta B_{z,c}$ response for α = 60˚, TE = 10 ms, TR = 20 ms, (b) normalized SNR of magnitude image simulation, (c) normalized measured SNR of magnitude image, (d) normalized phase difference image of two alternating steady-state for α = 20˚, TE = 10 ms, TR = 20 ms, BW = 64 Hz/px, N_{avg} = 2, I_c = 1 mA, (e) efficiency simulation, and (f) measured efficiency

B APPENDIX

SENSITIVITY ANALYSIS OF MAGNETIC FIELD MEASUREMENTS FOR MAGNETIC RESONANCE ELECTRICAL IMPEDANCE TOMOGRAPHY (MREIT)

The following paper has been published in Magnetic Resonance in Medicine (published online prior to inclusion in an issue, DOI: 10.1002/mrm.26727).

FULL PAPER

Magnetic Resonance in Medicine 00:00–00 (2017)

Sensitivity Analysis of Magnetic Field Measurements for Magnetic Resonance Electrical Impedance Tomography (MREIT)

Cihan Göksu,[1,2] Klaus Scheffler,[3,4] Philipp Ehses,[3,4] Lars G. Hanson,[1,2†] and Axel Thielscher[1,2,3†*]

Purpose: Clinical use of magnetic resonance electrical impedance tomography (MREIT) still requires significant sensitivity improvements. Here, the measurement of the current-induced magnetic field ($\Delta B_{z,c}$) is improved using systematic efficiency analyses and optimization of multi-echo spin echo (MESE) and steady-state free precession free induction decay (SSFP-FID) sequences.

Theory and Methods: Considering T_1, T_2, and T_2^* relaxation in the signal-to-noise ratios (SNRs) of the MR magnitude images, the efficiency of MESE and SSFP-FID MREIT experiments, and its dependence on the sequence parameters, are analytically analyzed and simulated. The theoretical results are experimentally validated in a saline-filled homogenous spherical phantom with relaxation parameters similar to brain tissue. Measurement of $\Delta B_{z,c}$ is also performed in a cylindrical phantom with saline and chicken meat.

Results: The efficiency simulations and experimental results are in good agreement. When using optimal parameters, $\Delta B_{z,c}$ can be reliably measured in the phantom even at injected current strengths of 1 mA or lower for both sequence types. The importance of using proper crusher gradient selection on the phase evolution in a MESE experiment is also demonstrated.

Conclusion: The efficiencies observed with the optimized sequence parameters will likely render in-vivo human brain MREIT feasible. **Magn Reson Med 000:000–000, 2017.** **© 2017 International Society for Magnetic Resonance in Medicine.**

Key words: efficiency analysis; magnetic resonance electrical impedance tomography; multi-echo spin echo; steady-state free precession; sequence optimization

INTRODUCTION

Magnetic resonance current density imaging (MRCDI) and magnetic resonance electrical impedance tomography (MREIT) are two emerging imaging modalities, which combine MRI with externally applied currents (either direct current or alternating current at low frequencies combined with repeated refocusing pulses (1)) to reconstruct the current density distribution and ohmic conductivity variation inside body tissue (2–7). This may open up novel ways to characterize pathological tissue (8). In addition, better knowledge of the conductivity distribution would allow improving the accuracy of source localization methods for electroencephalography and magnetoencephalography (9) and enable better spatial targeting of neurostimulation methods (10,11). However, MRCDI and MREIT are still hampered by their low sensitivity, which prevents their clinical usage.

In both modalities, electrical current is applied in synchrony with the MRI pulse sequence. The current flow induces a magnetic field distribution in the body, and the component of the induced magnetic field ($\Delta B_{z,c}$) which is parallel to the main magnetic field (B_0) creates a phase perturbation in the MRI signal that can be measured (5). The sensitivity of the $\Delta B_{z,c}$ measurement directly affects the accuracy and quality of the reconstructed current and conductivity distributions (12). However, a reliable $\Delta B_{z,c}$ measurement in in-vivo situations is crucial and challenging as only weak currents can be applied to the human body in the low frequency range, e.g. around 1-2 mA for brain studies (13). Optimized MR sequences which allow for efficient $\Delta B_{z,c}$ measurements within clinically relevant scan times are thus important to enable in-vivo applications of MRCDI and MREIT.

Up to now, single-echo spin echo (SE), multi-echo spin echo (MESE), gradient recalled echo, echo planar imaging, and steady-state free precession free induction decay (SSFP-FID) MREIT experiments have been performed (5,14–19). Sequences with refocusing pulses are more robust to main field inhomogeneities and have a higher signal-to-noise ratio (SNR), but imaging time is prolonged. On the other hand, the gradient-echo sequences are more vulnerable to main field inhomogeneities and have less SNR attributed to T_2^* decay, but are generally faster.

In this study, systematic efficiency analyses of two sensitive sequences (MESE and SSFP-FID) are performed, thereby considering the impact of T_1, T_2, and T_2^* relaxation and radiofrequency (RF) imperfections on

[1]Danish Research Center for Magnetic Resonance, Center for Functional and Diagnostic Imaging and Research, Copenhagen University Hospital, Hvidovre, Denmark.

[2]Center for Magnetic Resonance, DTU Elektro, Technical University of Denmark, Kgs Lyngby, Denmark.

[3]High-Field Magnetic Resonance Center, Max-Planck-Institute for Biological Cybernetics, Tübingen, Germany.

[4]Department of Biomedical Magnetic Resonance, University of Tübingen, Tübingen, Germany.

Grant sponsor: Lundbeck Foundation; Grant numbers: R118-A11308; R59 A5399 (PI Hartwig Siebner).

*Correspondence to: Axel Thielscher, Danish Research Center for Magnetic Resonance, Center for Functional and Diagnostic Imaging and Research, Copenhagen University Hospital Hvidovre, Section 714, Kettegaard Allé 30, 2650 Hvidovre, Denmark. E-mail: axelt@drcmr.dk

†These authors contributed equally to this work.

Received 30 November 2016; revised 2 March 2017; accepted 29 March 2017

DOI 10.1002/mrm.26727

Published online 00 Month 2017 in Wiley Online Library (wileyonlinelibrary.com).

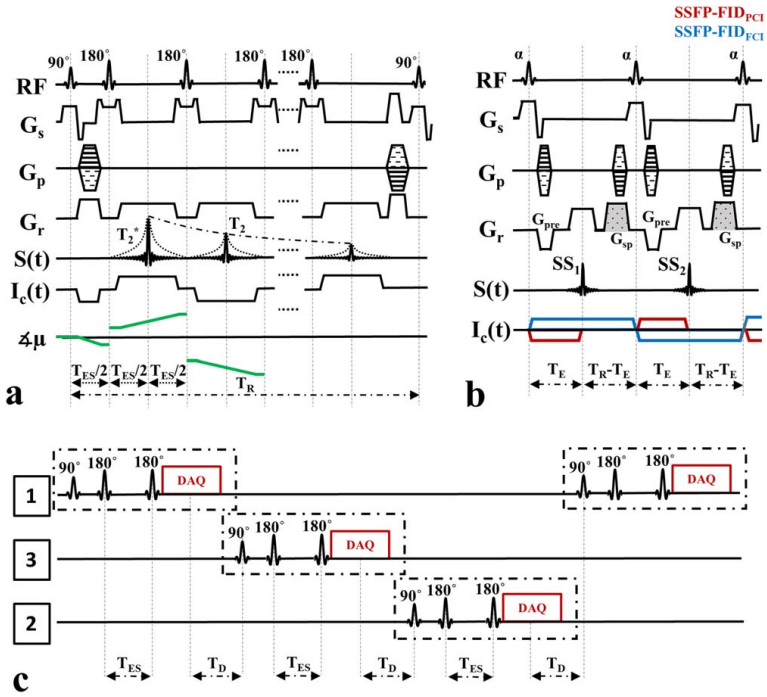

FIG. 1. (**a**) Diagram of the MESE MREIT pulse sequence with equal and symmetric echo spacing. The sequence is composed of a 90° excitation pulse preceding repetitive 180° refocusing pulses, so that multiple echoes are created. Crusher gradients are used to preserve the desired echo pathways, while eliminating unwanted ones caused by nonideal refocusing pulses (27). At the end of the sequence, phase encoding rewinder and spoiler gradients are used to eliminate unwanted effects of remaining transverse magnetization. This is followed by a dead time T_D after which the slice (or the next slice for multi-slice measurements; see subfigure **c**) is excited again. The injected bipolar electrical current is synchronized with the RF pulses, so that the phase of the continuous complex transverse magnetization ($\measuredangle\mu$) increases linearly over time. (**b**) Sequence diagrams of the two SSFP-FID variants. An SSFP sequence is composed of repetitive constant tip angle and in-phase excitation pulses, where the interval T_R between each RF pulse is constant. These conditions are enough to reach a steady state (30). In case of a bipolar electrical current injection in synchrony with the SSFP-FID sequence, the continuous transverse magnetization phase evolves in opposite directions in odd and even T_R periods, which induces two different steady-state conditions with opposite current-induced phases. Please note that unlike in the original study of Lee et al (19), we decided to inject electrical current until T_E for SSFP-FID$_{PCI}$ in order to test its most efficient case. On the other hand, the current is injected within the entire T_R period in SSFP-FID$_{FCI}$. (**c**) Interleaved multi-slice acquisition of MESE.

SNR. All results are experimentally validated in a saline-filled homogenous spherical phantom with relaxation parameters similar to brain tissue. For MESE (Fig. 1a,c), it is simulated how efficiency depends on the relevant sequence parameters, which are shown to be the echo spacing T_{ES}, the number of echoes N_{echo}, and the dead time T_D. The efficiency change for multi-slice acquisition is subsequently assessed. In addition, the importance of selecting the proper echo pathways on the phase evolution is demonstrated. Furthermore, two different SSFP-FID variants (Fig. 1b) are simulated and compared. The more efficient variant is subsequently optimized with respect to the utilized tip angle α, echo time T_E, and repetition time T_R. In final experiments, the efficiencies of the optimized MESE and SSFP-FID sequences are directly compared, and $\Delta B_{z,c}$ measurements are performed for both MESE and SSFP-FID for a nonhomogeneous phantom.

THEORY

Efficiency of an MREIT Experiment

We use the following notation of efficiency η_{seq} to characterize the performance of a sequence (20), thereby relating the SNR of the acquired $\Delta B_{z,c}$ image to the required total scan time T_{tot} (Eq. 1):

$$\eta_{seq} = \frac{SNR_{\Delta B_{z,c}}}{\sqrt{T_{tot}}} = \frac{|\Delta B_{z,c}|}{\sigma_{\Delta B_{z,c}}\sqrt{T_{tot}}} \quad [1]$$

$|\Delta B_{z,c}|$ is the magnitude of the current-induced magnetic field and $\sigma_{\Delta Bz,c}$ the noise standard deviation of $\Delta B_{z,c}$. Please note that η_{seq} varies spatially, because $\Delta B_{z,c}$ depends on the injected current strength, electrode placement, electrode geometry, and conductivity distribution. In addition, $\sigma_{\Delta Bz,c}$ depends on the SNR of the MR image and the phase sensitivity of MRI sequence. In the following, we derive how the

efficiency depends on sequence and tissue relaxation parameters. The resulting equations are then used to determine the optimal parameter settings by numerical simulations.

MESE MREIT

The pulse sequence of a standard MESE MREIT sequence with equal and symmetric echo spacing is shown in Figure 1a,c. For current injection within periods free of RF pulses, the measured $\Delta B_{z,c}$ from each single echo and its noise variance were reported previously (17,21,22) and are given by Equations [2] and [3]:

$$\Delta B_{z,c}^{n} = \frac{\angle M_n{}^{+} - \angle M_n{}^{-}}{2\gamma[(T_{ES} - \tau_\pi)n - 0.5\tau_{\pi/2}]} \quad [2]$$

$$\mathrm{Var}\{\Delta B_{z,c}^{n}\} = \frac{1}{4\gamma^2 SNR_n^2[(T_{ES} - \tau_\pi)n - 0.5\tau_{\pi/2}]^2} \quad [3]$$

$\angle M_n{}^{+}$ and $\angle M_n{}^{-}$ are the phase of the complex MR images from the nth echo with positive (+) and negative (–) constant current injection, SNR_n is the SNR of the magnitude image from the nth echo, and γ denotes the gyromagnetic ratio. τ_π and $\tau_{\pi/2}$ are the durations of the 180° and 90° RF pulses where current is not applied.

The $\Delta B_{z,c}$ measurements can be optimally combined across echoes by weighting each by the inverse of its variance. Normalizing by a common factor to ensure that the weights across all echoes sum to 1, and adding the weighted images, the noise variance of the combined $\Delta B_{z,c}$ is then given by Equation [4] (17):

$$\mathrm{Var}\{\Delta B_{z,c}^{comb}\} = \frac{1}{\sum_{n=1}^{N_{echo}} 4\gamma^2 SNR_n^2[(T_{ES} - \tau_\pi)n - 0.5\tau_{\pi/2}]^2} \quad [4]$$

Applying Equation [4] to Equation [1] finally gives the efficiency of measuring the combined $\Delta B_{z,c}$ (Eq. [5]):

$$\eta_{MESE} = \frac{|\Delta B_{z,c}^{comb}|}{\sqrt{T_{tot}}} \sqrt{\sum_{n=1}^{N_{echo}} 4\gamma^2 SNR_n^2[(T_{ES} - \tau_\pi)n - 0.5\tau_{\pi/2}]^2} \quad [5]$$

In order to further relate the efficiency stated in Equation [5] to the sequence and tissue relaxation parameters, the 1D case is considered. The continuous complex transverse magnetization $\mu(x, t)$ depends on T_1, T_2, T_2^* relaxations and a signal loss factor caused by imperfect refocusing. Defining β_{RF} to be the fraction of preserved signal after each refocusing pulse, and under an assumption of a Lorentzian spectral density distribution (Eq. [6]),

$$\mu^n(x,t) = \mu_0(x)[1 - e^{-T_{rec}/T_1(x)}]e^{-nT_{ES}/T_2(x)}e^{-|t-nT_{ES}|/T_2^*(x)}\beta_{RF}^n \quad \text{for } (n-0.5)T_{ES} < t < (n+0.5)T_{ES} \quad [6]$$

$\mu_0(x)$ is the equilibrium magnetization distribution and T_{rec} is the T_1 recovery period between nulling of longitudinal magnetization after the last refocusing pulse and re-excitation of the same slice (the factor β_{RF}^n expresses the accumulated effect of imperfect refocusing pulses in later echoes). The acquired signal $S(k_x, t)$ for the nth MESE echo can then be expressed as Equation [7]:

$$S^n(k_x, t) = \int_{\text{object}} \mu^n(x,t)e^{-j2\pi k_x x}dx \quad [7]$$

The object can conceptually be considered a distribution of point sources. Combining Equations [6] and [7] and assuming an idealized single point distribution ($\mu_0(x) = \delta(x)$), constant relaxation times, β_{RF}, and noise σ, and a standard k-space trajectory $k_x(t) = \frac{\gamma G_x}{2\pi}(t - nT_{ES})$ results in the conclusion that the SNR_n in Equation [5] is proportional to attenuation factors ($\alpha_{T_1}, \alpha_{T_2}, \alpha_{T_2^*}$ and α_{RF}) caused by the T_1, T_2, T_2^* relaxations and RF imperfections, which can be expressed as Equation [8]:

$$SNR_n = \frac{|M_n|}{\sigma} \propto \alpha_{T_1}\alpha_{T_2}\alpha_{T_2^*}\alpha_{RF}$$

$$\alpha_{T_1} = 1 - e^{-T_{rec}/T_1}, \quad \alpha_{T_2} = e^{-nT_{ES}/T_2}, \quad \alpha_{RF} = \beta_{RF}^n$$

$$\alpha_{T_2^*} = \frac{1}{N_x\Delta k_x}\int_{-N_x\Delta k_x/2}^{N_x\Delta k_x/2} e^{-2\pi|k_x|/\gamma G_x T_2^*}dk_x = \frac{2T_2^*(1 - e^{-T_s/2T_2^*})}{T_s} \quad [8]$$

$|M_n|$ is the noise-free reconstructed MR magnitude image, which is proportional to μ^n given in Equation [6]. G_x is the readout gradient strength, N_x the readout matrix size, T_s the readout period, and Δk_x the spatial frequency resolution. The recovery of the longitudinal magnetization is almost linear for $T_{ES} << T_1$ within the period between refocusing pulses. Therefore, it can be assumed that the longitudinal magnetization is nulled at each echo, and T_{rec} can be approximated as shown by Equation [9]:

$$T_{rec} \approx (N_{slice} - 1)N_{echo}T_{ES} + N_{slice}T_D \quad [9]$$

N_{slice} and T_D are number of slices and dead time, respectively. In combination, Equations [5], [8], and [9] characterize the dependency of the efficiency of a MESE MREIT experiment on the sequence and tissue parameters.

SSFP-FID MREIT

Lee et al have previously studied different SSFP variants for MREIT (19). Here, we investigate their most sensitive variant further, in which the current is applied before the readout period (SSFP-FID_{PCI} with partial current injection; Fig. 1b). In addition, we propose a novel variant in which the current is injected within the entire T_R period (SSFP-FID_{FCI} with full current injection; Fig. 1b). The analytical solutions for the steady-state magnetization immediately after excitation with bipolar current injection have been derived by Lee et al (19) (Eq. [10]):

$$\mu_{ss_1}(\ t=0^+) = \frac{\mu_0(1-E_1)\sin(\alpha)}{D}\begin{pmatrix} A_1 e^{-2j(\varphi_g+\varphi_b)} + A_2 e^{-2j\varphi_c} + A_3 e^{j(\varphi_g+\varphi_b-\varphi_c)} \\ +A_4 e^{-j(\varphi_g+\varphi_b-\varphi_c)} + A_5 e^{-j(\varphi_g+\varphi_b+\varphi_c)} + A_6 \end{pmatrix}$$

$$\mu_{ss_2}(\ t=0^+) = \frac{\mu_0(1-E_1)\sin(\alpha)}{D}\begin{pmatrix} A_1 e^{-2j(\varphi_g+\varphi_b)} + A_2 e^{2j\varphi_c} + A_3 e^{j(\varphi_g+\varphi_b+\varphi_c)} \\ +A_4 e^{-j(\varphi_g+\varphi_b+\varphi_c)} + A_5 e^{-j(\varphi_g+\varphi_b-\varphi_c)} + A_6 \end{pmatrix}$$

with

$$A_1 = {E_2}^2(1+E_1)\Big(1+\cos(\alpha)\Big), A_2 = {E_2}^2(1-E_1)\Big(1-\cos(\alpha)\Big)$$

$$A_3 = -E_2(1+E_1)\Big(1+\cos(\alpha)\Big), A_4 = E_2(1-E_1)\Big(1-\cos(\alpha)\Big) \qquad [10]$$

$$A_5 = 2{E_2}^3\Big(E_1+\cos(\alpha)\Big), A_6 = -2\Big(1+E_1\cos(\alpha)\Big)$$

$$D = {E_2}^2(1-{E_1}^2)[\Big(\cos(\alpha)+1\Big)^2\cos\Big(2(\varphi_g+\varphi_b)\Big) + \Big(\cos(\alpha)-1\Big)^2\cos(2\varphi_c)]+$$

$$2E_1E_2(1-{E_2}^2)\Big(\cos(2\alpha)-1\Big)\cos(\varphi_g+\varphi_b)\cos(\varphi_c)+$$

$$2\Big(E_1\cos(\alpha)+1\Big)\Big(E_1\cos(\alpha)-1\Big) + 2{E_2}^4\Big(E_1+\cos(\alpha)\Big)\Big(E_1-\cos(\alpha)\Big)$$

and

$$E_1 = e^{-T_R/T_1}, E_2 = e^{-T_R/T_2}$$

Here, μ_{ss1} and μ_{ss2} are the alternating first and second steady-state transversal magnetizations; μ_0 is the thermal equilibrium magnetization, α the tip angle, φ_g the gradient-induced phase, φ_b the B_0 inhomogeneity-induced phase, and φ_c the current-induced phase. The steady-state magnetization at T_E becomes (Eq. [11]):

$$\mu_{SS_1}^{FID_1}(\Delta B_{z,c}, t=T_E) = \mu_{ss_1}(\varphi_c=\gamma\Delta B_{z,c}T_c,\ t=0^+)e^{-T_E/T_2}e^{j\gamma(\Delta B_0+\Delta B_{z,c})T_E}$$

$$\mu_{SS_2}^{FID_1}(\Delta B_{z,c}, t=T_E) = \mu_{ss_2}(\varphi_c=\gamma\Delta B_{z,c}T_c,\ t=0^+)e^{-T_E/T_2}e^{j\gamma(\Delta B_0-\Delta B_{z,c})T_E}$$

$$\mu_{SS_1}^{FID_2}(\Delta B_{z,c}, t=T_E) = \mu_{ss_1}(\varphi_c=\gamma\Delta B_{z,c}T_R, t=0^+)e^{-T_E/T_2}e^{j\gamma(\Delta B_0+\Delta B_{z,c})T_E}$$

$$\mu_{SS_2}^{FID_2}(\Delta B_{z,c}, t=T_E) = \mu_{ss_2}(\varphi_c=\gamma\Delta B_{z,c}T_R, t=0^+)e^{-T_E/T_2}e^{j\gamma(\Delta B_0-\Delta B_{z,c})T_E} \qquad [11]$$

where T_c is the injected current pulse width and ΔB_0 the local B_0 inhomogeneity. Assuming sufficiently strong spoiler gradients creating a uniform intravoxel phase distribution at the end of each repetition, the SSFP-FID signal is equal to the integral of the steady-state magnetization with respect to φ_g over a 2π interval (19,23). Therefore, constant phase shifts attributed to RF phase imperfections or local B_0 inhomogeneity do not influence the steady-state signal.

In contrast to MESE, SSFP-FID has a nonlinear dependence of $\Delta B_{z,c}$ on the phase of the transverse magnetization. However, for weak currents, this can be well approximated by a linear relationship (Eq. [12]):

$$\Delta B_{z,c} = \frac{\angle M_{SS1} - \angle M_{SS2}}{m_{seq}} \qquad [12]$$

where $\angle M_{SS1}$ and $\angle M_{SS2}$ are the phases of the first and second steady-state complex MR images and $m_{seq}=\partial(\angle M_{SS1}-\angle M_{SS2})/\ \partial\Delta B_{z,c}$ express the field dependence on the phase change. The standard deviation of the $\Delta B_{z,c}$ estimate and the efficiency can then be calculated as Equation [13]:

$$\sigma_{\Delta B_{z,c}} = \frac{1}{m_{seq}SNR},$$
$$\eta_{SSFP\text{-}FID} = \frac{|\angle M_{SS1} - \angle M_{SS2}|}{\sqrt{T_{tot}}}SNR \qquad [13]$$

with SNR being the SNR of the magnitude image.

METHODS

In this section, the numerical simulation methods are introduced, which were used to systematically evaluate the efficiencies of MESE and SSFP-FID MREIT based on the above theory. This is followed by a description of the experimental methods used to validate the theory and simulations.

Simulations

The efficiency of MESE was simulated based on Equations [5], [8], and [9]. Relaxation times of $T_1 = 1.1$ seconds, $T_2 = 100$ ms, and $T_2^* = 50$ ms were used, similar to those of brain tissue (24). The RF pulse durations and their efficiency were set to $\tau_{\pi/2} = 2.048$ ms, $\tau_\pi = 2.56$ ms, and $\beta_{RF} = 0.86$ to match those of the clinical 3T scanner used in the MESE experiments (the MESE section also describes the measurement of β_{RF}). The longest crusher gradient duration was set to $T_{crush} = 7.5$ ms, and this value was determining the minimal echo spacing in the simulations. Because the SNR of an MR image scales with the square root of data acquisition time (21), the lowest possible sampling bandwidths (BWs) were chosen in all simulations.

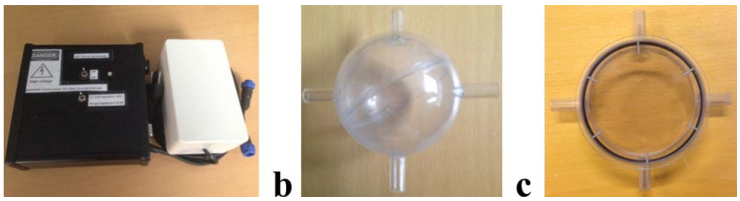

FIG. 2. (**a**) Photograph of the current source. (b) Phantom 1 was spherical with a diameter of 10 cm, filled with saline (1.45 g/L of NaCl) and doped with 0.1 mM of $MnCl_2$ to reach relaxation times of $T_1 = 1.1$ s and $T_2 = 100$ ms (31). T_1 values were determined by repeating an inversion recovery gradient recalled echo (IR-GRE) sequence for different inversion times. T_2 values were measured by repeating a spin echo sequence for a range of echo times. Also, the tip angle variation over the imaging region was investigated using a double-angle method (32). The tip angle map was created by repeating an RF spoiled fast low angle shot sequence with two different tip angles ($\alpha = 30^\circ$ and $\alpha = 60^\circ$; $T_E = 5$ ms; $T_R = 5$ seconds). The tip angle deviation over the imaging region was around 10%. (**c**) Phantom 2 was cylindrical with 10 cm in diameter and 3 cm in height, filled with the same saline solution and with a piece of organic chicken meat placed in its center. The relaxation parameters in Phantom 2 were around $T_1 = 1.05$ seconds, $T_2 = 110$ ms in the saline region, and $T_1 = 1.1$ seconds, $T_2 = 50$ ms in the chicken meat.

- For a single-slice acquisition, the SNR and efficiency of $\Delta B_{z,c}$ were simulated for a fixed dead time $T_D = 510$ ms to demonstrate the effects of N_{echo} and T_{ES}. The simulations were performed for $T_{ES} = [20–160]$ ms and $N_{echo} = [1–8]$.
- For multi-slice acquisitions, the dependence of the efficiency on T_D was obtained for different numbers of slices $N_{slice} = [1–5, 15]$, whereas the T_{ES} and N_{echo} giving the highest efficiency were selected for each T_D. The simulations were performed for $T_D = [0.1–10]$ s, $T_{ES} = [20–200]$ ms, and $N_{echo} = [1–8]$ (even for $T_{ES} = 200$ ms, the assumption of a linear recovery of the longitudinal magnetization causes an error of less than 9% when reading out the optimal T_D).

The SSFP-FID simulations were performed by using 3D rotation and relaxation matrices (25) and were cross-checked by the analytically derived Equations [10] to [13]. The number of isochromates in the simulations was 100, instantaneous RF pulses were assumed, and the spoiler gradients were modeled as creating 4π intravoxel phase dispersion. Relaxation times of $T_1 = 1.1$ s, $T_2 = 100$ ms, and $T_2^* = 50$ ms were used.

- First, the dependence of the steady-state transverse magnetization magnitude and phase on $\Delta B_{z,c}$ were simulated for both SSFP-FID variants and compared with spin echo. The simulation parameters were $\alpha = 60^\circ$, TR = 20 ms, TE = 10 ms, and a range of $\Delta B_{z,c} = [-100$ to $100]$ nT was covered.
- For the more efficient variant $SSFP\text{-}FID_{FCI}$, SNR and efficiency of $\Delta B_{z,c}$ measurements were simulated in order to demonstrate the effect of T_R and T_E. The simulation parameters were $\alpha = 20^\circ$, $\Delta B_{z,c} = 1$ nT, $T_R = [20–260]$ ms, and $T_E = [10–140]$ ms. The RF pulse width, prephaser, and spoiler gradient durations were set to $\tau_\alpha = 2$ ms, $T_{pre} = 0.5$ ms, and $T_{sp} = 0.6$ ms, respectively. Impossible combinations of T_E and T_R (i.e., $T_E > T_R$) were ignored. The image SNR was adjusted according to a choice of lowest possible sampling BWs.
- To find the most efficient parameters settings for $SSFP\text{-}FID_{FCI}$, the effect of the tip angle on the efficiency was also investigated. The simulation parameters were $\alpha = [5^\circ–90^\circ]$, $T_E = [10–120]$ ms, and $T_R = [20–1500]$ ms. For each tip angle, the normalized maximal efficiency and the corresponding T_E and T_R were selected and the results plotted with respect to α.

As a last step, we explored via simulations the loss in efficiency when using multi-gradient-echo summation by means of multiple monopolar or bipolar readout gradients to prevent image distortions resulting from using low BWs at long T_{ES} (MESE) or T_R (SSFP-FID). The number of summed echoes during a readout period N_m was varied in the range [1–16]. For MESE, $T_{ES} = 80$ ms was selected and the duration of the added prephaser gradients was $T_{pre} = 0.5$ ms. The other parameters were kept unchanged from the prior simulations. For SSFP-FID, $T_R = 160$ ms was used.

Experiments

All experiments were performed on a 3T MRI scanner (MAGNETOM Prisma; Siemens Healthcare, Erlangen, Germany) equipped with a 64-channel head coil (an adaptive combine algorithm (26) was used to combine the received MRI signals from each coil element). The current waveforms were created by an arbitrary waveform generator (33500B; Keysight Technologies, Santa Clara, CA, USA) and a home-made voltage-to-current converter (Fig. 2a), and injected into a phantom by recessed copper electrodes (Fig. 2b,c). Two different phantoms were used: Phantom 1 was spherical and filled with doped saline having relaxation times similar to brain tissue (Fig. 2b). Phantom 2 was cylindrical, filled with similar doped saline and having a piece of organic chicken meat placed in its center (Fig. 2c).

For MESE, the following experiments were performed:

- The importance of properly designed crusher gradients to prevent the impact of nonideal RF refocusing pulses on the phase evolution was demonstrated in Phantom 1. Three different MESE pulse sequences were tested and their current-induced phase evolutions over echoes were compared. In the first two sequences, the momentum of the crusher gradients

were kept constant and refocusing RF pulses of 150° and 180° were used to explore effects of B_1 inhomogeneity. In the third sequence, the momentum of the crusher gradients was systematically changed and 180° refocusing RF pulses were used: The crusher momentums were either doubled between subsequent echoes or the crusher gradient direction was switched. In all sequences, the first crusher gradient was optimized for creating a 4π intravoxel phase dispersion (27). The other sequence parameters were: field of view (FOV) = $200 \times 200\,mm^2$, image matrix = 128×128, slice thickness $\Delta z = 3$ mm, $N_{avg} = 1$, $N_{echo} = 7$, injected current magnitude $I_c = 1$ mA, $T_{ES} = [40, 60]$ ms, and $T_D = 510$ ms.

- Efficiency measurements were performed in Phantom 1. The measurement parameters were FOV = $300 \times 300\,mm^2$, image matrix = 256×256, $\Delta z = 5$ mm, $T_D = 510$ ms, $N_{avg} = 1$, $N_{echo} = [1–8]$, and $I_c = 0.5$ mA. The measurements were repeated by varying the echo spacing $T_{ES} = [20–160]$ ms with 20-ms intervals. In each experiment, the lowest possible bandwidth (BW) was used. The experiments were repeated with opposite polarity bipolar current injection in order to eliminate systematic phase artifacts and to increase the SNR of the experiment (21). The phase evolution over echoes, combined $\Delta B_{z,c}$ across echoes, SNR of the combined $\Delta B_{z,c}$, and efficiency were determined from the measurements (the root-mean-square SNR of the combined $\Delta B_{z,c}$ and the efficiency values were calculated in the region of interest ROI shown in Figs. 4a and 7a). To estimate the preserved signal ratio β_{RF} influenced by RF inhomogeneity, the signal decay across multiple echoes for $T_{ES} = 20$ ms was compared with the real T_2 decay determined from the first echoes when varying T_{ES} from 20 ms to 160 ms.

For SSFP-FID, the following experiments were performed:

- SSFP-FID measurements were repeated for different current magnitudes to validate the simulated dependency on $\Delta B_{z,c}$ of the transverse magnetization phase. The measurements were performed with both SSFP-FID_{PCI} and SSFP-FID_{FCI} sequences in Phantom 1 and their phase sensitivities were compared. The sequence parameters were FOV = $375 \times 375\,mm^2$, image matrix = 256×256, $\Delta z = 3$ mm, $\alpha = 60°$, $N_{avg} = 16 \times 2$ (16 separate averages for each steady state). The experiments were repeated for three different repetition times $T_R = [10, 30, 50]$ ms (with $T_E = T_R/2$) and for different current magnitudes $I_c = [–10$ to $10]$ mA with 2-mA intervals. The lowest possible BW was always selected to maximize SNR.
- Efficiency measurements were performed in Phantom 1 for SSFP-FID_{FCI}. The measurement parameters were FOV = $192 \times 192\,mm^2$, image matrix = 128×128, $\Delta z = 3$ mm, $\alpha = 20°$, $N_{avg} = 2 \times 2$, and $I_c = 1$ mA. The experiment was repeated for different echo times $T_E = [10–140]$ ms with 10-ms intervals and repetition times $T_R = [20–260]$ ms with 20-ms intervals. Impossible combinations of T_E and T_R (i.e., $T_E > T_R$) were ignored. In each measurement, bipolar currents were injected to create dual steady states with opposite current-induced phases. From these steady-state data, phase difference images were calculated and $\Delta B_{z,c}$ was reconstructed by using $m_{seq} = \partial(\angle M_{SS1} - \angle M_{SS2})/\partial \Delta B_{z,c}$ in the simulations. The SNR of the $\Delta B_{z,c}$ images and the efficiency were then determined.

In addition, two experiments with the optimized MESE and SSFP-FID_{FCI} sequences were performed in Phantom 1 in order to directly compare their efficiencies. The sequence parameters were FOV = $256 \times 256\,mm^2$, image matrix = 128×128, $N_{avg} = 1 \times 2$, and $I_c = 1$ mA. The optimized parameters were selected as $T_{ES} = 80$ ms, $T_D = 1.5$ s, and $N_{echo} = 3$ for MESE; and $T_E = 60$ ms, $T_R = 120$ ms, and $\alpha = 30°$ for SSFP-FID_{FCI}.

Finally, the MESE and SSFP-FID_{FCI} experiments were performed in Phantom 2 to demonstrate the sequence performance for a nonhomogenous geometry involving a chicken meat piece. The experiments were performed for both vertical and horizontal electrical current injection. The MESE measurement parameters were $T_{ES} = 80$ ms, $T_D = 510$ ms, $N_{echo} = 3$, FOV = $192 \times 192\,mm^2$, image matrix = 128×128, $\Delta z = 3$ mm, BW = 100 Hz/pixel, $N_{avg} = 1$, and $I_c = 1$ mA. The SSFP-FID_{FCI} measurement parameters were $\alpha = 20°$, $T_E = 15$ ms, $T_R = 30$ ms, FOV = $192 \times 192\,mm^2$, image matrix = 128×128, $\Delta z = 3$ mm, BW = 100 Hz/pixel, $N_{avg} = 16 \times 2$, and $I_c = 1$ mA.

RESULTS

MESE

As a first step, the importance of properly chosen crusher gradients is demonstrated. When keeping the crusher gradients constant, the stimulated echo pathways caused by the nonideal refocusing pulses have a clear impact on the phase evolution (Fig. 3a,b). This effect is more prominent for 150° refocusing pulses (Fig. 3a), but is also clearly visible in the later echoes for 180° refocusing pulses (Fig. 3b). In contrast, systematically doubling the area of the crusher gradients between consecutive echoes in combination with changing crusher direction (27) successfully eliminates the unwanted echo pathways, resulting in the expected linear phase increase over echoes (Fig. 3c).

The results of the efficiency simulations and measurements for a fixed T_D are shown in Figure 4. As an example, Figure 4a shows the combined $\Delta B_{z,c}$ image for eight echoes ($T_{ES} = 20$ ms, $T_R = 670$ ms, BW = 125 Hz/pixel, and $I_c = 0.5$ mA). The measured $\Delta B_{z,c}$ pattern is in agreement with the current flowing from top to bottom. As expected, the weak current strength did not cause significant geometric distortions despite being applied throughout the readout periods. Figure 4b shows the measured phase evolution across echoes for $T_{ES} = [20–160]$ ms, confirming the linear phase evolution for the optimized crusher gradients. The simulated and measured dependencies of the efficiency of the combined $\Delta B_{z,c}$ on N_{echo} and T_{ES} are shown in Figure 4e,f. Because the simulations give only relative efficiency values, both plots are normalized to their individual maxima. The

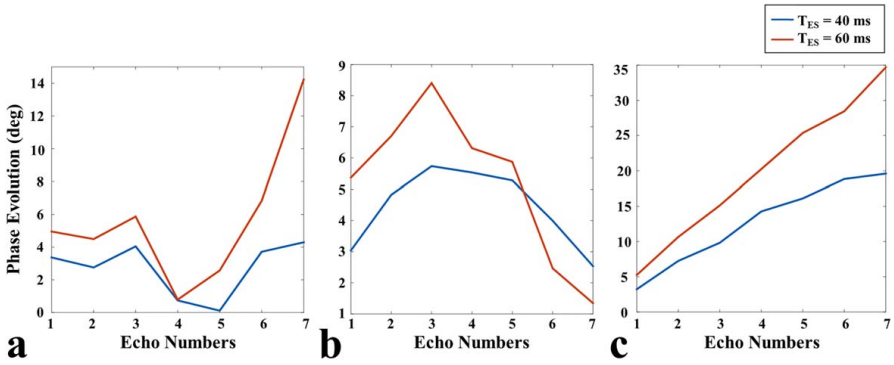

FIG. 3. Phase evolution for MESE across echoes, tested for two different echo spacings $T_{ES} = [40, 60]$ ms. (**a**) The refocusing pulse tip angle is 150°, and the gradient areas and axes are kept identical across echoes. This results in both primary and stimulated echo pathways. (**b**) The refocusing pulse tip angle is 180°, and the gradients are kept identical. This also causes primary and stimulated echo pathways. (**c**) The refocusing pulse tip angle is 180° and the gradients are systematically varied, resulting in the selection of only the primary echo pathway and a linear phase accumulation.

simulations and experimental results are in good agreement. The corresponding results for the SNR are shown in Supporting Figure S1. While the SNR increases with the number of acquired echoes, the highest efficiency occurs for $N_{echo} = [2, 3]$. This indicates that the later echoes contribute only weakly to the combined $\Delta B_{z,c}$ image. Interestingly, the highest efficiency is found for rather long echo times of $T_{ES} = [80–100]$ ms. In order to make a comparison with our results and the literature, single-echo SE with $T_E = 60$ ms is selected as a reference (12,21). The selection of the most efficient sequence parameters results in an efficiency increase of 41%.

So far, the efficiency was only assessed for a single slice and a fixed T_D value. Figure 5a shows the simulated efficiency also with respect to T_D and different number of slices, normalized to the maximum across all simulations. For each T_D, the most efficient T_{ES} and N_{echo} were selected. In addition, the corresponding T_{ES} and N_{echo} for a single slice are shown in Figure 5b. For a single slice, the efficiency peaks for a rather long T_D of around 1.5 seconds, indicating that a substantial recovery of the longitudinal magnetization before re-excitation is optimal. Interestingly, the maximal efficiency can still be reached for three to four slices (as expected, T_D reaches 0 in this case) and a clear drop occurs only for a higher number of slices. This shows that multi-slice MESE MREIT is feasible without losing efficiency. The optimized T_{ES} is around 80 ms and the best-performing N_{echo} increases from 2 to 4 when increasing T_D.

SSFP-FID

Simulated dependencies of the transverse magnetization phase on $\Delta B_{z,c}$ are shown in Figure 6a for both sequence variants. The results indicate that the dependency of the steady-state phase on $\Delta B_{z,c}$ can be well linearized for weak injection currents. Judging from the slope of the phase dependencies around 0, SSFP-FID_{PCI} is 37% and SSFP-FID_{FCI} is 73% more sensitive compared to the standard spin echo case. Measured dependencies of the steady-state phase on the injected current strength I_c are shown in Figure 6b (SSFP-FID_{PCI}) and 6c (SSFP-FID_{FCI}). The measured steady-state phase depends linearly on $\Delta B_{z,c}$ for both variants. SSFP-FID_{FCI} is 26% more sensitive than SSFP-FID_{PCI} for $T_R = 50$ ms. This is in good agreement with the simulations (Fig. 6a), using the linear relationship between $\Delta B_{z,c}$ and I_c. In contrast to the phase, the steady-state magnitude has a flat dependency on $\Delta B_{z,c}$ for both variants for the weak injected current strengths tested here ($\Delta B_{z,c}$ close to 0), both in the simulations (Supporting Fig. S2a) and measurements (Supporting Fig. S2b,c).

The results of the efficiency simulations and measurements for SSFP-FID_{FCI} are shown in Figure 7. Figure 7a shows the reconstructed $\Delta B_{z,c}$ image from the averaged phase difference images between the two alternating steady states for $\alpha = 20°$, $T_R = 20$ ms, $T_E = 10$ ms, and $I_c = 1$ mA. The image is in agreement with the current flowing from top to bottom, and, as expected, the weak current strength did not cause geometric distortions despite being applied throughout the readout periods. However, significant signal drop attributed to T_2^* decay is observed in the poorly shimmed regions, such as near the electrodes and phantom edges. Figure 7b shows the measured phase evolution for $T_E = [10–140]$ ms and $T_R = [20–260]$ ms. The steady-state phase increases linearly with increasing T_E. There is no significant phase change observed for different T_R values when T_E is kept constant.

Figure 7c,d shows the simulation and experimental results for the efficiencies of $\Delta B_{z,c}$, normalized to their individual maxima (Supporting Fig. S3a,b depicts the corresponding SNR plots). Simulations and experimental results agree well. The maximal efficiency occurs for $T_E = [60–90]$ ms and $T_R = [120–180]$ ms. The highest efficiency is mostly observed when $T_E = T_R/2$, attributed to the symmetric data acquisition. Interestingly, the highest efficiency occurs for rather long echo times. This indicates that the increased signal strength attributed to

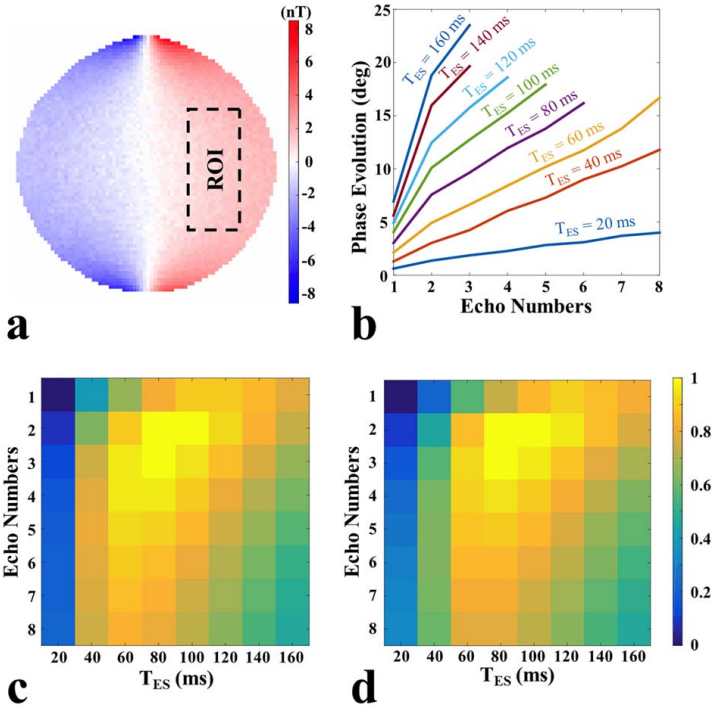

FIG. 4. MESE simulation and measurement results. (**a**) Measured combined $\Delta B_{z,c}$ image for $N_{slice} = 1$, $N_{avg} = 1$, $N_{echo} = 8$, $T_{ES} = 20$ ms, $T_D = 510$ ms, BW = 125 Hz/pixel, and $I_c = 0.5$ mA. The current is injected in a vertically downward direction. The ROI used to calculate the SNR and the efficiency is shown by the dashed lines. (**b**) Measured phase evolution over echo numbers for different T_{ES}. (**c**) Simulated efficiency. (**d**) Measured efficiency. The results in (**c**) and (**d**) are normalized relative to their maximal values. The measurement and simulation parameters in (**b–d**) are FOV = $300 \times 300\,mm^2$, image matrix = 256×256, $\Delta z = 5$ mm, $N_{slice} = 1$, $N_{avg} = 1$, $N_{echo} = [1–8]$, $T_{ES} = [20–160]$ ms, $T_D = 510$ ms, $T_1 = 1.1$ seconds, $T_2 = 100$ ms, $T_2^* = 50$ ms, and $I_c = 0.5$ mA. In both measurements and simulations, the lowest possible BW is selected to maximize the SNR of the MR magnitude image.

increased T_1 recovery and higher phase accumulation outweighs the stronger impact of T_2^* decay at longer T_E.

So far, the results were assessed for a fixed tip angle α of 20°. Figure 8 shows the simulated efficiency also with respect to changes in the tip angle for SSFP-FID_{FCI}, normalized to the maximum across all simulations. The most efficient T_E and T_R values were selected for each tip angle. The maximal efficiency occurs around $\alpha = 30°$ and decreases slightly for higher tip angles (Fig. 8a). The corresponding optimized T_E and T_R values are shown in Figure 8b,c. The optimized echo time T_E varies in the range between 50 and 80 ms (i.e., it is roughly in the

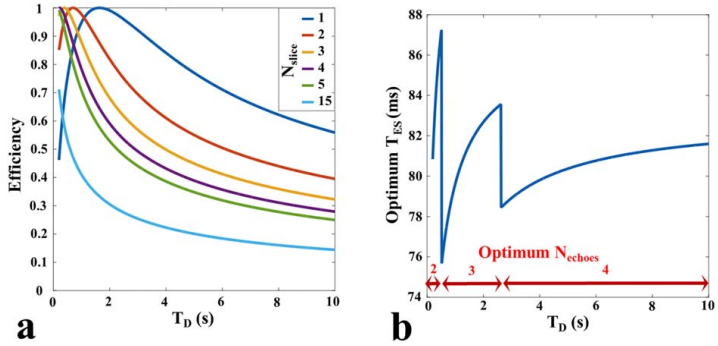

FIG. 5. (**a**) Efficiency of MESE with respect to T_D, assessed for slices $N_{slice} = [1–5, 15]$ and normalized to the peak across all simulations. For each T_D, T_{ES}, BW, and N_{echo} were optimized. (**b**) Corresponding echo spacing T_{ES} and number of echoes N_{echo} for $N_{slice} = 1$.

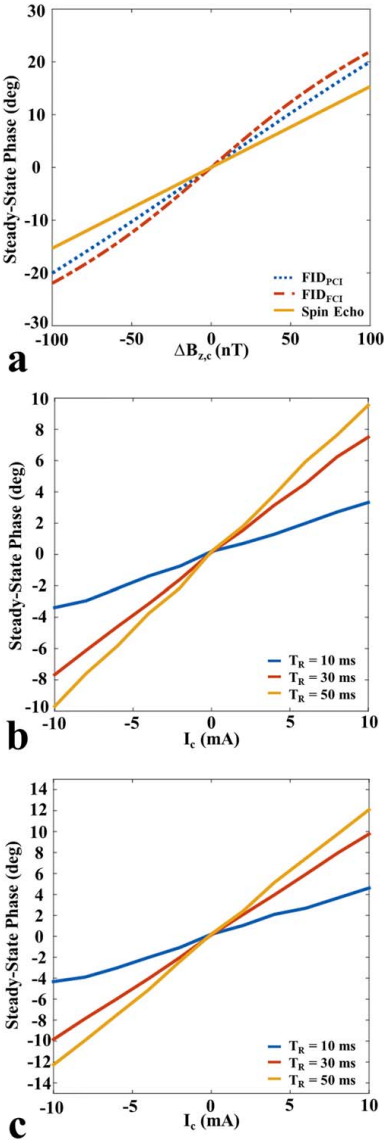

FIG. 6. (**a**) Simulated dependency of phase of the steady-state transverse magnetization. (**b**) SSFP-FID_{PCI}. Measured dependencies of the phase of the transverse magnetization. (**c**) SSFP-FID_{FCI}. Measured dependencies of the phase of the transverse magnetization. (**b,c**) The results were obtained for $T_R = [10, 30, 50]$ ms and $I_c = [-10 \text{ to } 10]$ mA.

range of the selected T_2^*) and reaches a plateau for higher tip angles. This is mainly attributed to the large signal loss for sampling times much longer than T_2^*. The optimized T_R increases with tip angle.

Comparison Between MESE and SSFP-FID

The efficiencies of MESE and SSFP-FID_{FCI} with optimized sequence parameters were directly compared. SSFP-FID_{FCI} has a 0.07% higher SNR for $\Delta B_{z,c}$ compared to MESE, but gives a 3 times higher efficiency. This suggests that SSFP-FID may be very useful for rapid imaging. However, the SSFP-FID causes a significant efficiency decrease in inhomogenous regions and the image is significantly distorted, whereas MESE can preserve both. In addition, multi-slice SSFP-FID applications will cause significant efficiency decrease, whereas MESE preserves the efficiency.

Maximal Efficiency for Multi-Gradient-Echo Acquisition

The most efficient parameter ranges in both MESE and SSFP-FID experiments result in very low BWs, which cause geometric image distortions attributed to B_0 inhomogeneities. This effect can be prevented by acquiring multiple gradient echoes during each readout period at a higher BW, which are then added (17). Here, the efficiency decrease attributed to the time required for the additional prephaser gradients and gradient switching and corresponding BW were simulated. For both monopolar (Fig. 9a) and bipolar readout gradients (Fig. 9b), only a moderate loss of efficiency of less than 10% occurred for up to 16 gradient echoes. This indicates that the summation of multiple gradient echoes may be a suitable way for preventing geometric distortions caused by otherwise low BWs while maintaining acquisition efficiency.

Experiments in a Phantom With Inhomogeneous Geometry

MESE and SSFP-FID_{FCI} images were obtained in Phantom 2 containing a piece of chicken meat to assess the sequence performance for nonuniform structures. The sequence parameters were chosen in pilot trials to optimize efficiency as far as possible while maintaining image quality at an acceptable level. The results are reported for vertical and horizontal directions of current injection. For MESE, the combined MR magnitude image is shown in Figure 10a, and the combined $\Delta B_{z,c}$ images for horizontal and vertical current injection are depicted in Figure 10b,c. For SSFP-FID_{FCI}, the averaged MR magnitude image is shown in Figure 10d, and the $\Delta B_{z,c}$ images are given in Figure 10e,f. Both sequences allow accurate $\Delta B_{z,c}$ measurements for the saline regions of the phantom, despite using a low current magnitude of $I_c = 1$ mA. The impact of the chicken piece on the $\Delta B_{z,c}$ distribution is clearly visible in particular for the horizontal current injection. In MESE, the SNR of combined $\Delta B_{z,c}$ image is lower in the region of the chicken meat, which can be explained by the chosen T_{ES} (80 ms), which exceeds T_2 in this region (50 ms) and results in a low signal magnitude (Fig. 10a). This is less of an issue for SSFP-FID_{FCI}, where a short T_E (15 ms) was chosen.

DISCUSSION AND CONCLUSIONS

Successful in-vivo applications of MRCDI and MREIT will require that magnetic fields created by weak injection

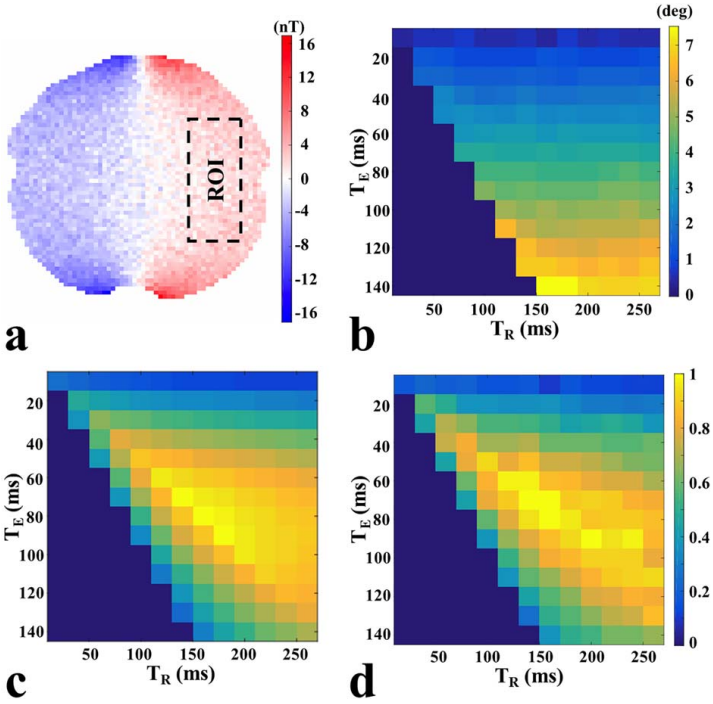

FIG. 7. Simulations and measurement results for SSFP-FID$_{FCI}$. (**a**) Measured $\Delta B_{z,c}$ image for $I_c = 1$ mA, $\alpha = 20^\circ$, $T_R = 20$ ms, and $T_E = 10$ ms. The ROI used to calculate the SNR and the efficiency is shown by the dashed lines. (**b**) Measured phase evolution. (**c**) Simulated efficiency (normalized to the maximum) of the reconstructed $\Delta B_{z,c}$ image. (**d**) Measured efficiency (normalized to the maximum) of the reconstructed $\Delta B_{z,c}$ image. The measurement and simulation parameters in (**b–d**) are $N_{avg} = 2 \times 2$ (two separate averages for each steady state), $T_E = [10–140]$ ms, $T_R = [20–260]$ ms, $T_1 = 1.1$ seconds, $T_2 = 100$ ms, $T_2^* = 50$ ms, voxel size $= 1.5 \times 1.5 \times 3\,mm^3$, image matrix $= 256 \times 256$, and $I_c = 1$ mA. In both measurements and simulations, readout was symmetrical around T_E and the lowest possible BW is selected to maximize SNR of the MR magnitude image. For impossible combinations of T_E and T_R (i.e., $T_E > T_R$), the SNR and efficiency were set to 0.

currents of 1 to 2 mA are reliably measured in clinically relevant acquisition times. We therefore performed systematic sensitivity analyses to optimize the efficiency of two MREIT pulse sequences based on MESE and SSFP-FID, respectively, while assuming relaxation times similar to human brain tissue at 3T. For both sequence types, the current injection was extended into the readout periods to maximize sensitivity. Considering the low targeted current strengths, we suggest that this is feasible without causing relevant image distortions so that correction

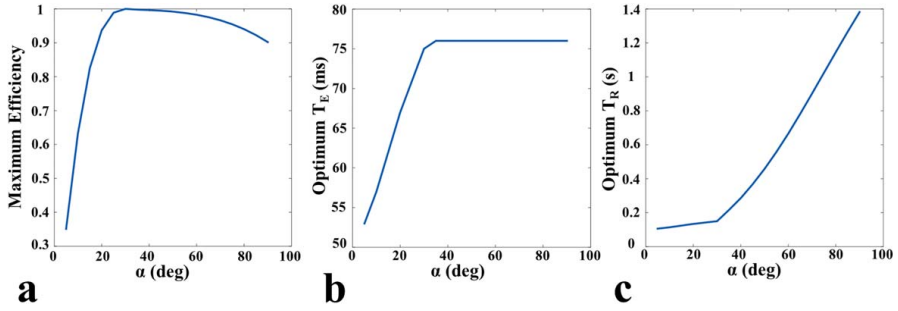

FIG. 8. Simulated efficiencies for different tip angles for SSFP-FID$_{FCI}$. (**a**) Normalized maximal efficiency dependence on the tip angle. (**b**) Corresponding optimal T_E values. (**c**) Corresponding optimal T_R values.

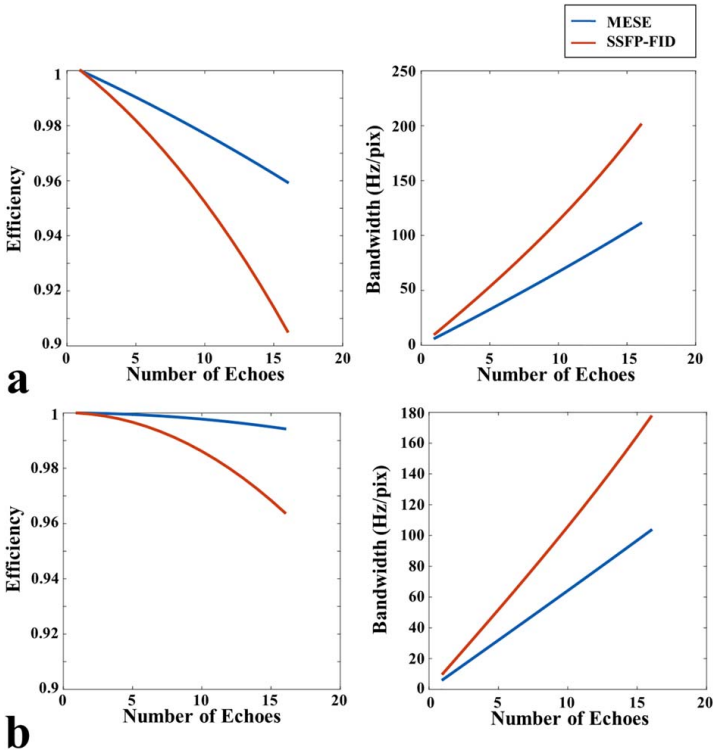

FIG. 9. Efficiency loss and corresponding BW increase in case of multi-echo acquisition: (**a**) monopolar readout gradient and (**b**) bipolar readout gradient.

strategies (28) are not needed (the distortions depend on the ratio between current-induced magnetic field and the readout gradient magnitude). In line with this, our simulations and measurements indicate that the steady-state magnitude response is only insignificantly affected by weak $\Delta B_{z,c}$, and there was no observable distortions in the magnitude images.

For MESE, the highest efficiencies were reached at echo spacings of $T_{ES} = [80–100]$ ms when using two to three echoes and a rather long dead time of $T_D = 1.5$ s. This is interesting, because it highlights the importance of allowing for sufficient T_1 recovery to boost signal intensity and by that also the SNR and efficiency of the $\Delta B_{z,c}$ images. It further opens up the possibility to use the dead time to acquire additional slices without decreasing efficiency. The parameters giving highest efficiency depend on the chosen RF pulse width, crusher gradients duration, and the efficiency of refocusing pulses. In particular, increasing the efficiency of the refocusing pulses above the 86% achieved in our phantom experiments may result in higher efficiencies with shorter T_{ES} and more echoes. This might be feasible for some human applications attributed to a better RF field homogeneity, for example, in the upper part of the brain. It is important to note that efficiency improvements by the combination of multiple echoes depend on a proper design of the crusher gradients to allow a linear phase accumulation over echoes. The systematic arrangement of crusher gradients in this study (doubling up gradient area or changing direction) guarantees elimination of unwanted echoes, at a cost of large crusher widths. This may cause small signal loss attributed to diffusion weighting, eddy currents, or concomitant magnetic fields, which are not quantified in this study. Alternative methods, such as random crusher variation, do not guarantee the complete elimination of unwanted echoes.

Two different SSFP-FID variants were considered, with the current being injected until T_E (as originally investigated in a previous work (19)) and within the entire T_R period, respectively. Because the later variant exhibited increased phase sensitivity, it was considered further in the efficiency analyses. The maximal efficiency occurred for echo times of $T_E = [60–90]$ ms, repetition times of $T_R = [120–180]$ ms, and tip angles of $\alpha = 30°$.

Our main focus was on determining optimal parameter ranges. For this, relative, rather than absolute, efficiency values were sufficient, as obtained in the simulations. However, we also directly compared the measured absolute efficiencies between optimized MESE and SSFP-FID sequences. The results demonstrate that SSFP-FID has 3 times higher efficiency compared to MESE. The SNR of the reconstructed $\Delta B_{z,c}$ images are in a similar range, but the total scan time is substantially shorter for SSFP-FID.

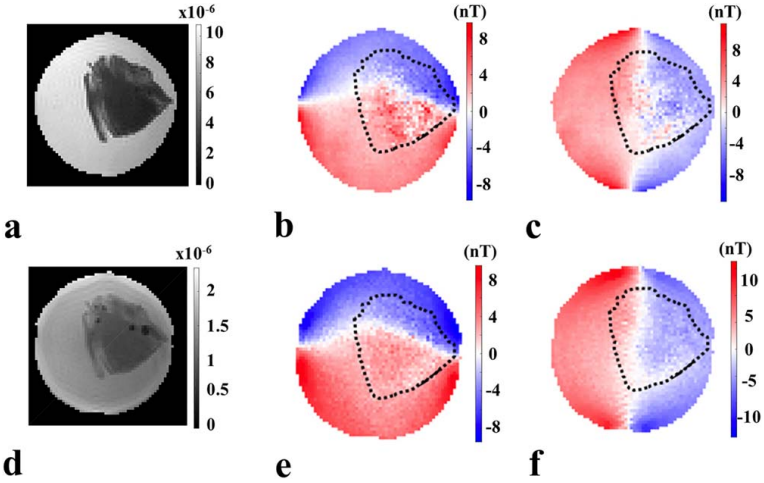

FIG. 10. Results for Phantom 2. (**a**) Combined magnitude image for MESE. (**b**) Combined $\Delta B_{z,c}$ images for MESE (horizontal current injection). (**c**) Combined $\Delta B_{z,c}$ images for MESE (vertical current injection). (**d**) Averaged magnitude image for SSFP-FID$_{FCI}$. (**e**) Reconstructed $\Delta B_{z,c}$ image for SSFP-FID$_{FCI}$ (horizontal current injection). (**f**) Reconstructed $\Delta B_{z,c}$ image for SSFP-FID$_{FCI}$ (vertical current injection). The parameters for MESE were FOV = $192 \times 192\,mm^2$, image matrix = 128×128, $\Delta z = 3$ mm, $N_{echo} = 3$, BW = 100 Hz/pixel, $N_{avg} = 1$, $T_{ES} = 80$ ms, and $T_D = 510$ ms. The parameters for SSFP-FID$_{FCI}$ were FOV = $192 \times 192\,mm^2$, image matrix = 128×128, $\Delta z = 3$ mm, BW = 100 Hz/pixel, $N_{avg} = 16 \times 2$, $\alpha = 20°$, $T_E = 15$ ms, and $T_R = 30$ ms. The injected current magnitude was $I_c = 1$ mA.

On the other hand, MESE has a better image quality, is robust to B_0 inhomogeneities, and is better suited for multi-slice experiments. Attributed to the robustness to B_0 inhomogeneities, MESE might perform better than SSFP-FID in regions with very short T_2^* (Supporting Fig. S4e,f).

Our results show that the efficiency is maximized for rather long echo spacings (for MESE) and echo times (for SSFP-FID), respectively. This also implies low readout bandwidths to optimize the SNR, resulting in considerable image distortions attributed to B_0 inhomogeneities. We suggest that this problem can be ameliorated without substantial decrease in efficiency when multiple gradient echoes are acquired at a higher BW during each readout period and are subsequently added (17). This strategy should result in a good image quality for MESE, for which the signal evolution is robust to B_0 inhomogeneities. SSFP-FID sequences are generally more susceptible to local B_0 inhomogeneities, so that the T_R (and thus also T_E), which can be achieved in practice, might be lower than the one required to maximize efficiency.

To summarize, in our phantom study, the optimized MESE and SSFP-FID sequences allowed for a reliable measurement of the magnetic field created by currents of 1 mA or below. This is promising for the exploration of these sequences for in-vivo brain imaging applications. Future sequence optimizations might use multi-gradient-echo readouts to combine high efficiencies with good image quality. Also, other sequences might further improve the efficiency, for example, balanced SSFP MREIT attributed to its very high phase sensitivity (29). Further studies are needed to evaluate the image quality in-vivo, which also depends on the sensitivity of the sequence, for example, to physiological noise and subject motion.

REFERENCES

1. Mikac U, Demsar F, Beravs K, Sersa I. Magnetic resonance imaging of alternating electric currents. Magn Reson Imaging 2001;19:845–856.
2. Eyüboğlu BM. Magnetic resonance current density imaging. In Wiley Encyclopedia of Biomedical Engineering, Vol. 4, Metin Akay, ed. Hoboken, NJ, USA: Wiley-Interscience; 2006:2147–2153.
3. Eyüboğlu BM. Magnetic resonance electrical impedance tomography. In Wiley Encyclopedia of Biomedical Engineering, Vol. 4, Metin Akay, ed. Hoboken, NJ, USA: Wiley-Interscience; 2006:2154–2162.
4. Seo JK, Woo EJ. Magnetic resonance electrical impedance tomography. Soc Ind Appl Math 2011;53:40–68.
5. Scott GC, Joy ML, Armstrong RL, Henkelman RM. Measurement of nonuniform current density by magnetic resonance. IEEE Trans Med Imaging 1991;10:362–374.
6. Woo EJ, Lee SY, Mun CW. Impedance tomography using internal current density distribution measured by nuclear magnetic resonance. SPIE 1994;2299:377–385.
7. Seo JK, Woo EJ. Electrical tissue property imaging at low frequency using MREIT. IEEE Trans Biomed Eng 2014;61:1390–1399.
8. Fear EC, Hagness SC, Meaney PM, Okoniewski M, Stuchly MA. Enhancing breast tumor detection with near-field imaging. IEEE Microw Mag 2002;3:48–56.
9. Mosher JC, Leahy RM, Lewis PS. EEG and MEG: forward solutions for inverse methods. IEEE Trans Biomed Eng 1999;46:245–259.
10. Opitz A, Paulus W, Will S, Antunes A, Thielscher A. Determinants of the electric field during transcranial direct current stimulation. Neuroimage 2015;109:140–150.
11. Thielscher A, Opitz A, Windhoff M. Impact of the gyral geometry on the electric field induced by transcranial magnetic stimulation. Neuroimage 2011;54:234–243.
12. Göksu C, Sadighi M, Eroğlu HH, Eyüboğlu M. Realization of magnetic resonance current density imaging at 3 Tesla. In: Annual International Conference of the IEEE Engineering in Medicine and Biology Society, EMBC, 2014. pp. 1115–1118.
13. Utz KS, Dimova V, Oppenländer K, Kerkhoff G. Electrified minds: transcranial direct current stimulation (tDCS) and Galvanic Vestibular

Stimulation (GVS) as methods of non-invasive brain stimulation in neuropsychology—a review of current data and future implications. Neuropsychologia 2010;48:2789–2810.
14. Minhas AS, Jeong WC, Kim YT, Han Y, Kim HJ, Woo EJ. Experimental performance evaluation of multi-echo ICNE pulse sequence in magnetic resonance electrical impedance tomography. Magn Reson Med 2011;66:957–965.
15. Sadleir R, Grant S, Zhang SU, Oh SH, Lee B Il, Woo EJ. High field MREIT: setup and tissue phantom imaging at 11 T. Physiol Meas 2006;27:S261–S270.
16. Hamamura MJ, Muftuler LT. Fast imaging for magnetic resonance electrical impedance tomography. Magn Reson Imaging 2008;26:739–745.
17. Nam HS, Kwon OI. Optimization of multiply acquired magnetic flux density B(z) using ICNE-Multiecho train in MREIT. Phys Med Biol 2010;55:2743–2759.
18. Birgül Ö, Eyüboğlu BM, Ider YZ. Magnetic resonance-conductivity imaging using 0.15 Tesla MRI scanner. In: 2001 Proceedings of the 23rd Annual EMBS International Conference, 2001. pp. 3384–3387.
19. Lee H, Jeong WC, Kim HJ, Woo EJ, Park J. Alternating steady state free precession for estimation of current-induced magnetic flux density: a feasibility study. Magn Reson Med 2016;75:2009–2019.
20. Pohmann R, von Kienlin M, Haase A. Theoretical evaluation and comparison of fast chemical shift imaging methods. J Magn Reson 1997;129:145–160.
21. Scott GC, Joy MLG, Armstrong RL, Henkelman RM. Sensitivity of magnetic-resonance current-density imaging. J Magn Reson 1992;97:235–254.
22. Sadleir R, Grant S, Zhang SU, et al. Noise analysis in magnetic resonance electrical impedance tomography at 3 and 11 T field strengths. Physiol Meas 2005;26:875–884.
23. Scheffler K, Maderwald S, Ladd ME, Bieri O. Oscillating steady states. Magn Reson Med 2006;55:598–603.
24. Wansapura JP, Holland SK, Dunn RS, Ball WS. NMR relaxation times in the human brain at 3.0 Tesla. J Magn Reson Imaging 1999;9:531–538.
25. Jaynes ET. Matrix treatment of nuclear induction. Phys Rev 1955;98:1099–1105.
26. Walsh DO, Gmitro AF, Marcellin MW. Adaptive reconstruction of phased array MR imagery. Magn. Reson. Med. 2000;43:682–690.
27. Bernstein MA, King KF, Zhou XJ (eds). Handbook of MRI Pulse Sequences. Oxford, UK: Elsevier Academic; 2004.
28. Park C, Lee B Il, Kwon O, Woo EJ. Measurement of induced magnetic flux density using injection current nonlinear encoding (ICNE) in MREIT. Physiol Meas 2007;28:117–127.
29. Bieri O, Maderwald S, Ladd ME, Scheffler K. Balanced alternating steady-state elastography. Magn Reson Med 2006;55:233–241.
30. Scheffler K. A pictorial description of steady-states in rapid magnetic resonance imaging. Concepts Magn Reson 1999;11:291–304.
31. Tofts PS. QA: quality assurance, accuracy, precision and phantoms. Quant MRI Brain 2003:55–81.
32. Insko E, Bolinger L. Mapping of the radiofrequency field. J Magn Reson 1993;103:82–85.

SUPPORTING INFORMATION

Additional supporting information can be found in the online version of this article.

Fig. S1. MESE results. (**a**) Simulated and (**b**) measured dependence of $SNR_{\Delta Bz,c}$ on the acquired number of echoes and on T_{ES}. Results are normalized relative to their maximal values. The measurement and simulation parameters are $FOV = 300 \times 300\,mm^2$, image matrix $= 256 \times 256$, $\Delta z = 5\,mm$, $N_{slice} = 1$, $N_{avg} = 1$, $N_{echo} = [1–8]$, $T_{ES} = [20–160]$ ms, $T_D = 510$ ms, $T_1 = 1.1$ s, $T_2 = 100$ ms, $T_2^* = 50$ ms, and $I_c = 0.5$ mA. In both measurements and simulations, the lowest possible BW is selected to maximize the SNR of the MR magnitude image.
Fig. S2. (**a**) Simulated dependency of the magnitude of the steady-state transverse magnetization on $\Delta B_{z,c}$ for SSFP-FID. (**b**) Measured dependencies of the magnitude of the transverse magnetization on the injected current strength for $SSFP\text{-}FID_{FCI}$. As a side note, a decrease in the signal magnitude when increasing T_E is usually expected for SSFP-FID sequences attributed to T_2^* decay. However, this is only the case when holding the BW fixed. Here, the experiments were performed for the lowest possible BW (with T_E adjusted to $T_R/2$), which caused increases in the signal magnitude up to $T_E = [60–80]$ ms. (**c**) Measured dependencies of the magnitude of the transverse magnetization for $SSFP\text{-}FID_{FCI}$. The distortion in the flat response at $T_R = 10$ ms and $I_c = 6$ mA may have been caused by hardware imperfection. The results were obtained for $T_R = [10, 30, 50]$ ms and $I_c = [–10$ to $10]$ mA.
Fig. S3. $SSFP\text{-}FID_{FCI}$ results. (**a**) Simulated and (**b**) measured dependence of $SNR_{\Delta Bz,c}$ on T_E and T_R. The measurement and simulation parameters are $N_{avg} = 2 \times 2$ (two separate averages for each steady state), $T_E = [10–140]$ ms, $T_R = [20–260]$ ms, $T_1 = 1.1$ seconds, $T_2 = 100$ ms, $T_2^* = 50$ ms, voxel size $= 1.5 \times 1.5 \times 3\,mm^3$, image matrix $= 256 \times 256$, and $I_c = 1$ mA. In both measurements and simulations, the readout is symmetrical around T_E and the lowest possible BW is selected to maximize SNR of the MR magnitude image. For impossible combinations of T_E and T_R (i.e., $T_E > T_R$), the SNR values were set to 0.
Fig. S4. Dependence of the maximal efficiency of MESE (**a,c,e**) and $SSFP\text{-}FID_{FCI}$ (**b,d,f**) on the relaxation parameters T_1, T_2, and T_2^*. The simulations were performed by varying one of the relaxation parameters while keeping the other two fixed and close to the parameters of brain tissue ($T_1 = 1.1$ seconds, $T_2 = 100$ ms, and $T_2^* = 50$ ms). The simulations are normalized to their maxima.

Sensitivity Analysis of Magnetic Field Measurements for Magnetic Resonance Electrical Impedance Tomography (MREIT)

Cihan Göksu, Klaus Scheffler, Philipp Ehses, Lars G. Hanson, and Axel Thielscher

Supplementary Material

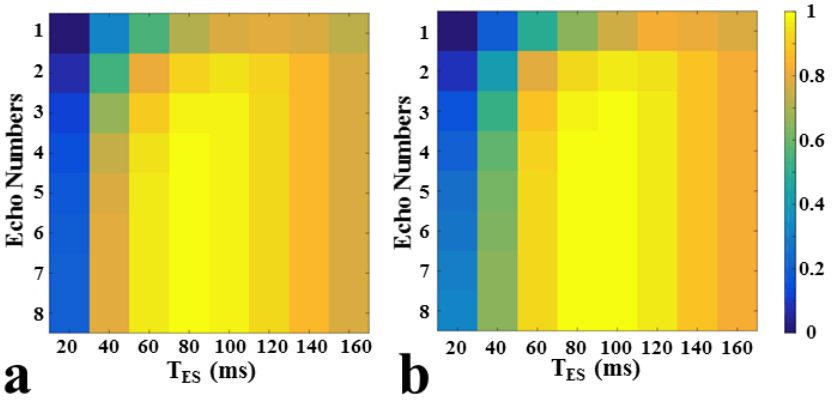

Figure S1: MESE results: (a) Simulated $SNR_{\Delta B_{z,c}}$ and (b) measured $SNR_{\Delta B_{z,c}}$ dependence on the acquired number of echoes and T_{ES}. The results are normalized by maximum value. The measurement and simulation parameters are FOV = 300x300 mm^2, image matrix = 256x256, Δz = 5 mm, N_{slice} = 1, N_{avg} = 1, N_{echo} = [1–8], T_{ES} = [20–160] ms, T_D = 510 ms, T_1 = 1.1 s, T_2 = 100 ms, T_2^* = 50 ms, and I_c = 0.5 mA. In both measurements and simulations, the lowest possible BW is selected to maximize the SNR of the MR magnitude image.

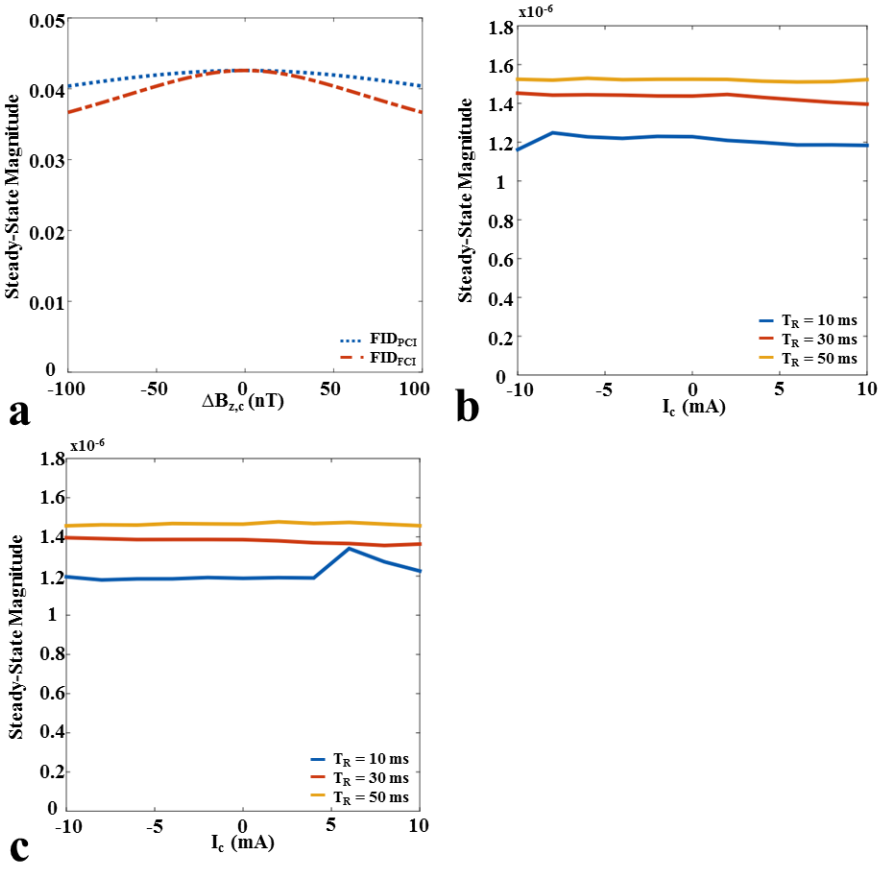

Figure S2: (a) Simulated dependency of the magnitude of the steady-state transverse magnetization on $\Delta B_{z,c}$ for SSFP-FID. (b) Measured dependencies of the magnitude of the transverse magnetization on the injected current strength for SSFP-FID_{PCI}. As a side note, a decrease in the signal magnitude when increasing T_E is usually expected for SSFP-FID sequences due to the T_2^* decay. However, this is only the case when holding the BW fixed. Here, the experiments were performed for the lowest possible BW (with T_E adjusted to $T_R/2$) which caused increases in the signal magnitude up to T_E = [60–80] ms. (c) Measured dependencies of the magnitude of the transverse magnetization for SSFP-FID_{FCI}. The distortion in the flat response at T_R = 10 ms and I_c = 6 mA may have been caused by hardware imperfection. The results were obtained for T_R = [10, 30, 50] ms and I_c = [-10–10] mA.

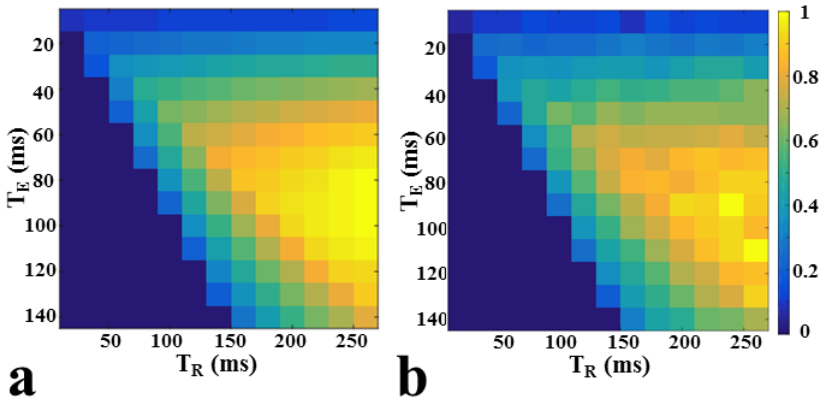

Figure S3: SSFP-FID$_{FCI}$ results: (a) Simulated SNR$_{\Delta Bz,c}$ and (b) measured SNR$_{\Delta Bz,c}$ dependence on T_E and T_R. The measurement and simulation parameters are N_{avg} = 2x2 (2 separate averages for each steady-state), T_E = [10–140] ms, T_R = [20–260] ms, T_1 = 1.1 s, T_2 = 100 ms, T_2^* = 50 ms, voxel size = 1.5x1.5x3 mm³, image matrix = 256x256, and I_c = 1 mA. In both measurements and simulations, the readout was symmetrical around T_E and the lowest possible BW is selected to maximize SNR of the MR magnitude image. For impossible combinations of T_E and T_R (i.e., T_E>T_R), the SNR and efficiency were set to 0.

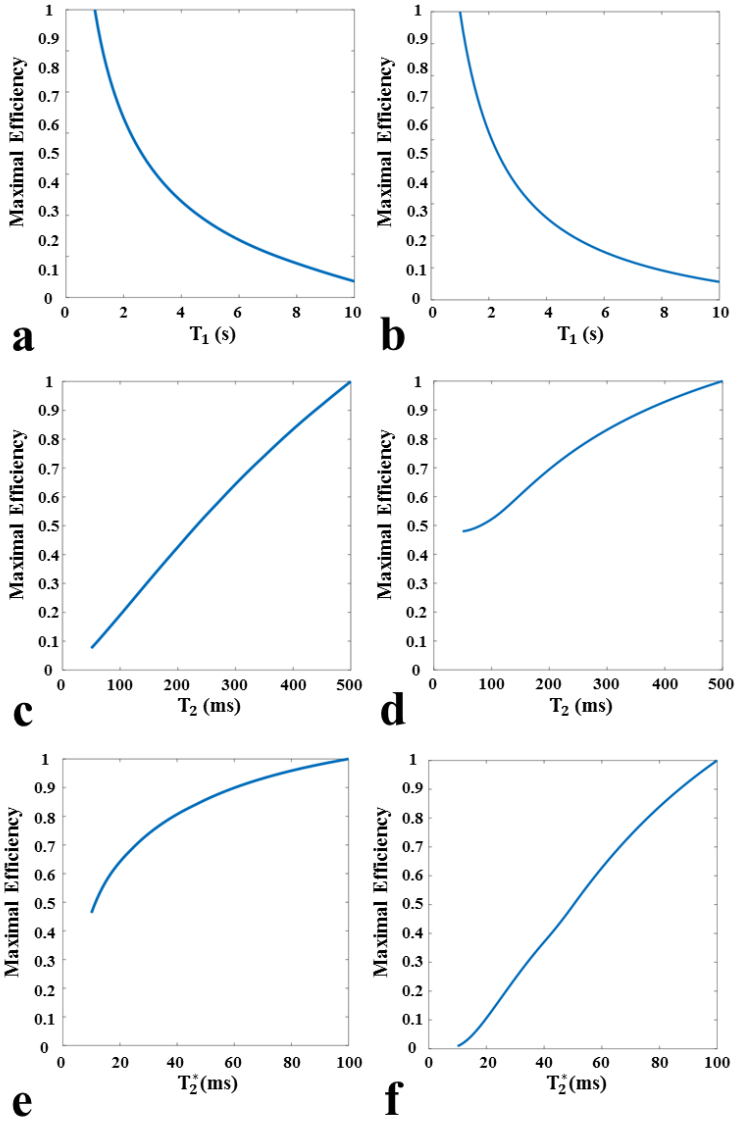

Figure S4: MESE and SSFP-FID$_{FCI}$ maximal efficiency dependence on relaxation parameters T_1, T_2, and T_2^*: (a,c,e) MESE and (b,d,f) SSFP-FID$_{FCI}$. The simulations were performed by varying one of the relaxation parameters and setting the other two close to brain tissue parameters (T_1 = 1.1 s, T_2 = 100 ms, T_2^* = 50 ms). The simulations are normalized by their maximum.

C APPENDIX

HUMAN IN-VIVO MR CURRENT DENSITY IMAGING (MRCDI) BASED ON OPTIMIZED MULTI-ECHO SPIN ECHO (MESE)

The following abstract was accepted for the annual scientific meeting of International Society for Magnetic Resonance in Medicine (ISMRM) 2017.

Human In-vivo MR Current Density Imaging (MRCDI) Based on Optimized Multi-echo Spin Echo (MESE)

Cihan Göksu[1-2], Lars G. Hanson[1-2], Philipp Ehses[3-4], Klaus Scheffler[3-4], and Axel Thielscher[1-2-3]

[1] Danish Research Centre for Magnetic Resonance, Centre for Functional and Diagnostic Imaging and Research, Copenhagen University Hospital Hvidovre, Denmark, [2] Center for Magnetic Resonance, DTU Elektro, Technical University of Denmark, Kgs Lyngby, Denmark, [3] High-Field Magnetic Resonance Center, Max-Planck-Institute for Biological Cybernetics, Tübingen, Germany, [4] Department of Biomedical Magnetic Resonance, University of Tübingen, Tübingen, Germany

Synopsis:
MRCDI aims at imaging an externally injected current flow in the human body, and might be useful for many biomedical applications. However, the method requires very sensitive measurement of the current-induced magnetic field component $\Delta B_{z,c}$ parallel to main field. We systematically optimized MESE to determine its most efficient parameters. In one of the first human in-vivo applications of MRCDI, the optimized sequence was successfully used to image the $\Delta B_{z,c}$ distribution in the brain caused by a two-electrode montage, as confirmed by finite-element calculations of $\Delta B_{z,c}$. Further improvements will be performed to increase its robustness to field drifts.

Purpose: Imaging the current distribution injected by external electrodes in the human brain might be useful in many biomedical applications, and could, e.g. be used to reconstruct the ohmic tissue conductivities. However, in-vivo human brain MRCDI allows only for weak electrical current injection, i.e. 1-2 mA, which severely limits its sensitivity.[1] We aimed for a systematic sensitivity analysis of MESE to determine the most efficient sequence parameters for human brain imaging, and for a systematic experimental validation in phantoms. Finally, we aimed at applying the optimized sequence for in-vivo MRCDI of the human brain.

Theory and Methods:
The injected current I_c creates a magnetic field $\Delta B_{z,c}$ inside brain, which is parallel to main MR field. This field causes small frequency shifts, and can be measured using MR phase images. Here, we employ MESE (Fig. 1) due to its high sensitivity, image quality, and robustness to field inhomogeneities and flow artifacts. The bipolar current is injected in synchrony with the sequence, and multiple echoes with linearly increasing current induced phases (Fig. 2b) are acquired. $\Delta B_{z,c}$ images from each echo are calculated and optimally combined. The efficiency of MESE MRCDI η_{MESE} is given in Eq. 1,

$$\eta_{MESE} = \frac{\left|\Delta B_{z,c}^{comb}\right|}{\sqrt{T_{tot}}} \sqrt{\sum_{n=1}^{N_{echo}} 4\gamma^2 SNR_n^2 \left[\left(T_{ES} - \tau_\pi\right) n - 0.5\tau_{\pi/2}\right]^2}$$

N_{echo}, γ, SNR_n, T_{ES}, τ_π, $\tau_{\pi/2}$, and T_{tot} are the total number of echoes, gyromagnetic ratio, signal to noise ratio of n^{th} echo, echo spacing, refocusing and excitation pulse-width, and the total measurement time, respectively.

First, an experiment was performed in a saline-filled spherical phantom with relaxation parameters like brain tissue (T_1 = 1 s, T_2 = 100 ms) to determine optimized sequence parameters N_{echo} and T_{ES}. Then, an in-vivo brain experiment was conducted with a 30-years old healthy male volunteer. Two MRI compatible 5x7 cm^2 rubber electrodes were placed on the head above the temporoparietal junctions of the brain. The current waveform was generated using an arbitrary waveform generator (33500B, KEYSIGHT Technologies, California, United States) and an MRI compatible transcranial current stimulator (DC-STIMULATOR PLUS, neuroConn GmbH, Germany).

Two different MESE experiments with positive and negative bipolar currents were performed with field of view FOV = 256x256mm^2, image matrix = 128x128, voxel size of 2x2x3mm^3, N_{avg} = 1x2 (for positive and negative current injection), T_{ES} = 60 ms, dead time T_D = 1.5 s, and I_c = 1mA. In the first experiment, the number of spin echoes N_{SE} = 4 and multiple gradient echoes N_{GE} = 1 (the total number of echoes $N_{echo} = N_{SE} \times N_{GE}$; bandwidth BW = 20.2 Hz/pix) were selected. The long T_{ES}

results in low-bandwidth data acquisition, causing artifacts. This can be prevented by multiple gradient echo acquisition within each T_{ES} with a very small loss of SNR. Therefore, the second experiment was repeated with $N_{SE} = 4$ and $N_{GE} = 5$ (BW = 115.2 Hz/pix). For comparison, a head model of the subject was created and the $\Delta B_{z,c}$ simulated by the finite-element method included in SIMNIBS [2] (conductivities: 0.126 S/m for white matter, 0.275 S/m for gray matter, 1.654 S/m for cerebrospinal fluid).

Results: The reconstructed $\Delta B_{z,c}$ inside phantom (Fig. 2a) is as expected for a current flow from top to bottom. The linear increase in the current induced phase is shown for different echo spacings (Fig. 2b). The most efficient sequence parameters (Fig. 2c,d) are T_{ES} = [60-100] ms, N_{echo} = [2-4], T_D = 1.5 ms. The MR magnitude images of the human brain are shown in Fig. 3a,b, and the reconstructed $\Delta B_{z,c}$ images are depicted in Fig. 3c,d (given the occurrence of a spurious $\Delta B_{z,c}$ offset, the mean-corrected image is shown for easier interpretation). Acquiring single echo with this long T_{ES} caused image distortions, which were avoided by multiple gradient echo acquisition. The measured and simulated $\Delta B_{z,c}$ images show the same general distribution (Fig. 4), with strong field changes close to the CSF-filled and well-conducting sulci underneath the electrodes.

Discussion and Conclusion: By multi-gradient echo acquisition, the low-bandwidth artifacts are eliminated. The simulation result of the generated head model and the measurements look similar. Large magnetic field changes induced by high current density in sulcus regions are well observed near pads (Fig 3c,d). The differences between simulations and experiments may arise from rough estimation of the conductivities and anisotropy in the simulations, the spurious magnetic field induced by the current flow in the cables or electrodes, or scanner imperfections. The effect of flow, motion, and static field inhomogeneities should also be considered. Nevertheless, this study demonstrates a successful initial measurement of $\Delta B_{z,c}$ for in-vivo MRCDI.

Acknowledgements: The project is supported by Lundbeck foundation with grant number R118-A11308.

References: 1. Utz KS, Dimova V, Oppenländer K, Kerkhoff G. Electrified minds: Transcranial direct current stimulation (tDCS) and Galvanic Vestibular Stimulation (GVS) as methods of non-invasive brain stimulation in neuropsychology-A review of current data and future implications. Neuropsychologia 2010;48(10):2789–2810.

2. Thielscher A, Antunes A, Saturnino GB. Field modeling for transcranial magnetic stimulation: A useful tool to understand the physiological effects of TMS?, 2015. Milan, Italy: Proc. Annu. Int. Conf. IEEE Eng. Med. Biol. Soc. EMBS; 2015.

FIGURES:

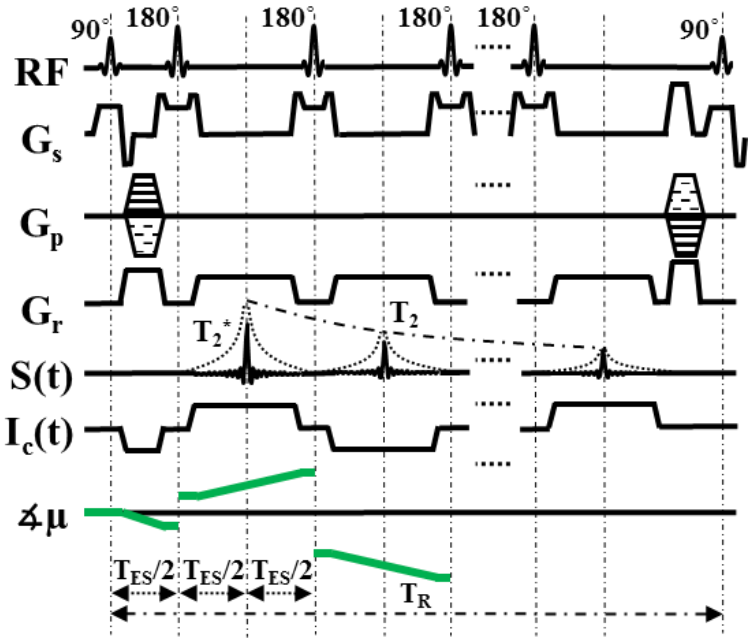

Figure 1. Diagram of the MESE pulse sequence with equal and symmetric echo spacing. The sequence is composed of a 90˚ excitation pulse preceding repetitive 180˚ refocusing pulses, so that multiple echoes are created. Crusher gradients are used to preserve only the desired echo pathways. At the end of the sequence, phase encoding rewinder and spoiler gradients are employed to eliminate the remaining transverse magnetization. The injected bipolar electrical current is synchronized with radio frequency (RF) pulses, so that the phase of the continuous complex transverse magnetization (∢μ) increases linearly over time.

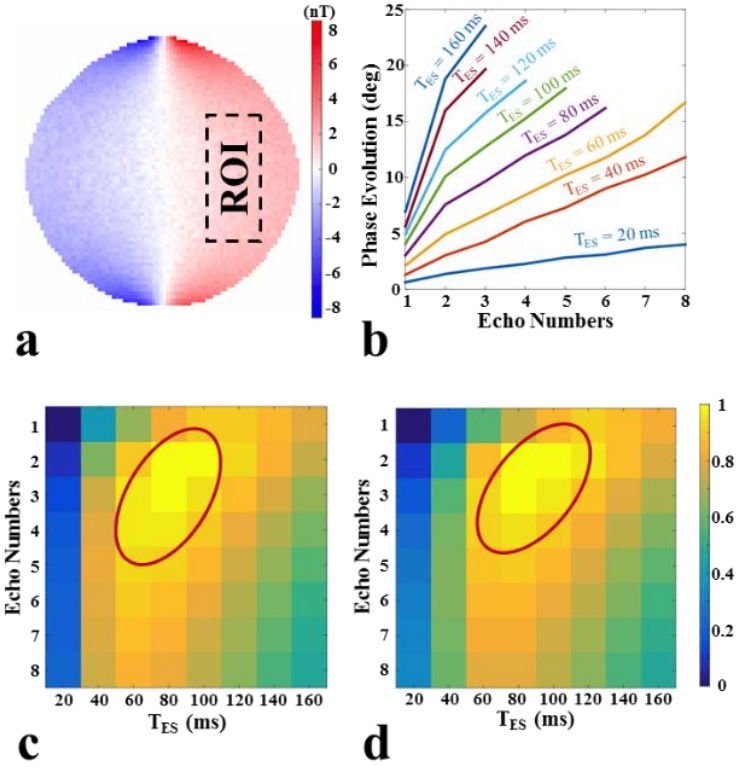

Figure 2. MESE simulation and measurement results in the phantom. (a) An example of combined $\Delta B_{z,c}$ measurement for I_c = 0.5 mA. The region of interest (ROI) used to calculate the efficiency is shown by the dashed lines. (b) Measured phase evolution. (c) Simulated efficiency. (d) Measured efficiency. The results in (c-d) are normalized, and FOV = 300x300 mm^2, image matrix = 256x256, Δz = 5 mm, N_{slice} = 1, N_{avg} = 1, N_{echo} = [1–8], T_{ES} = [20–160] ms, T_D = 510 ms, T_1 = 1.1 s, T_2 = 100 ms, T_2^* = 50 ms, and I_c = 0.5 mA.

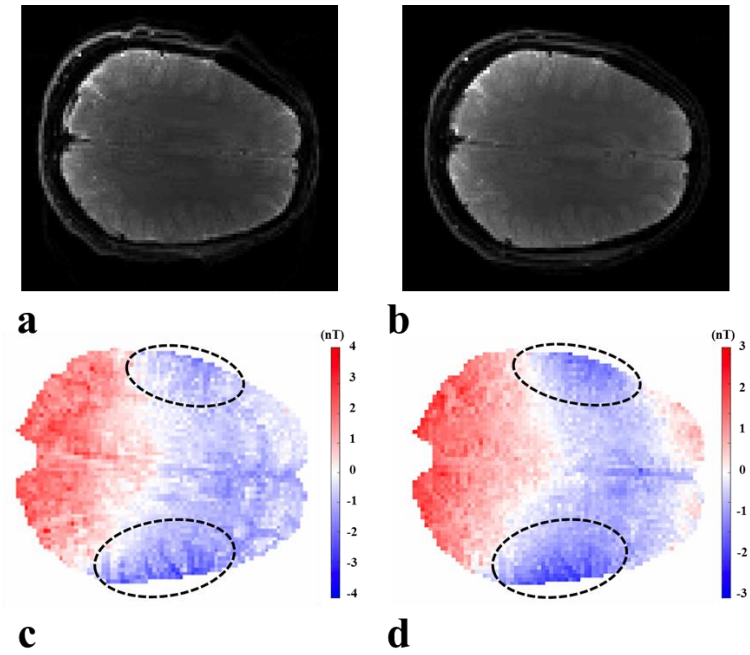

Figure 3. In-vivo MESE results in human brain. (a,b) MR magnitude images. (c,d) Reconstructed $\Delta B_{z,c}$ images. Number of spin echoes N_{SE} = 4 and number of gradient echoes N_{GE} = 1 are selected in (a,c), and N_{SE} = 4 and number of gradient echoes N_{GE} = 5 are selected in (b,d). Other parameters are field of view FOV = 256x256mm2, image matrix = 128x128, voxel size of 2x2x3mm3, Navg = 1x2 (for positive and negative current injection), T_{ES} = 60 ms, dead time TD = 1.5 s, and Ic = 1mA.

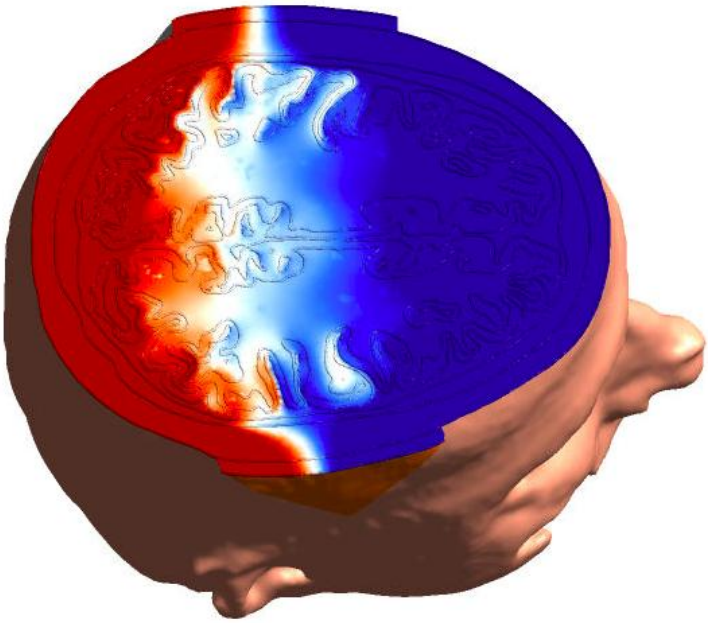

Figure 4. The $\Delta B_{z,c}$ simulations are performed by finite-element calculations in generated head model of the subject. The $\Delta B_{z,c}$ results are normalized in the full range (max:red and min:blue).The assigned electrical conductivities are 0.126 S/m for white matter, 0.275 S/m for gray matter, and 1.654 S/m for cerebrospinal fluid, 0.01 S/m.

D APPENDIX

HUMAN IN-VIVO BRAIN MAGNETIC RESONANCE CURRENT DENSITY IMAGING (MRCDI)

The following manuscript is in preparation.

Human In-vivo Brain Magnetic Resonance Current Density Imaging (MRCDI)

Cihan Göksu[1,2], Lars G. Hanson[1,2], Hartwig R. Siebner[1,5], Philipp Ehses[3,6], Klaus Scheffler[3,4†], and Axel Thielscher[1,2,3†*]

[1] Danish Research Centre for Magnetic Resonance, Centre for Functional and Diagnostic Imaging and Research, Copenhagen University Hospital Hvidovre, Denmark.

[2] Center for Magnetic Resonance, DTU Elektro, Technical University of Denmark, Kgs Lyngby, Denmark.

[3] High-Field Magnetic Resonance Center, Max-Planck-Institute for Biological Cybernetics, Tübingen, Germany.

[4] Department of Biomedical Magnetic Resonance, University of Tübingen, Tübingen, Germany.

[5] Department of Neurology, Copenhagen University Hospital, Bispebjerg, Denmark.

[6] German Center for Neurodegenerative Diseases (DZNE), Bonn, Germany

[†] These authors contributed equally to this work.

***** Corresponding Author

Axel Thielscher, Assoc. Prof.

Danish Research Centre for Magnetic Resonance, Centre for Functional and Diagnostic Imaging and Research, Copenhagen University Hospital Hvidovre, Section 714, Kettegaard Allé 30, 2650 Hvidovre, Denmark.

Tel: + 45-38623326

e-mail: axelt@drcmr.dk

ABSTRACT

Magnetic resonance current density imaging (MRCDI) and MR electrical impedance tomography (MREIT) are two emerging modalities, which combine weak time-varying currents injected via surface electrodes with magnetic resonance imaging (MRI) to acquire information about the current flow and ohmic conductivity distribution at high spatial resolution. The injected current flow creates a magnetic field in the head, and the component of the induced magnetic field $\Delta B_{z,c}$ parallel to the main scanner field causes small shifts in the precession frequency of the magnetization. The measured MRI signal is modulated by these shifts, allowing to determine $\Delta B_{z,c}$ for the reconstruction of the current flow and ohmic conductivity.

Here, we demonstrate reliable $\Delta B_{z,c}$ measurements in-vivo in the human brain based on multi-echo spin echo (MESE) and steady-state free precession free induction decay (SSFP-FID) sequences. In a series of experiments, we optimize their robustness for in-vivo measurements while maintaining a good sensitivity to the current-induced fields. We validate both methods by assessing the linearity of the measured $\Delta B_{z,c}$ with respect to the current strength. For the more efficient SSFP-FID measurements, we demonstrate a strong influence of magnetic stray fields on the $\Delta B_{z,c}$ images, caused by non-ideal paths of the electrode cables, and validate a correction method. Finally, we perform measurements with two different current injection profiles in five subjects. We demonstrate reliable recordings of $\Delta B_{z,c}$ fields as weak as 1 nT, caused by currents of 1 mA strength. Comparison of the $\Delta B_{z,c}$ measurements with simulated $\Delta B_{z,c}$ images based on FEM calculations and individualized head models reveals significant linear correlations in all subjects, but only for the stray field-corrected data. As final step, we reconstruct current density distributions from the measured and simulated $\Delta B_{z,c}$ data. Reconstructions from non-corrected $\Delta B_{z,c}$ measurements systematically overestimate the current densities. Comparing the current densities reconstructed from corrected $\Delta B_{z,c}$ measurements and from simulated $\Delta B_{z,c}$ images reveals an average coefficient of determination R^2 of 71%. In addition, it shows that the simulations underestimated the current strength on average by 24%.

Our results open up the possibility of using MRI to systematically validate and optimize numerical field simulations that play an important role in several neuroscience applications, such as transcranial brain stimulation, and electro- and magnetoencephalography.

Key words:

Current-induced magnetic field, magnetic resonance current density imaging, multi-echo spin echo, steady-state free precession free induction decay, in-vivo imaging

INTRODUCTION

Accurate knowledge of the current flow distribution in the human head caused by neural or external sources is important in several neuroscience applications such as targeting control in transcranial brain stimulation (TBS) and source localization in electro- (EEG) and magnetoencephalography (MEG) (Mosher et al., 1999; Nitsche and Paulus, 2000). The current distributions are usually derived using forward modeling schemes that employ volume conductor models of the head (Thielscher et al., 2015; Oostenveld et al., 2011; Tadel et al., 2011). However, even anatomically accurate models of the head still suffer from uncertainties of the tissue conductivities. The conductivity values reported in literature vary substantially across studies, likely caused by both methodological differences and natural physiological variability, with the amount of uncertainty depending on the tissue type (Miranda, 2013; Faes et al., 1999; Dabek et al., 2016; Huang et al., 2017). Methods to measure the current flow non-invasively in-vivo are thus important for the validation and improvement of these forward modelling approaches.

Magnetic resonance current density imaging (MRCDI) and MR electrical impedance tomography (MREIT) are two emerging modalities, which combine weak time-varying currents injected via surface electrodes with magnetic resonance imaging (MRI) to acquire information about the current flow and ohmic conductivity at high spatial resolution (Eyüboğlu, 2006a, 2006b; Göksu et al., 2014; Joy, 2004; Scott et al., 1991; Seo and Woo, 2011a; Woo et al., 1994). In short, the injected current flow creates a magnetic field in the head, and the component of the induced magnetic field $\Delta B_{z,c}$ parallel to the main magnetic field of the scanner slightly changes the precession frequency of the magnetization (here, the z-axis is chosen along the static scanner field, and $\Delta B_{z,c}$ is correspondingly the current-induced field change). This modulates the phase of the measured MRI signal proportional to $\Delta B_{z,c}$. The current-induced phase changes can thus be used to determine $\Delta B_{z,c}$, and to reconstruct the inner current flow and the ohmic conductivity distribution (Eyüboğlu, 2006b, 2006c; Ider and Birgül, 1998; Joy, 2004; Oh et al., 2003; Scott et al., 1991; Seo and Woo, 2011b).

Up to now, successful MRCDI and MREIT recordings have been demonstrated in phantoms, animal models and in-vivo in human limbs (Birgül et al., 2003; Han et al., 2010; Ider and Birgül, 1998; Jeon et al., 2009; Jeong et al., 2010; Kim et al., 2009, 2008, 2011; Meng et al., 2012; Oh et al., 2003, 2005; Sadighi et al., 2014; Sadleir et al., 2005; Seo and Woo, 2011b; Woo and Seo, 2008). However, in order to achieve a sufficient signal-to-noise ratio (SNR) of the $\Delta B_{z,c}$ images, these studies applied current strengths that were much higher than those applicable for in-vivo human brain applications (1-2 mA; Utz et al., 2010). Only recently, the first proof-of-principle studies have been performed that demonstrated the feasibility of acquiring $\Delta B_{z,c}$ images for the human brain in-vivo using weak current strengths (Jog et al., 2016; Kasinadhuni et al., 2017). These initial results are promising, but highlight

the need for further improvements of the measurement procedures and sequences to allow for sufficient quality and unambiguous $\Delta B_{z,c}$ images in a reasonable acquisition time.

Using comprehensive theoretical analyses and phantom measurements, we have previously optimized the sensitivity of two MRI sequences for in-vivo MRCDI and MREIT measurements in the human brain (Göksu et al., 2017). We explored multi-echo spin echo (MESE) and steady-state free precession free induction decay (SSFP-FID) sequences, and derived optimized parameters to maximize their efficiency for measuring current-induced phase changes, given relaxation parameters of brain tissue at 3 T. Here, we validate the performance of the optimized sequences for in-vivo brain imaging and improve their robustness to artifacts that are of concern in an in-vivo setting, in order to ensure the validity of the results. Using the adapted approach, we perform measurements with two different current injection profiles in five subjects using SSFP-FID, and demonstrate reliable recordings of $\Delta B_{z,c}$ fields as weak as 1 nT. We compare the $\Delta B_{z,c}$ measurements with simulations based on the Finite-Element Method (FEM) and individualized head models reconstructed from structural MR images of the same subjects. As final step, we reconstruct the current flow distributions from both the measured and simulated $\Delta B_{z,c}$ data. Taken together, the results presented here highlight the importance of careful validation of the measurement procedures to ensure unambiguous current density reconstructions. They optimize the novel $\Delta B_{z,c}$ measurements for in-vivo applications, and pave the way for their application in future MRCDI and MREIT studies of the human brain.

METHODS

Subjects

Thirteen healthy subjects were included in the study, which consisted of five successive experiments. Five participants took part in two of the experiments, and two participated three times. They had no previous history of neurological or psychiatric disorders and were screened for contraindications to MRI and TBS. Written informed consent was obtained from all participants prior to the scans. The study complied with the Helsinki declaration on human experimentation and was approved by the Ethics Committee of the Capital Region of Denmark (H16032361).

Sequence of Experiments

Our study is organized in five successive experiments:

- First, we compare the SNR and quality of $\Delta B_{z,c}$ images acquired with single- vs. multi-gradient-echo readouts. Our prior results demonstrated the need to use long echo times for MESE and long repetition times for SSFP-FID in order to maximize efficiency. The resulting SNR-optimal low readout bandwidth (BW) decreases image quality as it causes considerable distortions particularly for in-vivo applications. Here, we test to which extent these effects can be prevented by using multi-

gradient-echo readouts that are acquired at a higher BW and that are subsequently combined to reconstruct the $\Delta B_{z,c}$ image.

- Second, we validate the methods by assessing the linearity of the measured $\Delta B_{z,c}$ with respect to the strength of the injected currents.
- Third, we focus on the more efficient SSFP-FID measurements and assess the influence of magnetic stray fields on the $\Delta B_{z,c}$ images, caused by non-ideal paths of the feeding cables that are connected to the electrodes. We propose and validate a method to correct for these undesired influences.
- Fourth, we re-evaluate the impact of the chosen repetition times on measurement efficiency and image quality in the presence of physiological noise. We test whether decreasing the repetition times below the theoretically optimal values can help to improve image quality without substantially sacrificing the SNR of the $\Delta B_{z,c}$ images.
- Fifth, we perform $\Delta B_{z,c}$ measurements with two different current injection profiles (right-left and anterior-posterior), and compare the measurements with simulations based on the Finite-Element Method (FEM) and individualized head models reconstructed from structural MR images of the same subjects. We also reconstruct and compare the current density distributions from the measured and simulated $\Delta B_{z,c}$ data. For both the $\Delta B_{z,c}$ images and current flow distributions, we test how much the correction of the cable-induced magnetic stray fields affects the similarity between measured and simulated data.

MRI sequences for MRCDI

We tested the in-vivo application of two different MRCDI sequences, MESE (Fig. 1a) and SSFP-FID (Fig. 1b). Details of the sequences can be found in (Göksu et al., 2017). In short, we selected MESE because of its high SNR for the magnitude images and its robustness to field inhomogeneity (Nam and Kwon, 2010), and SSFP-FID for its high phase sensitivity (Lee et al., 2016; Scheffler et al., 2006).

For MESE (Fig. 1a), the measured current-induced magnetic field for the n^{th} spin-echo $\Delta B_{z,c}^{n}$ is given as

$$\Delta B_{z,c}^{n} = (\angle M_n^{+} - \angle M_n^{-}) / 2\gamma T_{ES} n, \quad (1)$$

where γ is the gyromagnetic ratio of protons, and T_{ES} the echo spacing. The measurement is performed twice with opposite current injection profiles, and $\angle M_n^{+}$ and $\angle M_n^{-}$ are the phases of the acquired complex MR images for the positive and negative current directions for the n^{th} echo (Göksu et al., 2017; Nam and Kwon, 2010; Scott et al., 1992). The final $\Delta B_{z,c}$ image is determined as the weighted sum of the $\Delta B_{z,c}^{n}$ images of the single echoes, with the weightings being proportional to the inverse of the variances of the images (Göksu et al., 2017). When a multi-gradient-echo readout is used, the final $\Delta B_{z,c}$ image is determined in the same way after summation across all acquired gradient echoes.

For SSFP-FID (Fig. 1b), the $\Delta B_{z,c}$ image in case of weak injection currents is given as

$$\Delta B_{z,c} = \frac{\angle M_{SS1} - \angle M_{SS2}}{m_{seq}}, \quad (2)$$

with $\angle M_{SS1}$ and $\angle M_{SS2}$ being the phase images for echoes with positive and negative current injection. The constant $m_{seq} = \partial\left(\angle M_{SS1} - \angle M_{SS2}\right)/\partial \Delta B_{z,c}$ is the phase sensitivity to magnetic field changes (Göksu et al., 2017). We calculated it via spin simulations based on 3D rotation and relaxation matrices (Jaynes, 1955), and it depends on the sequence and tissue relaxation parameters.

Measurement procedures

All experiments were performed on a 3 T MRI scanner (MAGNETOM Prisma, SIEMENS Healthcare, Erlangen, Germany) equipped with a 64-channel head coil. Multi-channel signals were combined using an adaptive combine algorithm (Walsh et al., 2000). The electrical current waveforms were created using a waveform generator (33500B; Keysight Technologies, Santa Clara, CA, USA), amplified using an MR-conditional device for transcranial weak current stimulation (DC-STIMULATOR PLUS, neuroConn GmbH, Ilmenau, Germany), and were applied to the participants via circular rubber electrodes (5 cm in diameter) attached to the scalp. We used two different electrode configurations that created current flows either from right to left (R-L) or from anterior to posterior (A-P) in the brain. For R-L current injection, the rubber electrodes were attached symmetrically at positions directly above and slightly anterior to the ears using conductive paste (Ten20, Weaver and Company, Colorado, USA). This corresponds roughly to positions above the temporoparietal junctions. For A-P injection, one electrode was placed centrally on the forehead and the second centrally superior to the inion. Unless stated otherwise, peak current amplitudes of ± 1 mA were used. A ramp up period of 10 s was used in order to prevent sudden subject motion. MR data acquired during this period were discarded.

We used single-slice MESE and SSFP-FID measurements, with an axial slice placed in the upper half of the brain. Based on an initial structural image (details are given below), the slice position was chosen to contain approximately the electrode centers. The fat signal was suppressed by a chemical-shift-selective (CHESS) fat suppression technique (Haase et al., 1985). A field of view (FOV) of 224x180 mm^2, an image matrix of 112x90 and a voxel size of 2x2x3 mm^3 was used for both sequence types. For MESE, the echo spacing was T_{ES} = 60 ms, repetition time was T_R = 1.5 s and the number of spin echoes was N_{SE} = 3. For SSFP-FID, the tip angle was $\alpha = 30^\circ$. The other MR sequence parameters varied across experiments and are stated below. All experiments were performed with both positive and negative current directions (i.e. two subsequent acquisitions of each k-space line; the first corresponds to the positive direction and the second to the negative). The current waveforms were employed as indicated in Figure 1 (I_c^+ for the first acquisition and I_c^- for the second). By that, each k-space line was acquired twice in successive readout periods with opposite currents I_c^+ and I_c^- to measure two phase images

with opposite current-induced phases. After acquisition of the complete k-space, the measurements were repeated. The MESE measurements were repeated twice (N_{meas} = 2), with a total scan time of T_{tot} ≈ 9 mins. For SSFP-FID, the number of measurements N_{meas} varied across experiments and are stated below. Generally, they were selected as high as possible while limiting the total duration of each experiment for the participants to 1.5 hours.

For all subjects, a high-resolution structural image was acquired using the Pointwise Encoding Time reduction with Radial Acquisition (PETRA) sequence (Ida et al., 2015) with number of slices N_{sli} = 320, image matrix 320x320, voxel size 0.9x0.9x0.9 mm^3, tip angle $\alpha = 6^\circ$, T_R = 3.61 ms, T_E = 0.07 ms, inversion time T_I = 0.5 s, BW = 359 Hz/pixel, and turbo factor 400. The images exhibited a T_1-weighted contrast for soft tissue. In addition, it allowed locating the rubber of the electrodes and of the cable insulations due to the short T_E. The visibility of the cable tracks was further improved by covering them with Play-Doh (Hasbro Inc., RI, USA) which provides strong MRI signal due to its high water content.

For participants in which the current flow distribution was estimated using FEM calculations, additional T_1- and T_2-weighted images were acquired for the construction of individualized volume conductor models. The T_1-weighted images were based on a Magnetization-Prepared Rapid Acquisition Gradient-Echo (MPRAGE) sequence with number of slices N_{sli} = 208, image matrix 256x256, voxel size 1x1x1 mm^3, tip angle $\alpha = 9^\circ$, T_R = 2700 ms, T_E = 3.63 ms, and inversion time T_I = 1090 ms with selective water excitation. The T_2-weighted images used a Sampling Perfection with Application-optimized Contrasts using different flip-angle Evolutions (SPACE) sequence with N_{sli} = 208, image matrix 256x256, voxel size 1x1x1 mm^3, T_R = 3200 ms, T_E = 408 ms, and turbo factor 282.

Experiment 1: Single- vs. Multi-gradient-echo acquisition

In three participants, we compared the quality and SNR of the $\Delta B_{z,c}$ images based on multi-gradient-echo readouts at high BW versus their single-gradient-echo counterparts at low BW, employing an R-L electrode montage. The experiments were performed both with and without current injection. The MESE experiments were repeated for N_{GE} = 1 (BW = 19.2 Hz/pixel; echo time point relative to the preceding refocusing pulse: T_{GE}=30 ms) and N_{GE} = 5 (BW = 103.6 Hz/pixel; gradient echo time points relative to the preceding refocusing pulse: T_{GE}=[8.8, 19.6, 30, 40.6, 51.2] ms). The SSFP-FID experiments were performed with T_R = 120 ms and N_{meas} = 12 (T_{tot} ≈ 4.5 mins). They were repeated for N_{GE} = 1 (BW = 12 Hz/pixel; gradient echo time point relative to the preceding RF pulse: T_{GE}=60 ms) and N_{GE} = 7 (BW = 75 Hz/pixel; gradient echo time points: T_{GE} = [8.33, 22.43, 36.53, 50.63, 64.73, 79.00, 93.16] ms).

MESE was tested at its optimal T_{ES} of 60 ms, while SSFP-FID was tested at its optimal T_R of 120 ms, resulting in a different number of readouts for the multi-gradient-echo cases. For both sequences, the number of readouts was chosen to result in a BW that was high enough to prevent visible distortions.

The quality of the resulting $\Delta B_{z,c}$ images was evaluated by visual inspection. In addition, the performance of the methods was quantified by creating histograms of the noise floor in the $\Delta B_{z,c}$ images acquired without current injection. For that, masks created from the magnitude images were used to extract the values from the brain. Gaussian distributions were fitted to the histograms, and the differences in the mean $\mu_{\Delta Bz,c}$ and standard deviation $\sigma_{\Delta Bz,c}$ of the fits were evaluated.

Experiment 2: Linear dependence of the measured $\Delta B_{z,c}$ on current strength

In order to verify the linear dependence of the measured $\Delta B_{z,c}$ on the strength of the injected currents, MESE and SSFP-FID experiments using multi-gradient-echo readouts were performed in four participants. The data of one subject was discarded due to severe motion artefacts. For MESE, $N_{GE} = 5$ was used. The parameters for SSFP-FID were $T_R = 120$ ms, $N_{meas} = 12$ and $N_{GE} = 7$. For each participant, measurements at four currents strength ($I_c = 0$, 0.33, 0.66 and 1 mA) were acquired in random order, using an R-L electrode montage. This resulted in 4x12=48 SSFP-FID and 4x2=8 MESE measurements per participant. For each measurement, average $\Delta B_{z,c}$ values were extracted from a region-of-interest (ROI) that was individually positioned to exhibit clear current-induced phase changes for the MESE measurements at 1 mA. Linear regression models of the extracted $\Delta B_{z,c}$ values as a function of I_c were fitted both to the MESE and SSFP-FID results, and the mean shifts β_0 and slopes β_1 and their standard errors are reported.

Experiment 3: Correction of cable-induced stray magnetic fields

Given the higher efficiency of SSFP-FID compared to MESE (Göksu et al., 2017), we focused on SSFP-FID in the rest of the study. The sequence parameters were $T_R = 120$ ms, $N_{meas} = 24$ ($T_{tot} \approx 9$ mins) and $N_{GE} = 7$. In the proximity of the head, the cables connecting the electrodes to the current stimulator should be fully parallel to the main magnetic field of the scanner. This ensures that the magnetic fields created by the current flow through the cables do not contribute to the phase of the measured MR images. Any deviation from an ideal parallel cable path can result in strong stray fields which change the measured $\Delta B_{z,c}$ distribution. For example, a straight wire of 10 cm length that carries a current of 1 mA and is placed parallel to an axial imaging plane at a distance of 10 cm changes the z-component of the magnetic field in the plane by up to 0.9 nT. This is approximately the situation encountered if the electrode cables meet just above or below the head, and the resulting field change is similar to that caused by current flow inside the head. However, parallel cable paths are difficult to achieve in practice, as modern multichannel receive coils fit tightly around the head. Changing to, e.g. birdcage coils would strongly reduce the SNR of the measurements. In addition, in our measurements, the stray fields were severe as we employed a twisted wire pair that branched out only in close proximity to the head. This was caused by the need to employ stimulator equipment that was CE approved as medical device.

Using SSFP-FID measurements in four participants, we demonstrated the impact of the cable-induced stray fields on the $\Delta B_{z,c}$ images. A wire loop was placed around the head, with the upper half following a similar path as the cables in the other measurements. The lower half of the loop was extended inferior, with the wires being as parallel as possible to the main magnetic field for 30 cm before they were twisted and connected to the stimulator. By that, the stray field of the wire loop coarsely mimicked that of the cables in the axial imaging slice in the upper part of the head.

In order to correct for the effects of the stray field, we reconstructed the wire path from the PETRA images, calculated the wire-induced field using the Biot-Savart Law, and subtracted it from the measured $\Delta B_{z,c}$ image. We validated this correction method by comparing the corrected $\Delta B_{z,c}$ images with the results of control measurements without current injection. Histograms of both measurements were obtained, and the mean and standard deviation of Gaussian distributions fitted to the histograms were compared. For both the experiments with and without current flow, $N_{meas} = 24$ measurements were used. The experiments were repeated twice to test the reproducibility of the results.

Experiment 4: Dependence of measurement efficiency on repetition time

In our prior study (Göksu et al., 2017), we employed phantom experiments and simulations to demonstrate a strong influence of the SSFP-FID repetition time T_R (Fig. 1b) on the efficiency of the MRCDI measurements. We derived an optimal value of $T_R = 120$ ms, which is higher than usually employed in order to allow for sufficient phase accumulation. However, a long T_R can also increase the influence of physiological noise on the measurements, leading us to re-evaluate the impact of T_R on measurement efficiency in the in-vivo case.

We performed SSFP-FID experiments in six participants, employing an R-L electrode montage. The experiments were repeated with and without current injection. The data of one subject was discarded due to severe motion artefacts. In each participant, three repetition times $T_R = [40, 80, 120]$ ms were tested in a random order. The number of measurement repetitions N_{meas} was adjusted to keep the total acquisition time T_{tot} close to 9 mins. The remaining MR sequence parameters were adjusted to optimize the measurement sensitivity and image quality for the given T_R:

- $T_R = 40$ ms: $T_{GE} = 20$ ms, $N_{GE} = 1$, BW = 276 Hz/pixel, $N_{meas} = 72$
- $T_R = 80$ ms: $T_{GE} = [7.46, 19.73, 31.86, 43.99, 56.13]$ ms, $N_{GE} = 5$, BW = 88 Hz/pixel, $N_{meas} = 36$
- $T_R = 120$ ms: $T_{GE} = [8.33, 22.43, 36.53, 50.63, 64.73, 79.00, 93.16]$ ms, $N_{GE} = 7$, BW = 75 Hz/pixel, $N_{meas} = 24$

The $\Delta B_{z,c}$ images were corrected for the cable-induced stray fields as described above. Histograms of the $\Delta B_{z,c}$ images without current injection were obtained, and the mean and standard deviation of Gaussian distributions fitted to the histograms were determined.

Experiment 5: $\Delta B_{z,c}$ measurements for two different electrode montages

We compared the $\Delta B_{z,c}$ images obtained for R-L versus A-P electrode montages in six participants. The sequence parameters were T_R = 120 ms, N_{meas} = 24 ($T_{tot} \approx$ 9 mins) and N_{GE} = 7. The measurements were repeated with and without current injection. The data of one subject was discarded due to motion artefacts. The $\Delta B_{z,c}$ images were corrected for the cable-induced stray fields. Histograms of the $\Delta B_{z,c}$ images without current injection were obtained, and the mean and standard deviation of Gaussian distributions fitted to the histograms were determined.

FEM simulations of the current flow and the induced magnetic field

We compared the $\Delta B_{z,c}$ images measured in experiment 5 with simulated images, using FEM calculations of the current flow distribution inside the head based on our open-source pipeline SimNIBS 2 (www.simnibs.org; A Thielscher et al., 2015). An anatomically realistic volume conductor model was automatically created from the structural T_1 and T_2-weighted MR images. The model consists of five tissue compartments, namely brain gray matter (GM), white matter (WM), cerebrospinal fluid (CSF), skull and scalp. Isotropic ohmic conductivities were assigned to the tissues (WM: 0.126 S/m, GM: 0.275 S/m, CSF: 1.654 S/m, bone: 0.010 S/m, scalp: 0.465 S/m). The electrode positions were determined from the PETRA images. The electrode pads were modelled as disks with 50 mm diameter and 5 mm thickness with a conductivity of 1.0 S/m. For the FEM calculations, Dirichlet boundary conditions for the electrostatic potential were applied at the electrode surfaces (Saturnino et al., 2015). The simulations were performed for both R-L and A-P montages, assuming a current strength of I_c = 1 mA. The Biot-Savart Law was applied to the calculated current density distribution $\vec{J}$ in order to determine the $\Delta B_{z,c}$ image.

Reconstruction of current density images

The measured $\Delta B_{z,c}$ images for the two electrode montages R-L and A-P (experiment 5) were used to determine current density distributions. We reconstructed the x- and y-component of the current density in the imaging slice using the approach explained in (Ider et al., 2010; Park et al., 2007). The recovered current density $\vec{J}_{rec}$, termed "projected current density" in (Park et al., 2007), is given as

$$\vec{J}_{rec} = \vec{J}_0 + \frac{1}{\mu_0}\left(\frac{\partial(\Delta B_{z,c} - \Delta B^0_{z,c})}{\partial y}, -\frac{\partial(\Delta B_{z,c} - \Delta B^0_{z,c})}{\partial x}, 0\right) \quad (3)$$

with μ_0 being the permeability of free space. The variables $\vec{J}_0$ and $\Delta B^0_{z,c}$ denote the current density and magnetic field distributions that would occur for a uniform conductivity distribution inside the head. They were determined using FEM calculations. The projected current density images were reconstructed from both the measurements with and without stray field correction, and compared with the simulation results. A median filter (3x3 neighborhood) was applied to the $\Delta B_{z,c}$ measurements to

remove spatial high-frequency noise before applying the reconstruction algorithm. For comparability, the same filter was applied to the simulated $\Delta B_{z,c}$, even though it affected the images only marginally. There are more advanced filtering (Lee et al., 2011) and current density reconstruction (Ider et al., 2010; Park et al., 2007) techniques, which might perform slightly better. However, they are beyond the scope of this study.

RESULTS

Experiment 1: Single- vs. Multi-gradient-echo acquisition

For both the MESE and SSFP-FID measurements, the evaluation of the $\Delta B_{z,c}$ images acquired without current injection (Fig. 2a) shows that the multi-gradient-echo readouts consistently reduce the noise floor. In case of multiple echoes, the depicted $\Delta B_{z,c}$ images are the weighted sum of the single echo results, with the weighting factors being proportional to the inverse of the variances of the images (Göksu et al., 2017). The better quality of the multi-gradient-echo results is corroborated by the lower mean values and standard deviations obtained for the $\Delta B_{z,c}$ images of the multi-gradient-echo readouts, as listed in Table 1 (Supplementary Fig. S1 shows the corresponding histograms). In this respect, the mean values indicate $\Delta B_{z,c,}$ offsets, while the standard deviations characterize the "noise power", i.e. the strength of the spatial fluctuations of the noise. As a side note, the MESE measurements with multi-gradient-echo readouts have the lowest noise standard deviations across all four tested conditions. However, it should be noted that the listed values are not normalized per unit time, and the total scan time of MESE was two times longer than that of the SSFP-FID counterparts.

The use of multi-gradient-echo readouts also helps to improve the quality of the $\Delta B_{z,c}$ images obtained with current injection (Fig. 2b). Specifically, the results for the single-gradient-echo readouts suffer from ghosting-like patterns, which are absent when multi-gradient-echo readouts are used. Visual inspection suggests further that the multi-gradient-echo readouts result in more similar $\Delta B_{z,c}$ images for the MESE and SSFP-FID measurements in each of the three subjects.

Experiment 2: Linear dependence of the measured $\Delta B_{z,c}$ on current strength

Figure 3a shows the MR magnitude and $\Delta B_{z,c}$ images for MESE and SSFP-FID measurements performed at I_c = 1 mA. In each of the subjects, the $\Delta B_{z,c}$ images of the MESE and SSFP-FID measurements show a good similarity. Average $\Delta B_{z,c}$ values were extracted from the indicated ROIs for each of the four tested current strengths and plotted against the current strength in Fig. 3b. In all cases, the fitted regression models are highly significant, demonstrating a good linear dependency (Table 2). The mean shifts β_0 (i.e., the intercepts of the fits) are close to zero in all cases, which proves the absence of systematic biases. For all three subjects, the slopes β_1 are similar between the MESE and SSFP-FID

results. For SSFP-FID, the small standard errors indicate a good accuracy of the $\Delta B_{z,c}$ results that were obtained by averaging across twelve measurements.

Experiment 3: Correction of cable-induced magnetic stray fields

The $\Delta B_{z,c}$ fields created by currents flowing in a wire loop around the head and measured using SSFP-FID are shown in Fig. 4b. Corrected images were obtained by subtracting $\Delta B_{z,c}$ fields that were determined via forward calculations based on the reconstructed wire paths and the Biot-Savart Law (Fig. 4c).

Comparing the corrected images with control $\Delta B_{z,c}$ measurements without current injection (Fig. 4d) demonstrates that the remaining noise after the correction is in a similar range to that of the control images. This is confirmed by evaluating the mean values and standard deviations of the $\Delta B_{z,c}$ images, as listed in Table 3. For both experimental runs, the mean values of the corrected and control results are close to zero. The standard deviations are slightly higher for the corrected results, indicating a small residual effect that was not corrected by the subtraction procedure. The underlying reason might be small inaccuracies in determining the wire paths from the PETRA images.

Experiment 4: Dependence of SSFP-FID measurement efficiency on repetition time

The $\Delta B_{z,c}$ images acquired using SSFP-FID at three different repetition times, both with and without current injection, are shown in Figure 5. The images with current injection were corrected for the impact of the cable-induced stray fields as described above. The SNR of the images acquired at T_R = 40 ms is clearly lower than obtained at the two other repetition times. The results obtained at T_R = 80 ms and T_R = 120 ms exhibit similar sensitivities to the current-induced magnetic field changes. An exception is the $\Delta B_{z,c}$ image obtained for subject S_4 without current injection (fourth row of Fig. 5a), which has a poor quality compared to the other results, presumably due to motion. Comparison of the standard deviations of the $\Delta B_{z,c}$ images obtained without current injection confirms the visual impression (Table 4). On average, the standard deviation is reduced by 61% for T_R = 80 ms and 53% for T_R = 120 ms compared to the measurements at T_R = 40 ms. The measurements using T_R = 80 ms perform slightly better than those with T_R = 120 ms in four out of five subjects.

Experiment 5: $\Delta B_{z,c}$ measurements for two different electrode montages

The $\Delta B_{z,c}$ images obtained by SSFP-FID measurements for the R-L and A-P electrode montages are shown in Figure 6, both without (Fig. 6b) and with correction of the cable-induced stray fields (Fig. 6c). Visual comparison confirms the importance of applying the correction (please note, that the blue-red patterns are actually inversed between uncorrected and corrected images). Focusing on the corrected images (Fig. 6c), the results of the A-P montage exhibit very similar spatial distributions of the current-induced magnetic fields across the five subjects, while the obtained peak intensities clearly vary. The

results obtained with the R-L montage differ more between subjects, with the variation in the electrode positions likely contributing to these differences.

The control $\Delta B_{z,c}$ images obtained without current injection (Supplementary Fig. S2) exhibit an average mean shift of $\mu_{\Delta Bz,c}$ = 0.005 nT (averaged across the five subjects) and an average standard deviation of $\sigma_{\Delta Bz,c}$ = 0.111 nT. These values ensure a sufficient sensitivity when measuring magnetic field changes caused by the current flow at the chosen strength of 1 mA.

Comparison of measured and simulated current-induced magnetic fields $\Delta B_{z,c}$

We simulated the current-induced magnetic field for both the R-L and A-P electrode montages (Fig. 7a shows exemplarily the results for subject S_1). In general, the simulated and measured fields exhibit similar spatial distributions and variations, supporting the validity of the measurements. Scatter plots of the measurements (with and without correction of the stray fields) versus simulations show clear linear dependencies for the corrected $\Delta B_{z,c}$ data, which are absent for the uncorrected measurements (Fig. 7b depicts the results for S_1). Correspondingly, fitting linear regression models to the dependencies between corrected $\Delta B_{z,c}$ measurements and simulations reveals significant results for all subjects (Table 5), with the coefficients of determination being on average 0.68 and 0.88 for the R-L and A-P montages. Interestingly, the estimated slopes are slightly lower than unity. That is, the simulations underestimate $\Delta B_{z,c}$ slightly, but quite systematically in 9 out of the 10 measurements. It is worth noting that we do not expect identical results, as the simulations were based on a head model that employed standard conductivity values from literature.

Comparison of the current density measurements and simulations

We reconstructed the x- and y-components of the current density distribution in the imaging slice from the $\Delta B_{z,c}$ measurements (with and without stray field correction) and additionally from the simulated $\Delta B_{z,c}$ data in the five subjects for both R-L and A-P electrode montages. The results of the first subject are exemplarily shown in Figure 8a (Suppl. Fig. S3 lists the results of the other subjects). For the simulations, the reconstructed current densities $\vec{J}_{rec}$ differ markedly from the original current densities $\vec{J}_{FEM}$ that were determined via FEM calculations and served to calculate the $\Delta B_{z,c}$ distributions via the Biot-Savart Law. While coarse features of the current flow pattern such as generally higher current densities close to the electrodes and in the longitudinal fissure (for the A-P montage) are maintained, fine inflow effects in the sulci are mostly lost. Visual comparison of the current density reconstructions from the uncorrected versus corrected $\Delta B_{z,c}$ measurements reveals that the current densities close to the electrodes are overestimated when the $\Delta B_{z,c}$ data is not corrected for the cable-induced stray fields. In addition, increased current densities in the CSF-filled longitudinal fissure are only observable for the corrected case. Comparing the current density distributions reconstructed from the measurements versus the simulations by means of scatter plots (Fig. 8b) and linear regression analyses (Tables 6 and 7)

confirms that the difference between measurements and simulations is overestimated without stray field correction. Specifically, the slopes of the regression lines increase by on average 0.16 (uncorrected vs. corrected: 0.65 vs. 0.81, pooled across A-P and R-L). Also for the corrected data, the slopes are still lower than unity, i.e. the simulations systematically underestimate the current densities by on average 24%. The coefficients of determination are only slightly increased for the corrected data, for which they reach on average 0.71.

DISCUSSION AND CONCLUSIONS

We tested two MR sequences, MESE and SSFP-FID, for measurements of weak current-induced magnetic fields in the human brain. The sequences were previously optimized using extensive computer simulations and phantom tests (Göksu et al., 2017) to maximize their sensitivity to the current-induced fields. Here, we assessed their performance in-vivo and demonstrated that both sequence types could be successfully used to reveal the magnetic field distributions for a current strength of 1 mA, in turn allowing us to reconstruct the current flow distribution in the brain.

Optimization and validation of the MR sequences and measurement procedures

Our results demonstrated the need to adapt the employed sequences for in-vivo application by including multi-gradient-echo acquisitions. Specifically, long echo times (MESE) and repetitions times (SSFP-FID) are required to maximize the sensitivity of the measurements to the current-induced magnetic fields (Göksu et al., 2017). This in turn decreases their robustness to physiological noise (e.g., due to respiration, blood flow and small subject movement) when single-echo readouts with low bandwidths are used. Our results show that multi-gradient-echo readouts at higher bandwidths improve the image quality and allow selecting long echo and repetition times to maximize sensitivity, even though the total available readout period is slightly shortened by the time needed for the additional gradient switching in that case.

In contrast to the better efficiency of SSFP-FID compared to MESE observed in the prior phantom tests, both sequence types had similar noise levels in the in-vivo case when matching the total acquisition time. Specifically, comparing the average noise standard deviations listed for MESE (N_{GE}=5) in Table 1 to the results for SSFP-FID with T_R = 120 ms in Table 4 (both acquired with $T_{tot} \approx 9$ mins) reveals similar values. This indicates that physiological noise is a dominant factor that limits the sensitivity of the in-vivo measurements. In practice, the higher number of measurements that are obtained during SSFP-FID acquisitions open up a possibility of discarding (partial) measurements with strong noise, thereby possibly improving the quality of the final averaged magnetic field image. Nevertheless, MESE may still outperform SSFP-FID in multi-slice acquisition, as it allows for interleaved slice excitation without prolonging the total acquisition time (Göksu et al., 2017). The impact of physiological noise

also became apparent when testing different repetition times for the SSFP-FID measurements. As expected, increasing T_R from 40 ms to 80 ms increased the measurement sensitivity. However, an additional increase to 120 ms tended to decrease the sensitivity of the in-vivo results slightly again, in contrast to the theoretical and phantom results. This indicates that a T_R moderately below the theoretically optimal value can be chosen for in-vivo applications without losing sensitivity, while potentially improving robustness.

For both sequence types, the dependence of the measured magnetic field on the current strength exhibited a good linearity. In each of the three tested subjects, the slopes of the linear fits of the results obtained with the two sequences were similar. This validates the chosen scaling factor m_{seq} for the SSFP-FID measurements (Eq. 2), which relates the magnetic field and phase changes, and which was determined via spin simulations (Göksu et al., 2017).

We have demonstrated strong effects of the magnetic stray fields created by the current flow in the cables on the measured magnetic field and on the reconstructed current flow distributions, and have validated a correction method that employs delineations of the cable paths derived from structural images for forward calculations of the stray fields. While improved cable designs might help to ameliorate this problem, we would like to emphasize that even a small deviation from an ideal path parallel to the field direction of the scanner will cause non-negligible distortions of the measured field distributions when it occurs close to the measurement volume, e.g., 10 cm away. This effect results in miscalculated current flow distributions, and highlights the importance of controlling for and, if required, correcting the impact of the stray fields.

Comparison of measured and simulated fields

The measured magnetic fields showed a good correspondence to the fields obtained via FEM simulations, with average coefficient of determinations R^2 of 68% and 88% for R-L and A-P montages. Following up on the reasons why the A-P montage is on average revealing a better correspondence might be interesting for future studies. The simulations based on "standard" tissue conductivities taken from literature systematically underestimated the strength of the current-induced $\Delta B_{z,c}$ in 9 out of the 10 measurements (average regression slopes of 0.80 and 0.90 for R-L and A-P). Also the current density distributions estimated from the corrected magnetic field measurements and the FEM simulations were in good agreement, with an average coefficient of determination of R^2=71%, with little difference between the R-L and A-P montages. The simulations underestimated the current strength on average by 24%.

Interestingly, recent studies using invasive in-vivo recordings to measure the electric field injected by transcranial weak current stimulation indicate that FEM simulations based on standard conductivity values similar to the ones used here over- rather than underestimate the electric field strength (Huang et al., 2017; Opitz et al., 2016). This apparent contradiction might be resolved by considering that we reconstructed the current density rather than the electric field. Interestingly, Huang et al. (2017) derived

individually optimized ohmic conductivities to best fit the simulated to the measured electric fields, and found that optimization resulted in higher-than-standard tissue conductivities consistently across subjects. Increasing the conductivity of brain tissue would in turn tend to increase the current strength inside the skull, in line with our results. While this explanation seems plausible, it should be followed up, e.g. by future simulation work.

Prior Studies

To our knowledge, only two prior studies report in-vivo MR measurements of current-induced magnetic fields in the human brain. In (Jog et al., 2016), standard field mapping sequences were employed to measure the constant fields of direct currents. While the use of standard sequences has the advantage that 3D coverage can be readily achieved, this approach is not robust to slow temporal drifts of the MR signal that occur due to both technical and physiological reasons, inherently limiting the achievable sensitivity. The results presented in (Kasinadhuni et al., 2017) were based on a measurement approach that was more similar to the approach tested here. However, their method is comparably less sensitive to current-induced field changes and the results were not corrected for cable-induced stray fields. The spatial patterns of the measured magnetic field distributions reported in that study vary substantially across subjects, despite using the same electrode locations. The peak magnetic field values exceed those, which we obtained for the uncorrected images, and are consistently higher than those indicated by their and our FEM simulations. Even when considering that a higher current strength of 1.5 mA was applied, these observations indicate that cable-induced stray fields likely affected the results of that study. As current flow reconstruction algorithms employ spatial derivatives of the measured current-induced magnetic field (Ider et al., 2010; Park et al., 2007), any non-constant stray field will distort the reconstructed current flow. This opens the possibility that also the substantial differences between the measured and simulated current density reconstructions reported in (Kasinadhuni et al., 2017) might have been amplified by neglecting putative cable-induced stray fields.

Limitations and Future Work

The main focus of our study was on the optimization and validation of the MR sequences and measurement protocol. In the future, the measurement sensitivity can possibly be further increased by using pulse sequences such as balanced alternating steady-state free precession (bSSFP) which exhibits a more than 10 times higher phase sensitivity (Bieri et al., 2006; Minhas et al., 2010). A higher sensitivity would be beneficial to limit scan time when aiming to extend the spatial coverage towards multiple slices. Increasing the current strength from 1 mA up to 2 mA is also feasible, but requires careful piloting. Stronger currents also increase the side effects such as tickling and pain sensations underneath the electrodes, which makes the measurements less comfortable for the participants and might result in stronger head movement. It would also be desirable to optimize the cable design in order

to reduce the influence of the cable-induced stray fields, which might help to further increase the robustness of the final results.

In addition, the employed current density reconstruction can be further optimized. Replacing the median filter used to denoise the $\Delta B_{z,c}$ image before applying the reconstruction algorithm by more advanced filter approaches (Lee et al., 2011) might help to reveal some more detail in the reconstructed current density images. The reconstruction was based on the simplified assumption that the current flow is restricted to a 2D slice to account for the fact that only $\Delta B_{z,c}$ data of one slice was available. Combined with the imaging of multiple slices, reconstructing the current flow from 3D $\Delta B_{z,c}$ data should help to increase the accuracy of the reconstruction (Ider et al., 2010). However, it should be noted that these limitations do not affect our finding that the FEM simulations underestimated the current strength, as we applied the same reconstruction steps to the simulation results rather than using the originally simulated current distribution for comparison (Fig. 8a). Finally, it will be interesting to explore the usage of the measured $\Delta B_{z,c}$ data for the estimation of individual tissue conductivities (Kwon et al., 2016).

Conclusion

We have demonstrated the feasibility of reliable MRCDI measurements in-vivo in the human brain at a current strength of 1 mA. Future studies might aim to further improve the sensitivity of the MR methods and their robustness to physiological noise, as well as to extend their spatial coverage towards multiple slices. Our results are promising and indicate that MRCDI measurements combined with the reconstruction of current densities and tissue conductivities (Eyüboğlu, 2006c; Ider et al., 2010; Park et al., 2007; Seo et al., 2003; Seo and Woo, 2011b) might be useful for validating simulations based on volume conductor models of the head and for improving the accuracy of the simulations.

ACKNOWLEDGEMENTS

This study was supported by the Lundbeck foundation (grant R118-A11308 to AT and grant R59 A5399 to HR).

FIGURES

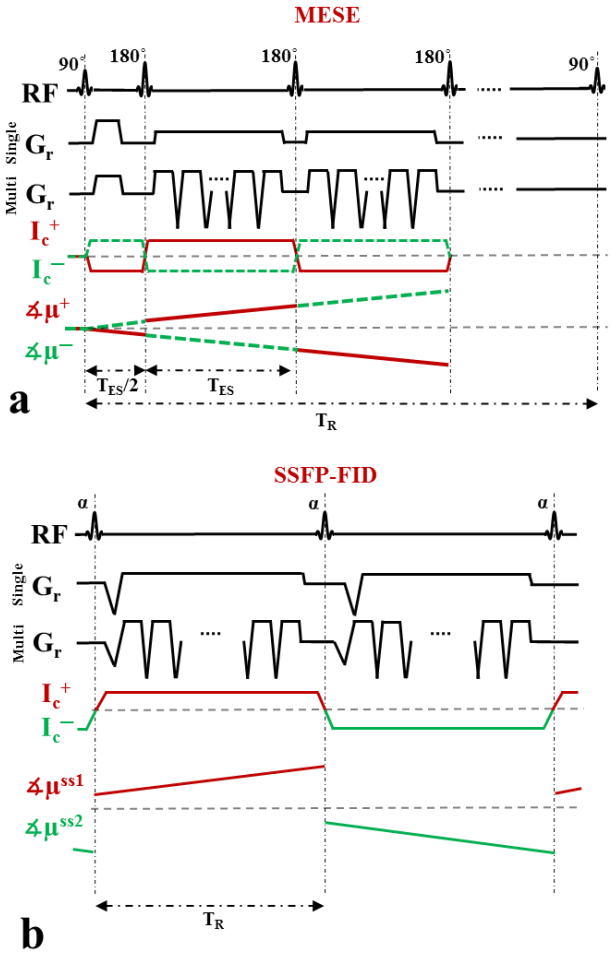

Figure 1. Schematic diagrams of the MESE and SSFP-FID sequences (please see Göksu et al., 2017 for details). (a) Diagram of the MESE sequence. The sequence is composed of a 90˚ excitation pulse preceding repetitive 180˚ refocusing pulses, so that multiple spin echoes are created. The injected bipolar current waveform is synchronized with the radio frequency (RF) pulses, so that the phase of the continuous complex transverse magnetization ($\measuredangle\mu$) increases linearly over time. The measurement is performed twice with opposite current injection profiles (indicated by red and green dashed lines), and the difference between the phase images is used to determine the current-induced magnetic field. Either single-gradient-echo readouts (single G_r) or multi-gradient-echo readouts with fly-back (multi G_r) are used. (b) Diagram of the SSFP-FID sequence. The sequence is composed of repetitive in-phase excitation pulses with constant tip angle and constant repetition time T_R. A bipolar current waveform is injected in synchrony with the SSFP-FID sequence. The current-induced phase of the continuous complex transverse magnetization evolves in opposite directions in odd and even T_R periods (indicated by red and green lines), which results in two different steady-state conditions with opposite phases. Either single-gradient-echo readouts (single G_r) or multi-gradient-echo readouts with fly-back (multi G_r) are used.

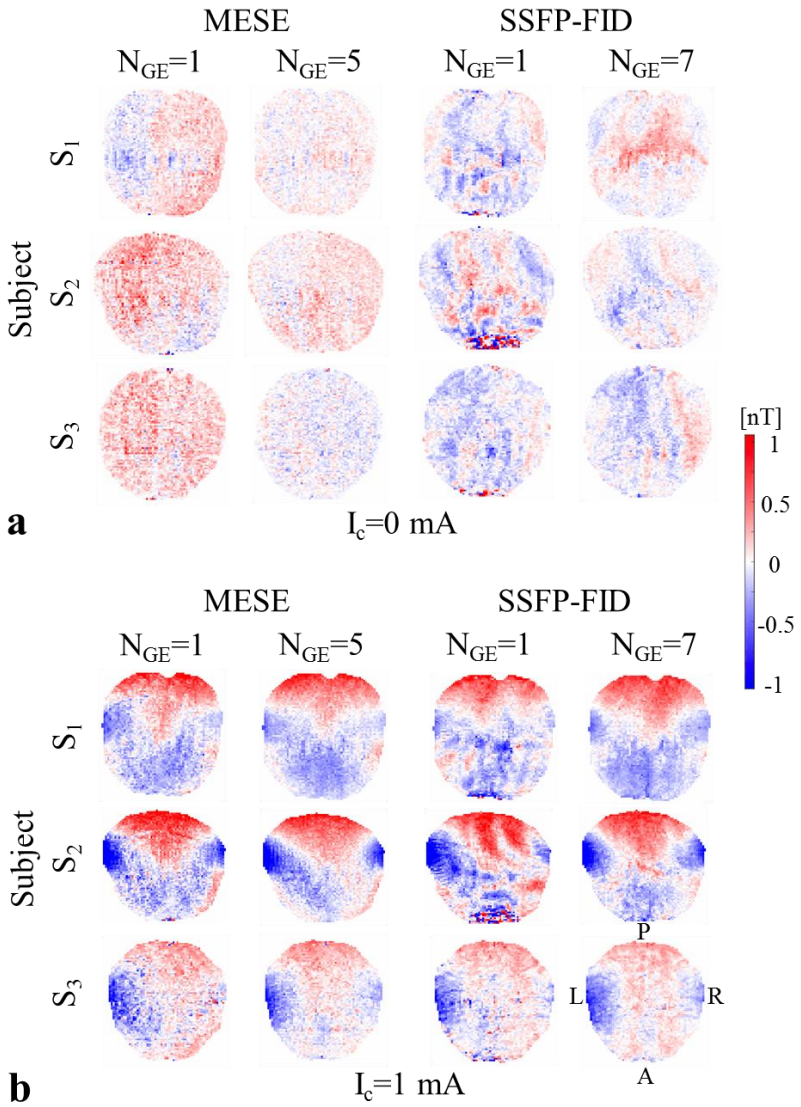

Figure 2. Experiment 1: Comparison of single- vs. multi-gradient-echo acquisition in three subjects. The T_{ES} (MESE) and T_R (SSFP-FID) times were kept identical between both cases. All images are shown in radiological convention, with the orientation indicated for the lower right slice in subfigure b. (a) $\Delta B_{z,c}$ images of the measurements without current injection. For both MESE and SSFP-FID (T_R=120 ms, N_{meas} = 12), the results of the multi-gradient-echo acquisitions exhibit a lower noise floor than those of the single-gradient-echo acquisitions. (b) $\Delta B_{z,c}$ images of the measurements with current injection. For better visualization of the spatial patterns, mean-corrected images are shown (i.e., the average $\Delta B_{z,c}$ in the brain was subtracted). The quality of the images is improved by the use of multi-gradient-echo readouts, which prevent the ghosting-like patterns observed in the results of the single-gradient-echo acquisitions. Please note that the total acquisition times differed for MESE ($T_{tot} \approx 9$ mins) and SSFP-FID ($T_{tot} \approx 4.5$ mins) in this experiment, as the primary goal was to compare single- versus multi-gradient-echo readouts.

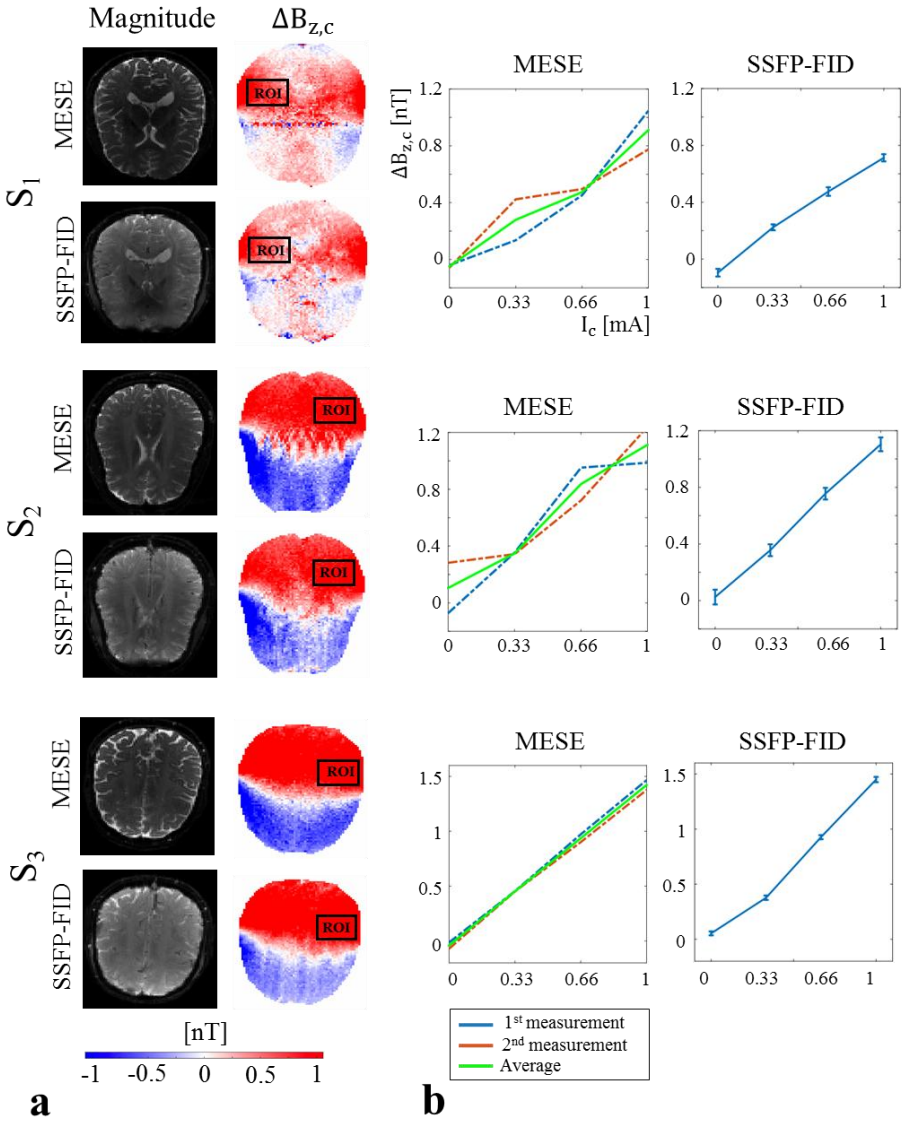

Figure 3. Experiment 2: Test of the linear dependence of the measured $\Delta B_{z,c}$ on the applied current strength in three subjects, performed for both MESE and SSFP-FID (T_R=120 ms, N_{meas} = 12) with multi-gradient-echo readouts. (a) Magnitude and $\Delta B_{z,c}$ images for the measurements at I_c = 1 mA. The black rectangles depict the regions-of-interest (ROIs), in which the average $\Delta B_{z,c}$ was extracted. In subject S_1, a line-like artifact is visible in the MESE $\Delta B_{z,c}$ images in the phase encoding direction and to a lesser extent also in the SSFP-FID results. The artifact is consistent with flow effects from vessels. We did not observe this type of artifact again. (b) Dependency of the average $\Delta B_{z,c}$ in the ROI on the applied current strength. For MESE, the results of the two measurements are shown as blue and orange lines, and their average is shown as a green line. For SSFP-FID, the average of the 12 measurements is shown; the bars represent the standard error.

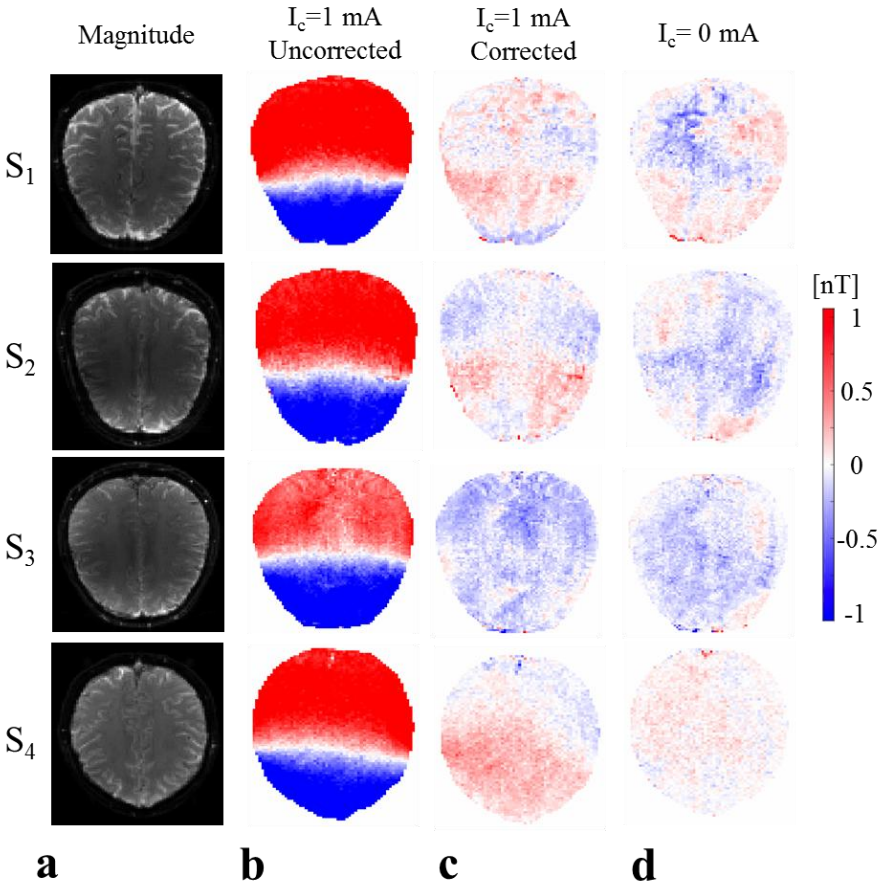

Figure 4. Experiment 3: Correction of the cable-induced magnetic stray fields for SSFP-FID measurements (T_R=120 ms, N_{meas}= 24) with multi-gradient-echo readouts in four subjects (no tissue current). The experiments were repeated twice, and the figure shows the results of the first experimental run. (a) Magnitude images. (b) Uncorrected $\Delta B_{z,c}$ images showing the stray field generated by the current flow in the wire loop around the head. (c) Corrected $\Delta B_{z,c}$ images, in which the stray field was calculated based on the reconstructed wire path and subtracted from the measured $\Delta B_{z,c}$. (d) $\Delta B_{z,c}$ images of the control measurements performed without current injection.

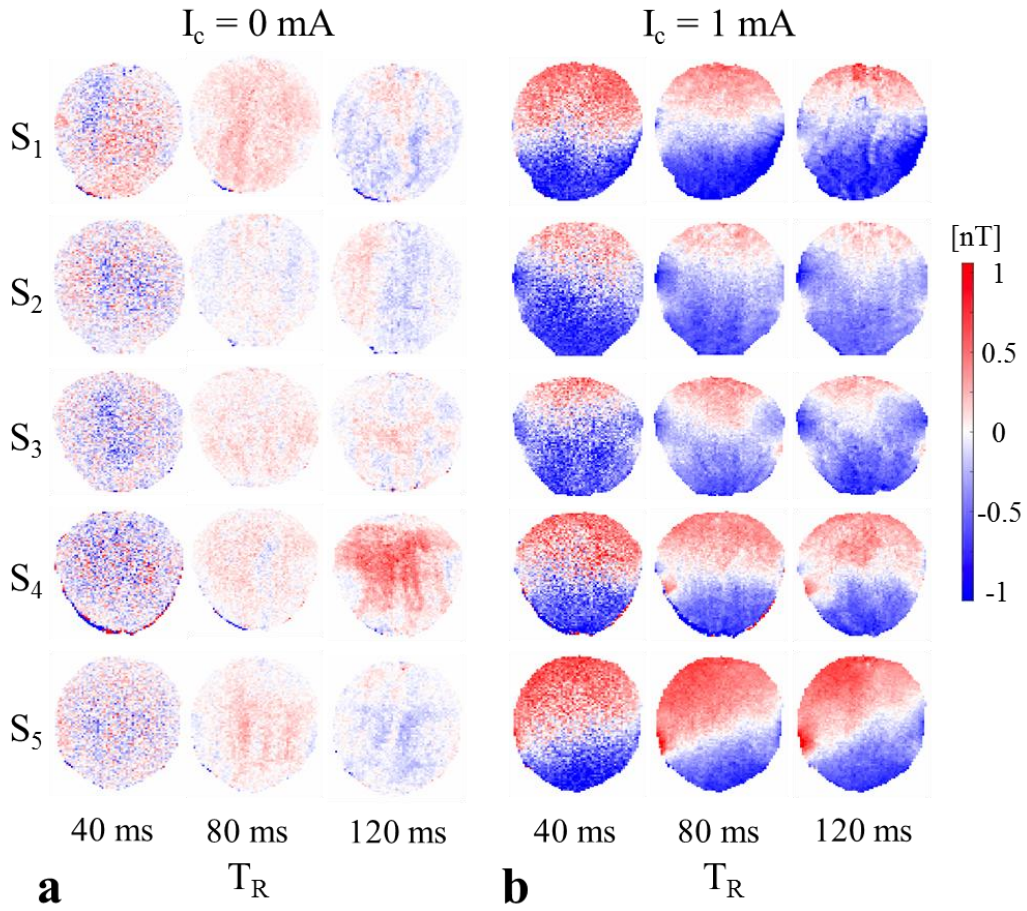

Figure 5. Experiment 4: Comparison of SSFP-FID measurements with multi-gradient-echo readouts performed in five subjects using three different repetition times T_R. (a) $\Delta B_{z,c}$ images of the experiments performed without current injection. (b) $\Delta B_{z,c}$ images of the experiments with current injection. The experiments using T_R = 40 ms exhibit the highest noise levels. The total acquisition time was kept the same for the three repetition times by adapting the number of measurements (T_R=40 ms: N_{meas}= 72; T_R=80 ms: N_{meas}= 36; T_R=120 ms: N_{meas}= 24).

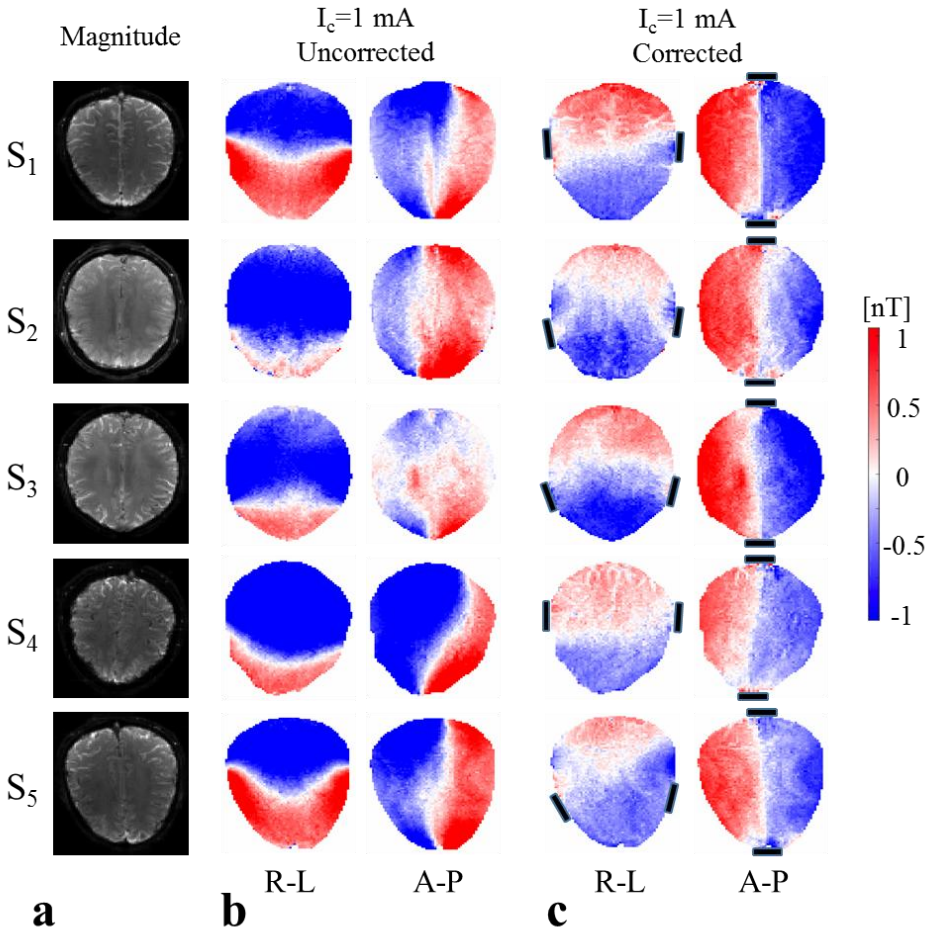

Figure 6. Experiment 5: SSFP-FID measurements (T_R=120 ms, N_{meas}= 24) with multi-gradient-echo readouts of five subjects for the R-L and A-P electrode montages. (a) Magnitude images. (b) Uncorrected $\Delta B_{z,c}$ images (left column: R-L montage; right column: A-P montage). (c) Corrected $\Delta B_{z,c}$ images. The electrode positions are indicated as black boxes. Note that cable contributions dominate the uncorrected images.

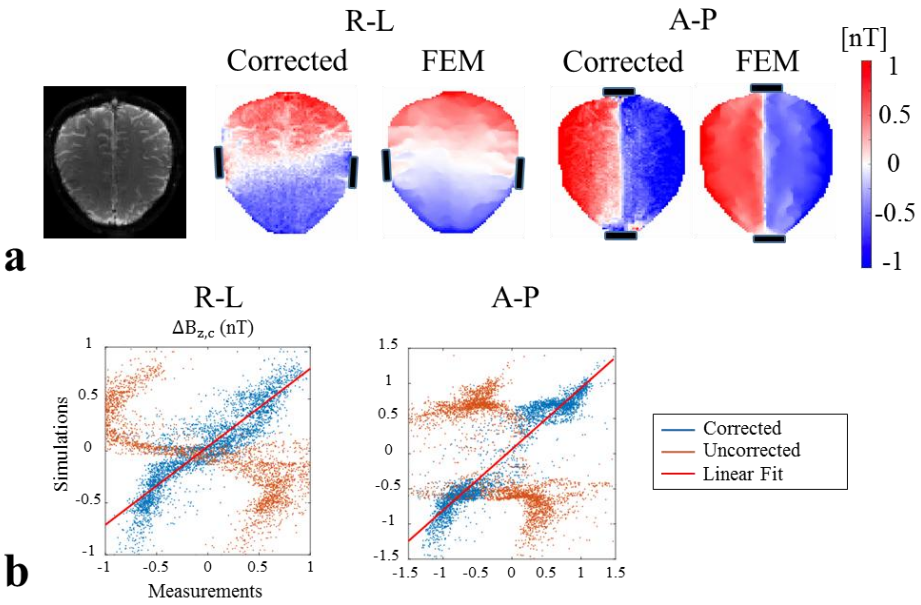

Figure 7. Experiment 5: (a) SSFP-FID measurements and FEM simulations of the current-induced $\Delta B_{z,c}$ for subject S1 in Fig. 6. Shown are the MR magnitude image, and the corrected $\Delta B_{z,c}$ images and FEM results for the both the R-L and A-P montages. The electrode positions are shown as black rectangles. (b) Scatter plots of the $\Delta B_{z,c}$ measurements versus simulations (left column: R-L montage; right column: A-P montage). The results are plotted for the cases with (blue) and without (orange) cable-induced $\Delta B_{z,c}$ correction. The results without stray field correction have no correspondence to the simulations. The red regression lines are based on a linear regression of the corrected $\Delta B_{z,c}$ measurement results versus the simulations (please refer to Table 5 for the results of the regression analyses for all five subjects).

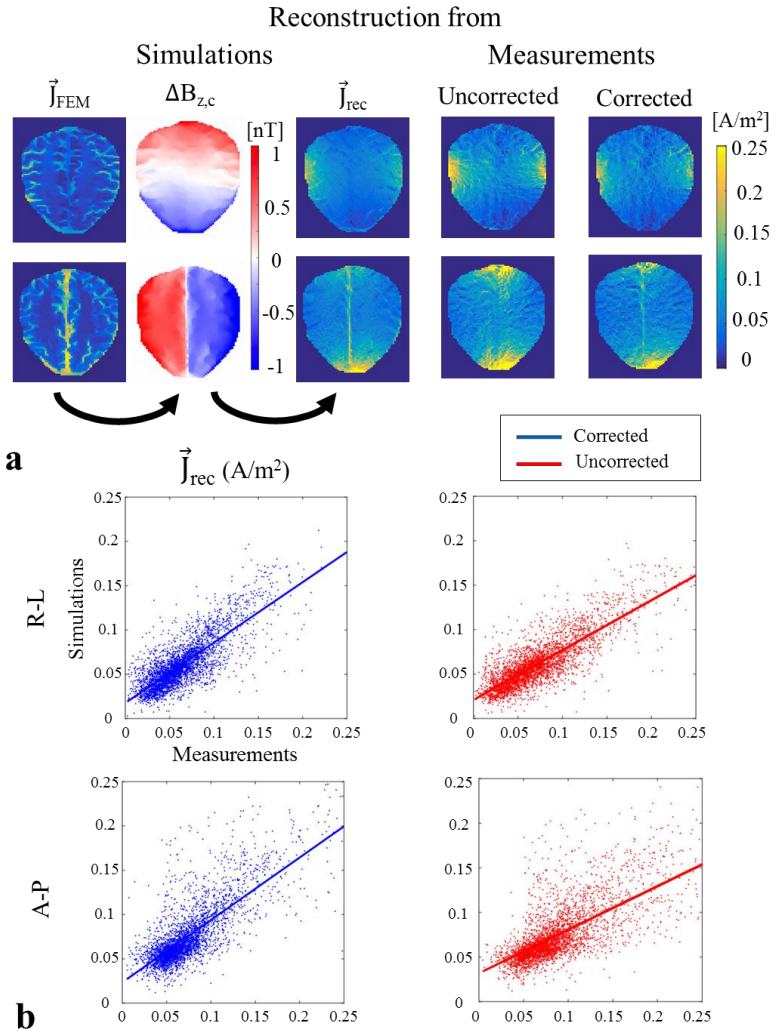

Figure 8. Experiment 5: (a) Reconstruction of the current density distributions from simulated and measured $\Delta B_{z,c}$ images. The results for subject S_1 are exemplarily shown (upper row: R-L montage; second row: A-P montage). The norm of the 2D current densities is depicted. Visual comparison of the simulated current density distributions $\vec{J}_{FEM}$ with their corresponding $\vec{J}_{rec}$ images that were reconstructed from the simulated $\Delta B_{z,c}$ images shows that the reconstruction algorithm recovers only the coarse features of the current flow pattern. Specifically, higher current densities close to the electrodes and in the longitudinal fissure are maintained. Visual comparison of the reconstructions from uncorrected and corrected $\Delta B_{z,c}$ measurements reveals that the reconstructions from the uncorrected measurements overestimate the current densities close to the electrodes. For the A-P montage, an increased current flow in the longitudinal fissure is only visible for the corrected measurements. (b) Scatter plots of the projected current flow measurements versus simulations for subject S_1 (1st row: R-L montage; 2nd row: A-P montage). The results are plotted for the cases with (blue) and without (red) cable-induced stray magnetic field correction. The results without stray field correction overestimate the current flow density, resulting in a smaller slope of the fitted regression line (please refer to Table 6 for the results of the regression analyses for all five subjects).

TABLES

	MESE		SSFP-FID	
	N_{GE}=1 $\mu_{\Delta Bz,c}$ ($\sigma_{\Delta Bz,c}$)	**N_{GE}=5**	**N_{GE}=1**	**N_{GE}=7**
S_1	0.066 (0.166)	0.037 (0.086)	-0.043 (0.149)	0.026 (0.123)
S_2	0.126 (0.186)	0.089 (0.117)	-0.024 (0.201)	-0.012 (0.111)
S_3	0.144 (0.150)	-0.035 (0.103)	-0.078 (0.150)	-0.041 (0.151)
Avg	**0.112 (0.167)**	**0.030 (0.102)**	**-0.048 (0.167)**	**-0.009 (0.128)**

Table 1. Experiment 1: Comparison of single- vs. multi-gradient-echo acquisition for the case without current injection in three subjects. The table lists the mean shifts $\mu_{\Delta Bz,c}$ and standard deviations $\sigma_{\Delta Bz,c}$ (given in brackets) of the noise distributions of $\Delta B_{z,c}$ values in the brain. The last row lists the average $\mu_{\Delta Bz,c}$ and average $\sigma_{\Delta Bz,c}$ values across subjects. The units are in nT. For both MESE and SSFP-FID, the multi-gradient-echo acquisitions have lower mean shifts and standard deviations.

	MESE			SSFP-FID		
	$F_{1,6}$ (p)	**β_0** in [nT]	**β_1** in [nT/mA]	**$F_{1,46}$ (p)**	**β_0** in [nT]	**β_1** in [nT/mA]
S_1	57 ($<0.3\cdot10^{-3}$)	-0.05 (0.08)	0.90 (0.12)	46 ($<10^{-6}$)	-0.07 (0.07)	0.80 (0.12)
S_2	50 ($<0.4\cdot10^{-3}$)	0.07 (0.09)	1.03 (0.15)	27 ($<10^{-5}$)	0.02 (0.13)	1.09 (0.21)
S_3	1527 ($<10^{-6}$)	-0.04 (0.02)	1.44 (0.04)	225 ($<10^{-6}$)	-0.01 (0.06)	1.42 (0.10)

Table 2. Experiment 2: Linear fits of the measured dependence of $\Delta B_{z,c}$ on the applied current strength. The table lists the F- and p-values, the intercepts β_0 and the slopes β_1 of the fitted linear regression models. The standard errors of β_0 and β_1 are given in brackets.

	1st Experiment		2nd Experiment	
	I_c=0 mA $\mu_{\Delta Bz,c}$ ($\sigma_{\Delta Bz,c}$)	**I_c=1 mA, corrected**	**I_c=0 mA**	**I_c=1 mA, corrected**
S_1	0.013 (0.136)	0.049 (0.138)	0.016 (0.095)	-0.011 (0.194)
S_2	-0.067 (0.120)	-0.012 (0.148)	-0.022 (0.091)	0.012 (0.133)
S_3	-0.110 (0.110)	-0.169 (0.130)	0.011 (0.108)	-0.018 (0.129)
S_4	0.031 (0.072)	0.110 (0.170)	0.103 (0.096)	-0.080 (0.125)
Avg	**-0.033 (0.110)**	**-0.006 (0.147)**	**0.027 (0.098)**	**-0.024 (0.145)**

Table 3. Experiment 3: Correction of the cable-induced magnetic stray field for SSFP-FID measurements in four subjects. The experiment was repeated twice. The table lists the mean shifts $\mu_{\Delta Bz,c}$ and standard deviations $\sigma_{\Delta Bz,c}$ (given in brackets) of the distribution of $\Delta B_{z,c}$ in the brain. The last row lists the average $\mu_{\Delta Bz,c}$ and average $\sigma_{\Delta Bz,c}$ values across subjects. The units are in nT. Correcting the stray field induced by the wire loop around the head results in noise distributions, which are similar to those of the control measurements without current injection.

	T_R = 40 ms $\mu_{\Delta Bz,c}$ ($\sigma_{\Delta Bz,c}$)	**T_R = 80 ms**	**T_R = 120 ms**
S_1	0.039 (0.202)	0.115 (0.092)	-0.046 (0.111)
S_2	-0.012 (0.191)	-0.007 (0.073)	-0.026 (0.095)
S_3	-0.045 (0.212)	0.053 (0.076)	0.011 (0.090)
S_4	-0.042 (0.259)	0.049 (0.084)	0.179 (0.210)
S_5	-0.002 (0.192)	-0.052 (0.091)	0.038 (0.084)
Avg	**-0.012 (0.211)**	**0.031 (0.083)**	**0.031 (0.100)**

Table 4. Experiment 4: Comparison of SSFP-FID measurements performed in five subjects without current injection for three different repetition times T_R. The table lists the mean shifts $\mu_{\Delta Bz,c}$ and standard deviations $\sigma_{\Delta Bz,c}$ (given in brackets) of the noise distributions of $\Delta B_{z,c}$ in the brain. The last row lists the average $\mu_{\Delta Bz,c}$ and average $\sigma_{\Delta Bz,c}$ values across subjects. The units are in nT. Both the measurements at T_R = 80 ms and 120 ms exhibit lower noise standard deviations than the measurements at T_R = 40 ms.

	R-L			A-P		
	β_0 in [nT]	β_1	R^2	β_0 in [nT]	β_1	R^2
S_1	0.18 ±0.002	0.81 ±0.12	0.87	0.04 ±0.003	0.80 ±0.004	0.91
S_2	0.04 ±0.003	0.75 ±0.15	0.80	0.06 ±0.004	0.87 ±0.005	0.90
S_3	-0.06 ±0.003	0.71 ±0.04	0.59	0.08 ±0.004	1.04 ±0.008	0.84
S_4	0.30 ±0.005	0.97 ±0.01	0.69	-0.14 ±0.003	0.84 ±0.005	0.89
S_5	0.10 ±0.006	0.77 ±0.02	0.44	-0.01 ±0.003	0.94 ±0.006	0.87
Avg ±SE	**0.11 ±0.06**	**0.80 ±0.05**	**0.68 ±0.08**	**0.01 ±0.04**	**0.90 ±0.04**	**0.88 ±0.01**

Table 5. Experiment 5: Linear fits of the $\Delta B_{z,c}$ measurements and simulations across five different subjects for the two current injection profiles (R-L and A-P). The table lists the intercepts β_0, the slopes β_1, and the coefficient of determination R^2 of the fitted linear regression models. For β_0 and β_1, also the standard errors are stated. The last row lists the averages across subjects, and the standard error of the averages. Most estimated slopes are lower than unity (i.e., the simulations slightly underestimate the $\Delta B_{z,c}$). The significance of the regression models was confirmed using F-tests, with the results being highly significant ($p<10^{-6}$) in all cases.

	R-L					
	Uncorrected			Corrected		
	β_0 in [A/m^2]	β_1	R^2	β_0 in [A/m^2]	β_1	R^2
S_1	0.021 $\pm$0.001	0.56 $\pm 6.4 \cdot 10^{-3}$	0.68	0.018 $\pm$0.001	0.68 $\pm 8.7 \cdot 10^{-3}$	0.63
S_2	0.016 $\pm$0.001	0.71 $\pm 6.6 \cdot 10^{-3}$	0.75	0.014 $\pm$0.001	0.78 $\pm 7.5 \cdot 10^{-3}$	0.74
S_3	0.016 $\pm$0.001	0.69 $\pm 7.4 \cdot 10^{-3}$	0.73	0.007 $\pm$0.001	0.89 $\pm 8.9 \cdot 10^{-3}$	0.76
S_4	0.018 $\pm$0.001	0.61 $\pm 10.7 \cdot 10^{-3}$	0.53	0.014 $\pm$0.001	0.74 $\pm 9.2 \cdot 10^{-3}$	0.69
S_5	0.019 $\pm$0.001	0.65 $\pm 6.8 \cdot 10^{-3}$	0.74	0.011 $\pm$0.001	0.80 $\pm 7.4 \cdot 10^{-3}$	0.79
Avg $\pm$SE	**0.018 $\pm$0.001**	**0.64 $\pm$0.03**	**0.69 $\pm$0.04**	**0.013 $\pm$0.002**	**0.78 $\pm$0.03**	**0.72 $\pm$0.03**

Table 6. Experiment 5: Linear fits of the current density distributions reconstructed from measurements and simulations. Listed are the results for the current injection profile R-L, for both the cases with and without stray magnetic field correction. The table lists the intercepts β_0, the slopes β_1, and the coefficient of determination R^2 of the fitted linear regression models. For β_0 and β_1, also the standard errors are stated. The last row lists the averages across subjects, and the standard error of the averages. The estimated slopes increase on average by 0.14 for the corrected vs. uncorrected case. Also for the corrected case, the estimated slopes are still lower than unity (i.e., the simulations underestimate the current density). The significance of the regression models was confirmed using F-tests, with the results being highly significant ($p<10^{-6}$) in all cases.

	A-P					
	Uncorrected			Corrected		
	β_0 in [A/m^2]	β_1	R^2	β_0 in [A/m^2]	β_1	R^2
S_1	0.032 $\pm$0.001	0.49 $\pm 7.4\cdot10^{-3}$	0.55	0.023 $\pm$0.001	0.71 $\pm 9.2\cdot10^{-3}$	0.62
S_2	0.022 $\pm$0.001	0.67 $\pm 6.4\cdot10^{-3}$	0.74	0.015 $\pm$0.001	0.84 $\pm 7.9\cdot10^{-3}$	0.75
S_3	0.022 $\pm$0.001	0.70 $\pm 9.0\cdot10^{-3}$	0.65	0.014 $\pm$0.001	0.83 $\pm 10.8\cdot10^{-3}$	0.65
S_4	0.023 $\pm$0.001	0.79 $\pm 10.2\cdot10^{-3}$	0.68	0.009 $\pm$0.001	0.84 $\pm 10.2\cdot10^{-3}$	0.71
S_5	0.018 $\pm$0.001	0.67 $\pm 6.5\cdot10^{-3}$	0.77	0.010 $\pm$0.001	0.91 $\pm 7.6\cdot10^{-3}$	0.82
Avg $\pm$SE	**0.023 $\pm$0.002**	**0.66 $\pm$0.05**	**0.68 $\pm$0.04**	**0.014 $\pm$0.003**	**0.83 $\pm$0.03**	**0.71 $\pm$0.04**

Table 7. Experiment 5: Linear fits of the current density distributions reconstructed from measurements and simulations. Listed are the results for the current injection profile A-P. The estimated slopes increase on average by 0.16 for the corrected vs. uncorrected case. The estimated slopes are still lower than unity also for the corrected case (i.e., the simulations underestimates the current density). This is similar to the results observed for current injection profile R-L. The significance of the regression models was confirmed using F-tests, with the results being highly significant ($p<10^{-6}$) in all cases.

References

Bieri, O., Maderwald, S., Ladd, M.E., Scheffler, K., 2006. Balanced alternating steady-state elastography. Magn. Reson. Med. 55, 233–41.

Birgül, Ö., Eyüboğlu, B.M., Ider, Y.Z., 2003. Experimental results for 2D magnetic resonance electrical impedance tomography (MR-EIT) using magnetic flux density in one direction. Phys. Med. Biol. 48, 3485–3504.

Dabek, J., Kalogianni, K., Rotgans, E., van der Helm, F.C.T., Kwakkel, G., van Wegen, E.E.H., Daffertshofer, A., de Munck, J.C., 2016. Determination of head conductivity frequency response in vivo with optimized EIT-EEG. Neuroimage 127, 484–495. doi:10.1016/j.neuroimage.2015.11.023

Eyüboğlu, B.M., 2006a. Electrical Impedance Imaging, Injected Current, in: Wiley Encyclopedia of Biomedical Engineering. pp. 1195–1205.

Eyüboğlu, B.M., 2006b. Magnetic Resonance Current Density Imaging, in: Wiley Encyclopedia of Biomedical Engineering. pp. 2147–53.

Eyüboğlu, B.M., 2006c. Magnetic Resonance-Electrical Impedance Tomography, in: Wiley Encyclopedia of Biomedical Engineering. pp. 2154–62.

Faes, T.J.C., Meij, H.A. van der, Munck, J.C. de, Heethaar, R.M., 1999. The electric resistivity of human tissues (100 Hz-10 MHz): a meta-analysis of review studies. Physiol. Meas. 20, R1–R10. doi:10.1088/0967-3334/20/4/201

Göksu, C., Sadighi, M., Eroğlu, H.H., Eyüboğlu, M., 2014. Realization of Magnetic Resonance Current Density Imaging at 3 Tesla, in: Annual International Conference of the IEEE Engineering in Medicine and Biology Society - EMBC. pp. 1115–1118.

Göksu, C., Scheffler, K., Ehses, P., Hanson, L.G., Thielscher, A., 2017. Sensitivity Analysis of Magnetic Field Measurements for Magnetic Resonance Electrical Impedance Tomography (MREIT). Magn. Reson. Med. 0. doi:10.1002/mrm.26727

Haase, A., Frahm, J., Hänicke, W., Matthaei, D., 1985. 1H NMR chemical shift selective (CHESS) imaging. Phys. Med. Biol. 30, 341–344.

Han, Y.Q., Meng, Z.J., Jeong, W.C., Kim, Y.T., Minhas, A.S., Kim, H.J., Nam, H.S., Kwon, O., Woo, E.J., 2010. MREIT conductivity imaging of canine head using multi-echo pulse sequence. J. Phys. Conf. Ser. 224, 12078. doi:10.1088/1742-6596/224/1/012078

Huang, Y., Liu, A.A., Lafon, B., Friedman, D., Dayan, M., Wang, X., Bikson, M., Doyle, W.K., Devinsky, O., Parra, L.C., 2017. Measurements and models of electric fields in the in vivo human brain during transcranial electric stimulation. Elife 6, e18834. doi:10.7554/eLife.18834

Ida, M., Wakayama, T., Nielsen, M.L., Abe, T., Grodzki, D.M., 2015. Quiet T1-Weighted Imaging Using PETRA : Initial Clinical Evaluation in Intracranial Tumor Patients. J. Magn. Reson. Imaging 41, 447–453. doi:10.1002/jmri.24575

Ider, Y.Z., Birgül, Ö., 1998. Use of the magnetic field generated by the internal distribution of injected currents for Electrical Impedance Tomography (MR-EIT). ELEKTRİK 6, 215–225.

Ider, Y.Z., Birgül, Ö., Oran, Ö.F., Arıkan, O., Hamamura, M.J., Müftüler, T., 2010. Fourier transform magnetic resonance current density imaging (FT-MRCDI) from one component of magnetic flux density. Phys. Med. Biol. 55, 3177–3199. doi:10.1088/0031-9155/55/11/013

Jaynes, E.T., 1955. Matrix treatment of nuclear induction. Phys. Rev. 98, 1099–1105.

Jeon, K., Minhas, A.S., Kim, Y.T., Jeong, W.C., Kim, H.J., Kang, B.T., Park, H.M., Lee, C.-O., Seo, J.K., Woo, E.J., 2009. MREIT conductivity imaging of the postmortem canine abdomen using CoReHA. Physiol. Meas. 30, 957–66. doi:10.1088/0967-3334/30/9/007

Jeong, W.C., Kim, Y.T., Minhas, a S., Lee, T.H., Kim, H.J., Nam, H.S., Kwon, O., Woo, E.J., 2010. In vivo conductivity imaging of human knee using 3 mA injection current in MREIT. J. Phys. Conf. Ser. 224, 12148. doi:10.1088/1742-6596/224/1/012148

Jog, M. V, Smith, R.X., Jann, K., Dunn, W., Lafon, B., Truong, D., Wu, A., Parra, L., Bikson, M., Wang, D.J.J., 2016. In-vivo Imaging of Magnetic Fields Induced by Transcranial Direct Current Stimulation (tDCS) in Human Brain using MRI. Sci. Rep. 6, 34385. doi:10.1038/srep34385

Joy, M.L.G., 2004. MR current density and conductivity imaging: the state of the art., in: Conf Proc IEEE Eng Med Biol Soc. pp. 5315–9. doi:10.1109/IEMBS.2004.1404484

Kasinadhuni, A.K., Indahlastari, A., Chauhan, M., Scär, M., Mareci, T.H., Sadleir, R.J., 2017. Imaging of current flow in the human head during transcranial electrical therapy. Brain Stimul. 10, 764–772. doi:10.1016/j.brs.2017.04.125

Kim, H.J., Kim, Y.T., Minhas, A.S., Jeong, W.C., Woo, E.J., 2009. In Vivo High-Resolution Conductivity Imaging of the Human Leg Using MREIT : The First Human Experiment 28, 1681–1687.

Kim, H.J., Oh, T.I., Kim, Y.T., Lee, B. Il, Woo, E.J., Seo, J.K., Lee, S.Y., Kwon, O., Park, C., Kang, B.T., Park, H.M., 2008. In vivo electrical conductivity imaging of a canine brain using a 3 T MREIT system. Physiol. Meas. 29, 1145–55. doi:10.1088/0967-3334/29/10/001

Kim, Y.T., Minhas, A.S., Meng, Z., Kim, H.J., Woo, E.J., 2011. Conductivity imaging of human lower extremity using MREIT with multi-echo pulse sequence and 3 mA imaging current. 2011 8th Int. Symp. Noninvasive Funct. Source Imaging Brain Hear. 2011 8th Int. Conf. Bioelectromagn. 48–52. doi:10.1109/NFSI.2011.5936818

Lee, C., Jeon, K., Ahn, S., Kim, H.J., Woo, E.J., Member, S., 2011. Ramp-Preserving Denoising for Conductivity Image Reconstruction in Magnetic Resonance Electrical Impedance Tomography 58, 2038–2050.

Lee, H., Jeong, W.C., Kim, H.J., Woo, E.J., Park, J., 2016. Alternating steady state free precession for estimation of current-induced magnetic flux density: A feasibility study. Magn. Reson. Med. 75, 2009–2019.

Meng, Z., Sajib, S.Z., Chauhan, M., Jeong, W.C., Kim, Y.T., Kim, H.J., Woo, E.J., 2012. Improved conductivity image of human lower extremity using MREIT with chemical shift artifact correction. Biomed. Eng. Lett. 2, 62–68. doi:10.1007/s13534-012-0052-0

Minhas, A.S., Woo, E.J., Sadleir, R., 2010. Simulation of MREIT using balanced steady state free precession (b-SSFP) pulse sequence. J. Phys. Conf. Ser. 224, 12019. doi:10.1088/1742-6596/224/1/012019

Miranda, P.C., 2013. Physics of effects of transcranial brain stimulation. Handb Clin Neurol 116, 353–366.

Mosher, J.C., Leahy, R.M., Lewis, P.S., 1999. EEG and MEG: Forward Solutions for Inverse Methods. IEEE Trans. Biomed. Eng. 46, 245–259.

Nam, H.S., Kwon, O.I., 2010. Optimization of multiply acquired magnetic flux density B(z) using ICNE-Multiecho train in MREIT. Phys. Med. Biol. 55, 2743–59.

Nitsche, M.A., Paulus, W., 2000. Excitability changes induced in the human motor cortex by weak transcranial direct current stimulation. J. Physiol. 527, 633–639.

Oh, S.H., Lee, B. Il, Woo, E.J., Lee, S.Y., Cho, M.H., Kwon, O., Seo, J.K., 2003. Conductivity and current density image reconstruction using harmonic Bz algorithm in magnetic resonance electrical impedance tomography. Phys. Med. Biol. 48, 3101–3116. doi:10.1088/0031-9155/48/19/001

Oh, S.H., Lee, B. Il, Woo, E.J., Lee, S.Y., Kim, T.-S., Kwon, O., Seo, J.K., 2005. Electrical

conductivity images of biological tissue phantoms in MREIT. Physiol. Meas. 26, S279-88. doi:10.1088/0967-3334/26/2/026

Oostenveld, R., Fries, P., Maris, E., Schoffelen, J.M., 2011. FieldTrip: Open source software for advanced analysis of MEG, EEG, and invasive electrophysiological data. Comput. Intell. Neurosci. 2011. doi:10.1155/2011/156869

Opitz, A., Falchier, A., Yan, C.-G., Yeagle, E.M., Linn, G.S., Megevand, P., Thielscher, A., Deborah A., R., Milham, M.P., Mehta, A.D., Schroeder, C.E., 2016. Spatiotemporal structure of intracranial electric fields induced by transcranial electric stimulation in humans and nonhuman primates. Sci. Rep. 6, 31236. doi:10.1038/srep31236

Park, C., Lee, B. Il, Kwon, O.I., 2007. Analysis of recoverable current from one component of magnetic flux density in MREIT and MRCDI. Phys. Med. Biol. 52, 3001–13. doi:10.1088/0031-9155/52/11/005

Sadighi, M., Göksu, C., Eyüboğlu, B.M., 2014. J-based Magnetic Resonance Conductivity Tensor Imaging (MRCTI) at 3 T. Annu. Int. Conf. IEEE Eng. Med. Biol. Soc. - EMBC 1139–1142.

Sadleir, R.J., Grant, S.C., Silver, X., Zhang, S.U., Woo, E.J., Lee, S.Y., Kim, T.S., Oh, S.H., Lee, B.I., Seo, J.K., 2005. Magnetic Resonance Electrical Impedance Tomography (MREIT) at 11 Tesla Field Strength : Preliminary Experimental Study 7, 340–343.

Saturnino, G.B., Antunes, A., Thielscher, A., 2015. On the importance of electrode parameters for shaping electric field patterns generated by tDCS. Neuroimage 120, 25–35. doi:10.1016/j.neuroimage.2015.06.067

Scheffler, K., Maderwald, S., Ladd, M.E., Bieri, O., 2006. Oscillating steady states. Magn. Reson. Med. 55, 598–603.

Scott, G.C., Joy, M.L.G., Armstrong, R.L., Henkelman, R.M., 1992. Sensitivity of magnetic-resonance current-density imaging. J. Magn. Reson. 97, 235–254.

Scott, G.C., Joy, M.L.G., Armstrong, R.L., Henkelman, R.M., 1991. Measurement of nonuniform current density by magnetic resonance. IEEE Trans. Med. Imaging 10, 362–374.

Seo, J.K., Woo, E.J., 2011a. Magnetic Resonance Electrical Impedance Tomography. Soc. Ind. Appl. Math. 53, 40–68.

Seo, J.K., Woo, E.J., 2011b. Magnetic Resonance Electrical Impedance Tomography (MREIT). Soc. Ind. Appl. Math. 53, 40–68.

Seo, J.K., Yoon, J., Woo, E.J., Kwon, O., 2003. Reconstruction of Conductivity and Current Density Images Using Only One Component of Magnetic Field Measurements. IEEE Trans. Biomed. Eng. 50, 1121–1124.

Tadel, F., Baillet, S., Mosher, J.C., Pantazis, D., Leahy, R.M., 2011. Brainstorm: A User-Friendly Application for MEG/EEG Analysis. Comput. Intell. Neurosci. 2011, 1–13. doi:10.1155/2011/879716

Thielscher, A., Antunes, A., Saturnino, G.B., 2015. Field modeling for transcranial magnetic stimulation: A useful tool to understand the physiological effects of TMS? Proc. Annu. Int. Conf. IEEE Eng. Med. Biol. Soc. EMBS 2015–Novem, 222–225. doi:10.1109/EMBC.2015.7318340

Thielscher, A., Antunes, A., Saturnino, G.B., 2015. Field modeling for transcranial magnetic stimulation: a useful tool to understand the physiological effects of TMS? Annu. Int. Conf. IEEE Eng. Med. Biol. Soc. 2015. doi:10.1109/EMBC.2015.7318340

Utz, K.S., Dimova, V., Oppenländer, K., Kerkhoff, G., 2010. Electrified minds: Transcranial direct current stimulation (tDCS) and Galvanic Vestibular Stimulation (GVS) as methods of non-invasive brain stimulation in neuropsychology-A review of current data and future implications.

Neuropsychologia 48, 2789–2810.

Walsh, D.O., Gmitro, A.F., Marcellin, M.W., 2000. Adaptive reconstruction of phased array MR imagery. Magn. Reson. Med. 43, 682–690.

Woo, E.J., Lee, S.Y., Mun, C.W., 1994. Impedance Tomography Using Internal Current Density Distribution Measured by Nuclear Magnetic Resonance. SPIE 2299, 377–385.

Woo, E.J., Seo, J.K., 2008. Magnetic resonance electrical impedance tomography (MREIT) for high-resolution conductivity imaging. Physiol. Meas. 29, R1-26. doi:10.1088/0967-3334/29/10/R01

Human In-vivo Brain Magnetic Resonance Current Density Imaging (MRCDI)

C Göksu, LG Hanson, HR Siebner, P Ehses, K Scheffler, A Thielscher

Supplementary Material

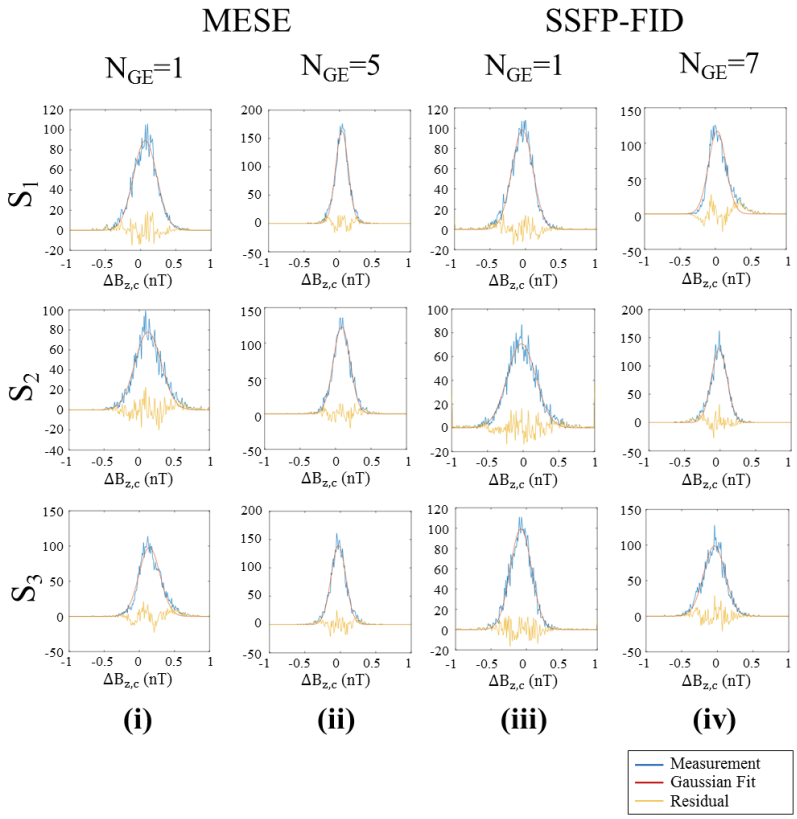

Supplementary Figure S1. Experiment 1: Comparison of single- vs. multi-gradient-echo acquisition for the case without current injection in three subjects. The plots show the $\Delta B_{z,c}$ distributions as histogram (blue), the Gaussian functions fitted to the distributions (red), and the residual of the fits (yellow). The T_{ES} (MESE) and T_R (SSFP-FID) were kept identical between both cases. MESE results: (i) N_{GE} = 1 and (ii) N_{GE} = 5. SSFP-FID results: (iii) N_{GE} = 1 and (iv) N_{GE} = 7. In both MESE and SSFP-FID, the results of the multi-gradient-echo acquisitions exhibit a lower noise floor than those of the single-gradient-echo acquisitions.

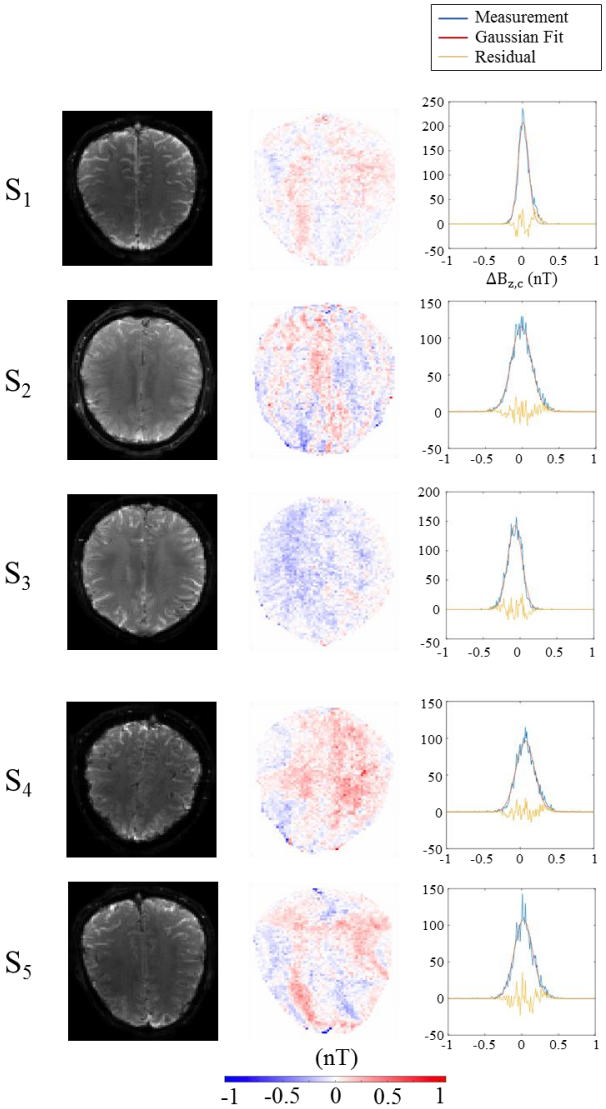

Supplementary Figure S2. Experiment 5: Control measurements without current injection for SSFP-FID measurements (T_R=120 ms, N_{meas}= 24) with multi-gradient-echo readouts of five subjects for the R-L and A-P electrode montages. Magnitude images (1st column), $\Delta B_{z,c}$ images (2nd column), and the corresponding histogram plots (3rd column) are shown. The histogram plots show the $\Delta B_{z,c}$ distributions as histogram (blue), the Gaussian functions fitted to the distributions (red), and the residual of the fits (yellow). The mean and standard deviations are in acceptable ranges (the standard deviation is less than 0.12 nT, and the mean is close to zero), which corroborates the accuracy of the measurements.

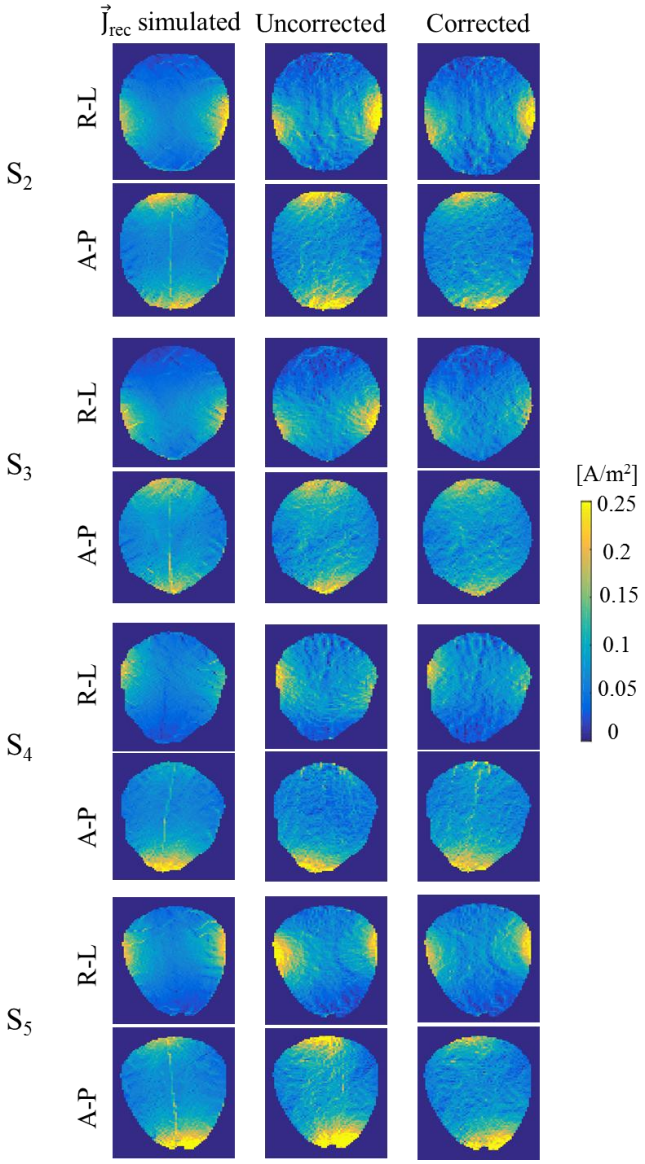

Supplementary Figure S3. Experiment 5: The reconstructed current density distributions from simulated and measured $\Delta B_{z,c}$ images (both with and without stray magnetic field correction) for subjects S_2 to S_5 (1st row: R-L montage; second row: A-P montage for each of the subjects). The norm of the current densities is depicted. Visual comparison of the reconstructions from uncorrected and corrected $\Delta B_{z,c}$ measurements reveals that the reconstructions from the uncorrected measurements overestimate the current densities close to the electrodes.

Copenhagen University Hospital Hvidovre
Centre for Functional and Diagnostic Imaging and Research
Danish Research Centre for Magnetic Resonance
Section 714
Kettegaard Allé 30
2650 Hvidovre
DENMARK
Tel: (+45) 3862 1184
Web: www.drcmr.dk
E-mail: info@drcmr.dk

Technical University of Denmark
Department of Electrical Engineering
Center for Magnetic Resonance
Ørsted Plads 349
2800 Kgs. Lyngby
DENMARK
Tel: (+45) 45 25 35 00
Web: www.elektro.dtu.dk
E-mail: info@elektro.dtu.dk